

DISS. ETH NO. 24962

Synchronized Two-Beam Strategies for Selective Laser Melting

A thesis submitted to attain the degree of
DOCTOR OF SCIENCES of ETH ZURICH
(Dr. sc. ETH Zurich)

presented by
THORSTEN HEELING
M.Sc., Ruhr-Universität Bochum
born on 16.10.1989
citizen of Germany

accepted on the recommendation of
Prof. Dr.-Ing. Konrad Wegener, examiner
Dr. Martin Schöpf, co-examiner

2018

Acknowledgements

The present thesis is the result of my almost four years of work at the Institute of Machine Tools and Manufacturing (IWF) of ETH Zurich. The work aimed for a better, more detailed understanding of the selective laser melting process and possible strategies for the optimization of it. During my time at IWF plenty of people contributed in some way to this work for which I am very grateful. In particular I want to thank

- Prof. Dr. Konrad Wegener for supervising this work, giving me the greatest freedom one can wish for to develop ideas and supporting me with great interest and expertise to get these ideas working. I really enjoyed the long, sometimes more, sometime less focused discussions about the details of this work.
- Dr. Martin Schöpf of Robert Bosch GmbH for showing great interest and support throughout the work as well as being co-examiner. I am especially thankful for him being always happy to give inputs from the industry side of view and to give advice in work and non-work related matters.
- The Bosch-Forschungstiftung (former Hans L. Merkle-Stiftung) for making all of this possible by supporting this work financially in the framework of their Program for Excellency in Science and Technology.
- The IWF and inspire workshop staff and technicians, especially Michel Demont, Albert Weber and Sandro Wigger, who largely contributed to the manufacturing and build-up of the SLM laboratory machine.
- My students who contributed a lot with their theses, especially by putting together most of the CAD/CAM-tool. The intern João Souza de Campos for taking care of other project's matters and thus keeping this additional work of me while I was working on this thesis. And my student assistant Fabian Keller for face lifting the simulation tool, so that it can be used by upcoming researchers more easily.

- Josef Stirnimann for taking care of all the background work, opening the way for me to work more freely and to care less about bureaucracy, and for always being open to discuss problems and their possible solutions.
- Dr. Michael Cloots for his great support in the early days of this work, the long discussions about whatever topic, which significantly helped getting another perspective or a better picture of it, and most notably for just making the time even more fun, during work as well as in free time.
- My colleagues in Zurich who contributed a bit on an every day basis by short discussions or during lunch time, especially Florian Wirth for being open to discussions regarding the simulation or for just listening to my problems when I was putting the simulation tool together. Furthermore, Maximilian Warhanek, Norbert Ackerl and Josquin Pfaff for advice in laser matters which helped putting together the laboratory machine and solving issues more rapidly.
- Colleagues in St. Gallen and other employees of Robert Bosch GmbH for long discussions about the industrial applicability of this work and for giving a better insight into the every day work with the SLM technology.

My utmost gratitude is dedicated to my parents, showing love and support on a daily basis and encouraging me to pursue any challenges I want.

Thorsten Heeling

January 2018

Contents

Acknowledgements	III
Abbreviations and Symbols	IX
Abstract	XIII
Zusammenfassung	XIV
1 Introduction	1
1.1 Additive Manufacturing	2
1.2 Selective Laser Melting	3
2 State of the Art	7
2.1 Current Understanding of the SLM Process	7
2.1.1 Absorption Characteristics	8
2.1.2 Heat Flow	12
2.1.3 Melt Pool Dynamics	15
2.1.4 Microstructural Effects	17
2.1.5 Evaporation and Spattering	19
2.1.6 Residual Stresses and Distortion	22
2.1.7 Defect Generation	23
2.2 Simulation of the SLM Process	25
2.2.1 Simulation of Fluid Dynamics	26

2.2.2	Simulation of Residual Stresses	29
2.3	Improving the SLM Process	30
3	Research Gap	32
3.1	Objectives and Work Packages	32
4	Numerical Modeling	34
4.1	Concept	34
4.1.1	Initial Configuration	36
4.2	Modeling Heat Flow	37
4.2.1	Absorption	37
4.2.2	Conduction, Convection and Radiation	40
4.2.3	Melting, Solidification and Evaporation	40
4.3	Modeling Fluid Flow	42
4.3.1	Surface Reconstruction	43
4.3.2	Driving Forces	44
4.3.3	Fluid Flow Solver	45
4.3.4	Volume and Heat Exchange	46
4.4	Validation	47
4.4.1	Material Data	48
4.4.2	Absorption Characteristics	49
4.4.3	Melt Pool Dynamics	52
4.4.4	Evaporation	55
4.4.5	Melt Pool Dimensions	56
5	Setup, Tools and Methods	58
5.1	Experimental Setup	58
5.1.1	Laboratory Machine	58
5.1.2	Initial Start-Up	61
5.1.3	High Speed Imaging	62

5.2	Software Tools	62
5.2.1	Beam Path Planning	62
5.2.2	Image Processing	64
5.3	Methods	66
5.3.1	Scan Field Calibration	66
5.3.2	Density Measurement	67
5.3.3	Microstructural Analysis	68
5.3.4	Distortion Measurement	68
5.3.5	Crack Penetration Depth Measurement	69
5.3.6	Surface Roughness Measurement	69
6	Investigation of Two-Beam Strategies	71
6.1	Setting a Reference	71
6.2	Offset Strategies	74
6.2.1	Experimental Planning	74
6.2.2	Microstructure and Density	76
6.2.3	Spatter Characteristics	84
6.2.4	Surface Roughness	88
6.2.5	Influence on Deflection	90
6.2.6	Simulation-Based Investigations	92
6.3	Wobble Strategy	95
6.3.1	Experimental Planning	95
6.3.2	Microstructure and Density	96
6.3.3	Spatter Characteristics	101
6.3.4	Surface Roughness	102
6.3.5	Influence on Deflection	104
6.4	Point-wise Heating	105
6.4.1	Experimental Planning	105
6.4.2	Microstructure and Density	106

6.4.3	High Speed Images	111
6.4.4	Surface Roughness	113
6.4.5	Influence on Deflection	115
6.5	Summary	116
7	Usability for Crack Susceptible Steel	118
7.1	Basic Investigations	119
7.2	Influence on Cracking	121
8	Conclusion and Outlook	125
	Bibliography	130
	Curriculum Vitae	141
	List of Publications	142

Abbreviations and Symbols

Abbreviation	Description
AM	Additive Manufacturing
CAD	Computer Aided Design
CLSVOF	Combined Level Set Volume of Fluids
DED	Direct Energy Deposition
HIP	Hot Isostatic Pressing
I/Os	In- and Outputs
PBF	Powder Bed Fusion
PISO	Pressure Implicit Splitting of Operators
PLC	Programmable Logic Controller
SLM	Selective Laser Melting
TGM	Temperature Gradient Mechanism
UTS	Ultimate Tensile Strength
VOF	Volume of Fluids

Symbol	Unit	Description
α	-	temperature-dependent material property of element
α_b	-	temperature-dependent material property of bulk material
α_{conv}	$[W/m^2 K]$	heat transfer coefficient
α_g	-	temperature-dependent material property of gas
β	$[m^{-1}]$	extinction coefficient
δ	-	dirac delta function
Δt	$[s]$	time step size
ΔT	$[K]$	temperature difference
Δx	$[m]$	element size or offset between two laser beams
ΔV	$[m]$	volume change
ϵ	-	emissivity
η	$[Pa s]$	dynamic viscosity
η_g	$[Pa s]$	dynamic viscosity of gaseous phase
η_l	$[Pa s]$	dynamic viscosity of liquid phase
κ	$[m^{-1}]$	surface curvature
λ	$[W/m K]$	thermal conductivity
λ_{opt}	-	optical thickness
ξ	-	dimensionless depth
ρ	$[kg/m^3]$	density
ρ_g	$[kg/m^3]$	density of gaseous phase
ρ_l	$[kg/m^3]$	density of liquid phase
ρ_{pl}	-	powder layer density
σ	$[N/m]$	surface tension
σ_B	$[W/m^2 K^4]$	Stefan-Boltzmann constant
φ	-	level set function

a	-	constant in absorption model
a^u	$[kg/s]$	coefficient of linear equation system
a^p	$[m\ s]$	coefficient of linear equation system
A	$[m^2]$	area
\mathbf{b}	$[N]$	vector of body and surface forces
\mathbf{b}_{buo}	$[N]$	body force due to buoyancy effect
\mathbf{b}_{cap}	$[N]$	surface force due to capillary effect
\mathbf{b}_{mar}	$[N]$	surface force due to Marangoni effect
\mathbf{b}_{rec}	$[N]$	surface force due to recoil pressure
c	$[N\ s/m]$	coefficient of linear equation system
c_p	$[J/kg\ K]$	specific heat capacity
d_B	$[m]$	beam diameter
d_{pp}	$[m]$	mean powder particle diameter
D	-	constant in absorption model
E_{eq}	$[J]$	equivalent energy
E_{fusion}	$[J]$	equivalent energy of fusion
F	-	filling degree
\mathbf{g}	$[N/kg]$	vector of gravitational acceleration
h_{pl}	$[m]$	powder layer height
H		smoothing function
i, j, k	-	element indexes
I	$[W/m^2]$	intensity
\mathbf{I}	-	unity matrix
L_{evap}	$[J/kg]$	heat of evaporation
M_{mol}	$[mol/kg]$	molar mass
n	-	time step index
\mathbf{n}	-	vector of normals
\mathbf{p}	$[bar]$	pressure field

p_0	[<i>bar</i>]	ambient pressure
p_{rec}	[<i>bar</i>]	recoil pressure
P_0	[<i>W</i>]	incident laser power
P_{abs}	[<i>W</i>]	absorbed power
\dot{Q}_{cond}	[<i>W</i>]	conductive heat flow in x , y or z
\dot{Q}_{rad}	[<i>W</i>]	radiative heat flow
\dot{Q}_{conv}	[<i>W</i>]	convective heat flow
R	[<i>J/mol K</i>]	universal gas constant
R_a	[μm]	arithmetical mean deviation of surface roughness
r	-	hemispherical reflectivity
S	[<i>W/m²</i>]	scattering term
T	[$^{\circ}C$]	temperature
$T_{liquidus}$	[$^{\circ}C$]	liquidus temperature
T_{pred}	[$^{\circ}C$]	predicted temperature
$T_{solidus}$	[$^{\circ}C$]	solidus temperature
\mathbf{u}	[<i>m/s</i>]	vector of fluid flow velocities
V	[<i>m³</i>]	volume
u, v, w	[<i>m/s</i>]	fluid flow velocities in x, y, z
x, y, z	[<i>m</i>]	Cartesian coordinates

Abstract

Additive Manufacturing, and selective laser melting in particular, are currently in the focus of various industrial sectors. The processes offer a far higher freedom of design than conventional manufacturing technologies which are already used in industry for decades or even centuries. The additive manufacturing technologies don't even need part specific tools to offer these benefits. Yet, porosity, anisotropy, evaporation and spattering, surface roughness as well as distortion and cracking are inherent problems which are holding the processes back from being used to a larger extent.

The presented thesis is taking part in the search for a promising strategy to get rid of those inherent problems within the selective laser melting process by investigating innovative irradiation strategies. These strategies are defined by the use of two synchronized laser beams which are focused to the same scan field. This can be used to change the effective intensity profile within the vicinity of the melt pool or to implement completely new strategies like a point-wise heating strategy. Since no common machine offers the use of these strategies, the concept and use of a self-developed and built up laboratory machine is presented in before. The experimental investigation of these strategies is supported by the use of a numerical model which is covering the temperature and fluid flow simulation on melt pool scale. In before the use of the numerical model it is validated. The validation shows a good accordance of the model with experimental results which can be accounted to the implementation of the absorption model that allows the differentiation of various material configurations while working on a quite coarse grid.

The experimental investigation of synchronized two-beam strategies shows that when using a defined offset of a melting beam to a heating beam it is possible to reduce spattering if the heating beam is moving in front of the melting beam. In case the heating beam is following in a certain offset a in-situ smoothing of the surface can be realized. In contrast, when using a point-wise heating strategy global effects can be induced to the part that can be used to reduce distortion and cracking.

Zusammenfassung

Additive Fertigungsverfahren, und das selektive Laserschmelzen im Speziellen, erfreuen sich großer Aufmerksamkeit, da diese Verfahren im Vergleich zu jenen, welche seit Jahrzehnten oder gar Jahrhunderten in der Industrie Anwendung finden, größere Gestaltungsfreiheit bieten und gleichzeitig keine werkstückabhängigen Werkzeuge benötigen. Jedoch hindern bisweilen inhärente Probleme wie Porosität, Anisotropie, Verdampfung und Spritzerbildung, rauhe Oberflächen sowie Verzug und Risse deren umfassendere Ausbreitung.

Vor diesem Hintergrund befasst sich die vorliegende Arbeit mit der Umsetzung und Untersuchung möglicher Belichtungsstrategien für den Prozess des selektiven Laserschmelzens, um die inhärenten Probleme signifikant zu reduzieren. Diese Belichtungsstrategien zeichnen sich durch die gleichzeitige, synchronisierte Nutzung zweier Laserstrahlen in ein und demselben Belichtungsbereich aus. Somit lassen sich die effektiven Intensitätsprofile innerhalb der Schmelzbadumgebung anpassen. Da keine aktuell verfügbaren Maschinen diese Strategien ermöglichen, werden im Voraus zusätzlich das Konzept sowie die Besonderheiten der Nutzung einer für diesen Zweck selbst entwickelten und aufgebauten Versuchsmaschine dargelegt. Die experimentellen Untersuchungen werden mit einem numerischen Modell, welches das Temperatur- und Strömungsfeld auf Schmelzbadebene abbildet, begleitet. Dieses Modell zeigt bei der vorausgehenden Validierung eine gute Übereinstimmung mit den experimentellen Ergebnissen, was insbesondere auf die Implementierung des Absorptionsmodells zurückzuführen ist, welches trotz einer groben Modellvernetzung eine Unterscheidung verschiedener Materialzustände ermöglicht.

Die experimentelle Untersuchung der synchronisierten Zweistrahlstrategien zeigt, dass bei der Nutzung einer definierten Distanz zwischen Schmelzstrahl und Heizstrahl eine Reduzierung der Spritzer möglich ist, sofern der Heizstrahl dem Schmelzstrahl vorausseilt. Folgt der Heizstrahl dem Schmelzstrahl hingegen ergibt sich die Möglichkeit Oberflächenrauheiten noch vor der endgültigen Erstarrung des Schmelzbades deutlich zu reduzieren. Gleichmaßen ist es möglich bei der Nutzung eines punktwisen Heizens mit einem der beiden Strahlen spur- und schichtübergreifende Effekte zu erzielen, welche in einer Reduzierung von Verzugs und Rissbildung resultieren können.

Chapter 1

Introduction

As Wohlers et al. [107] report, additive manufacturing (AM) technologies are already under development for about 50 years now, with first commercial machines being offered since the 1980s. In the beginning the AM processes were referred to as rapid prototyping because of the chance to generate a prototype without specific tooling. Yet, the parts were not intended to be used as industrial parts. As soon as first industrial parts were generated using these technologies it was commonly referred to as rapid manufacturing although conventional processes have often been more rapid than these processes [105]. Hence, with ongoing standardization the term of additive manufacturing was established to account for the technologies' characteristics properly.

After progressing in the shadows for a while, the possibilities of AM technologies are recently pushing these processes into the focus of various industrial sectors because they offer the chance to overcome challenges with which conventional manufacturing technologies are struggling, such as freedom of design and high individualization without part specific tooling as well as generating new materials or designing material properties during build-up. Hence, most of today's applications of AM technologies can be found in sectors where these factors are essential like consumer products, medical parts and small batch high value parts, but companies are looking forward to apply these technologies to a wider range of parts [107].

Yet, the quality, productivity and robustness of AM processes have to be significantly increased because the commonly layer-wise process in which micron scale material changes are accumulated over and over again to reach the desired geometry is taking a lot of time while being susceptible to defects, like porosity, cracking, distortion and high surface roughness. Furthermore, AM parts behave differently in regards to their mechanical properties because of the layer-wise build-up which results in a strong anisotropy with strongly elongated grains along the build direction and non-fully preventable porosity which reduces

the dynamic mechanical properties because it works as a lot of different starting points for crack growth. The presented thesis takes part within the search for possible process optimizations to increase the industrial applicability, focusing on the selective laser melting (SLM) process.

1.1 Additive Manufacturing

A process is considered additive manufacturing if it's gradually building up a part, often in a layer-wise process, without part-specific tools and is thereby defining the part's properties [83]. In case of today's AM technologies a sequence of digital processes is needed to start the build-up process, beginning with the computer aided design (CAD), followed by a platform neutral STL-file export which used to slice the model into single layers and a platform specific file which contains the layer information of the sliced part and on some machines even the processing parameters. As Schmidt et al. [83] state, the beginnings of modern AM are commonly dated to the years around 1980 when patents for the processes of laser sintering and stereolithography were filed.

By now, plenty more processes have been implemented to additively build up parts with a large variety of different materials, dimensions and resolutions. ISO 17296 [38] classifies this large amount of processes based on feedstock morphology, feedstock delivery and the binding mechanism into seven basic categories: binder jetting, directed energy deposition, material extrusion, material jetting, powder bed fusion, sheet lamination and vat photopolymerization. Directed energy deposition (DED) and powder bed fusion (PBF) are commonly the processes of choice for metal parts, but there are approaches for metal processing within the other categories as well. In case of DED the feed stock is either powder or wire material that is rapidly heated by an arc, a plasma, an electron beam or a laser beam. The PBF processes only work with powder material which is irradiated by an electron beam or a laser beam.

The main reason for the increasing industrial relevance of these AM processes is a benefit which is known as "complexity for free" [83]. It is defined by the fact that due to the gradual build-up of parts complexity can be integrated within the part without significant additional costs as long as the design guidelines are taken into account. In fact, a high complexity, from the view of conventional manufacturing, can reduce the costs of AM parts due to a reduced amount of material that is needed to be build. Only if the amount of necessary support structures increases, material, machine time as well as post-processing costs increase. Therefore, a design for AM is considered to be necessary for a reasonable use of these technologies because in the low complexity regime conventional manufacturing

technologies are certainly more capable. The design for AM can even be used to merge multiple parts into one. A illustration of this benefit is depicted in Fig. 1.1.

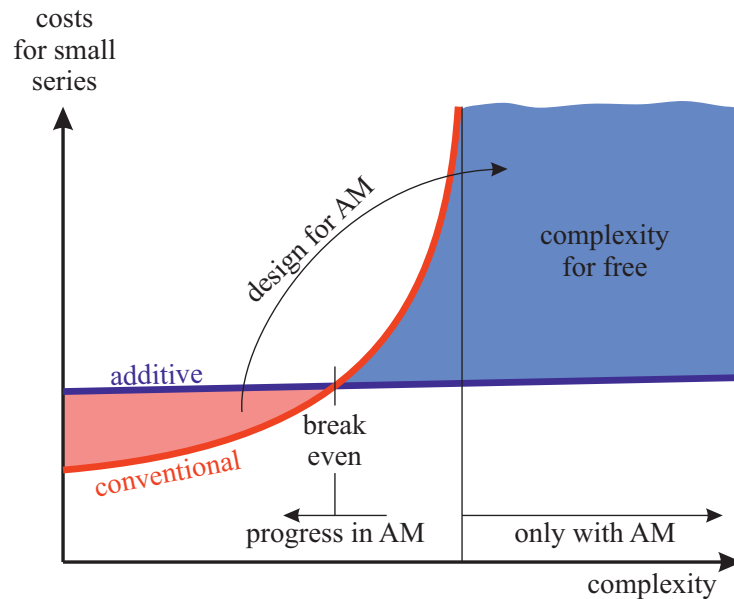


Figure 1.1: Illustration of “complexity for free”. At low complexity conventional manufacturing technologies are much cheaper than additive manufacturing. At a certain degree of complexity a break even point is reached after which additively manufactured parts are more economical. Furthermore, conventional manufacturing reaches a singularity which represents the degree of complexity that can be manufactured with those technologies. AM is able to surpass this degree of complexity. Progress in AM technologies will reduce the costs and thus move the break even point to a lower complexity (compare to [83]).

Since the material properties are build-up with the part’s geometry at the same time due to the layer-wise process, the qualification of additively manufactured parts and their mechanical properties is of high importance. Yet, it has to be taken into account that today most metal parts that find application in industry are heat treated after being manufactured so that material properties change after being generated by the AM process. Still, inherent defects are commonly not removed by these treatments so that a defect free build-up of parts is essential.

1.2 Selective Laser Melting

Selective laser melting is a laser based powder bed fusion process for metals and is equivalent to the processes of direct metal laser sintering, laser metal fusion or lasercusing which are other company specific terms for it. The basic components that are needed are a laser source, a laser beam deflection unit (commonly referred to as scan head) with appropriate optics, a powder deposition unit, a powder reservoir, a build plate and a powder overflow.

The components are in an enclosed build chamber which is filled with inert gas and which offers a constant inert gas flow over the build plate. The process follows a layer-wise procedure which is illustrated in Fig. 1.2. The first step of any layer is the deposition of the powder material. Therefore the build plate is lowered by the desired layer thickness, commonly $20\ \mu\text{m}$ to $100\ \mu\text{m}$, and a powder deposition unit is pushing the powder by a linear movement from the powder reservoir over the build plate to the overflow.

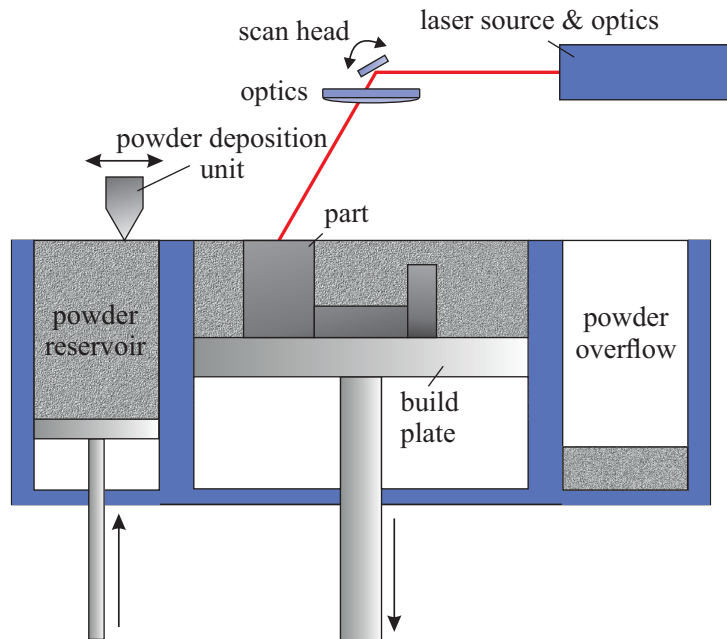


Figure 1.2: Simple depiction of the basic components within an SLM machine as well as their movements during the process.

The powder particles are usually smaller than about $60\ \mu\text{m}$ and can consist of various pure elements or alloys. As soon as the powder is deposited the layer is selectively irradiated by a laser beam that is deflected by the scan head and focused by a $f-\Theta$ -lens to move within the build plane. The laser beam diameter within the build plane is commonly set to $50\ \mu\text{m}$ to $150\ \mu\text{m}$, depending on the laser power and desired application. The irradiation is split in at least two steps. On the one hand, the irradiation of the core area of the desired cross section, commonly referred to as “hatching”. And on the other hand, the irradiation of the contour that results in the outer surface of the part. Different parameters are chosen for these two sections to achieve the best quality. During the irradiation the inert gas flow forces spatter away from the build plate and transports evaporated material to a filter system. A new layer is deposited as soon as the irradiation of the desired parts’ cross sections is finished.

Due to the small layer thicknesses, laser beam diameter and powder particle size, SLM offers the chance to manufacture highly complex, high resolution parts. The only restrictions for the design of SLM parts is given by the necessity to get the heat out of the part and to keep residual stresses and distortion in check. Therefore, support structures are used to conduct heat to the base plate, so that overhanging areas do not overheat, and to keep the material in place, so that features don't warp. Without support structures the minimum overhang angle is usually limited to about 45° [15].

Still, a range of drawbacks is restraining the larger scaled use of SLM. Those are a result of the layer-wise process, the use of powder material and especially the very high cooling speeds and thermal gradients. Therefore, residual stresses, cracking and porosity reduce the parts' mechanical properties and lifetime, while distortion might leave the part unusable and surface roughness as well as a strong anisotropy make a series of post-processing steps necessary [81, 65]. When considering these factors one can estimate the extent of these influences on the part's accuracy as listed in Tab. 1.1. While pores and cracks can result in severe problems within the part, the outer dimensions are mainly influenced by the part's distortion which are a result of the residual stresses as well as the part's geometry and the available resolution which is restricted by the melt pool size, the layer thickness and thereby the powder particle diameter because it is defining the minimum possible value of layer thickness. Although residual stresses and resulting distortion can be reduced by heat treatment, it has to be made sure that the residual stresses do not result in cracking or warping within the process which cannot be removed after build-up.

Table 1.1: Main influencing factors on part accuracy and their extent in SLM (compare to [105]).

influencing factor	dimension	extent [μm]
positioning accuracy of laser	x, y	≤ 5
positioning accuracy of build plate	z	≤ 5
discretization error of slicing	x, y, z	≤ 70
melt pool width	x, y	≥ 100
distortion	x, y, z	mm range

Furthermore, the layer-wise process results in comparably high manufacturing times, which is why a lot of effort is put into the optimization of the SLM process. Yet, there is already a range of established application areas of SLM parts consisting of lightweight parts, turbine components, medical prostheses and tools as well as injection molding tools with conformal cooling. Additionally, it offers high potential for small batch series of parts that need special tooling, for any part with complex outer or especially inner structures or for any highly individualized product [107].

While there are different approaches to speed up the process, for example by higher power [12] or the parallel use of multiple laser beams [5], and approaches to increase the overall part quality and material processability, for example by heating up the build plate [114], this thesis follows the approach of using two synchronized beams to influence the temperature field in the vicinity of the melt pool. This approach has first been proposed by Abe et al. [1] in 2001, but no sincere follow-up investigation of this promising way to change the process is known.

Chapter 2

State of the Art

As explained before additive manufacturing technologies are of growing industrial relevance, but are still suffering from various drawbacks. The following sections start with a discussion about the current understanding of the SLM process. It is split into the sub-processes of absorption, heat flow, melt pool dynamics, microstructural effects, evaporation and spattering, residual stresses and distortion as well as overall effects of defect generation. By doing that, a deep knowledge of the process dynamics is built up as a basis for the upcoming chapters, in which the effort of this thesis to reduce those drawbacks is explained. This knowledge is extended by further information about the state of the art in simulating the SLM process, either with a focus on fluid dynamics or residual stresses. The state of the art closes with a discussion of current thesis related improvement strategies within the SLM community to enable the process being used for a wider range of possible applications.

2.1 Current Understanding of the SLM Process

The understanding of the process dynamics is crucial to the optimization of the SLM process. The high process dynamics make it difficult to get the necessary knowledge by experiments only. In fact, numerical approaches are equally important to get a sufficiently detailed idea of the importance of different effects that take place during SLM. Hence, in the following sections the current understanding regarding the process' driving forces and main effects is discussed on the basis of experimental as well as numerical investigations. The section starts with the effects that lead to melting, consolidation and solidification of the powdered and bulk material, followed by effects and defects that are a result of these steps. The information of the upcoming subsections is summarized in Fig. 2.1.

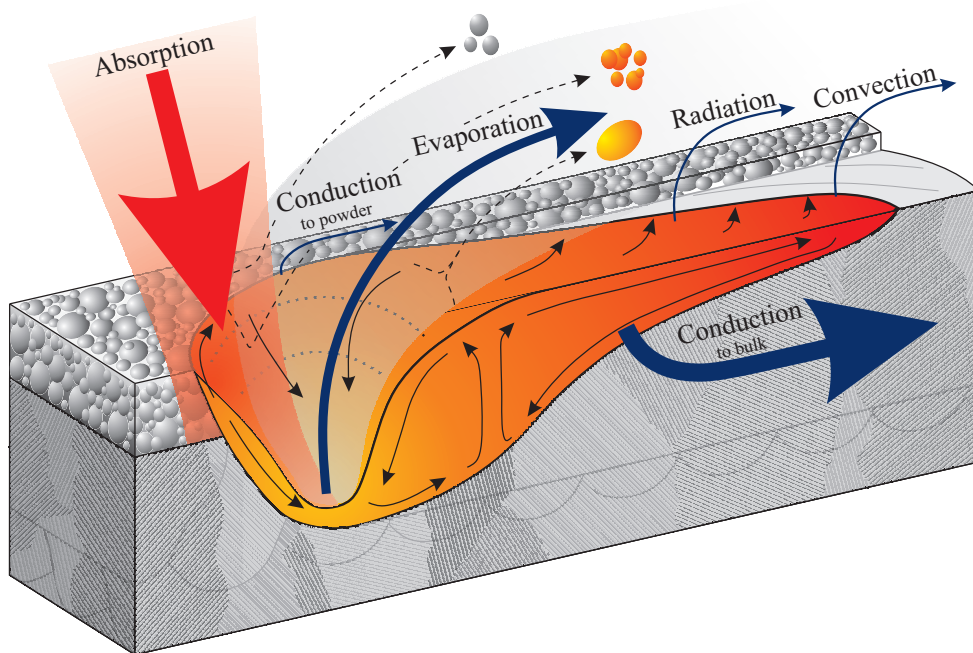


Figure 2.1: Summary of the main effects on melt pool scale that are dominating the process. The illustration shows heat flow, evaporation and spattering, melt flow as well as microstructural characteristics.

2.1.1 Absorption Characteristics

The interaction of laser light and material is the first micro-domain step on the path to a track, a cross section or even a larger part produced by SLM. Therefore the absorption characteristics are of undeniable importance for the process. Unfortunately, the material configuration in the process, meaning powdered material that is lying with a certain packing density on a previously solidified track, is making it impossible to use the known absorptivity of bulk materials. Rather, multiple reflection in the powder bed and possibly in a keyhole-like melt pool needs to be considered. Because of this, not just the layer thickness and bulk absorptivity are of importance, but even more influencing factors like the particle size distributions, packing densities and evaporated material as well as spatter need to be taken into account.

Since the measurement of absorptivity in a configuration similar to the process conditions is difficult, most of the early work in this field is based on analytical and numerical models. Singh and Kaviany [89, 90] were one of the first to investigate the absorptivity of powder beds that are comparable to those of the SLM process. They used analytical, numerical as well as experimental approaches to investigate the influence of packed powder beds, showing that even at a packing density as low as about 7% the absorption and scattering characteristics cannot be considered independent of neighboring particles. Therefore, a

powder bed of higher packing density needs to be handled in a different way. To circumvent the problem of dependent scattering a so-called two-flux method is employed. The two-flux method is tracking forward (deeper into the powder bed) and backward (out of the powder bed) scattered light, so that with the integration of both fluxes the intensity at a certain position can be calculated. The main issue is that the basic two-flux method is not applicable for powder beds in which energy is absorbed by particles [89]. Still, scaling factors can be used to mimic the extinction of light within the powder bed [90].

Gusarov and Kruth [31] used these approaches to transfer the radiation transfer theory to metallic powder beds that are irradiated by a laser beam, and therefore generated the basis for use in SLM modeling. The strength of this theory is that it gives comparable results to the far more complicated ray tracing technique, in which the laser beam is modeled as a large amount of single photons which are interacting with the material, leading to absorption and reflection. Gusarov et al. [33] simplified the equations, so that the model can be used with common SLM powder bed characteristics such as the layer thickness, an estimated packing density, an average particle size and the bulk material reflectivity. Thereby it is possible to estimate an overall absorptivity in a homogenized powder bed and its dependencies of the previously named powder characteristics as well as the amount of energy which is absorbed by the underlying bulk material. With this approach Gusarov et al. showed that in general the overall absorptivity is increasing with increasing optical thickness up to a saturation value which is slightly above 70 % for the investigated stainless steel powder bed. The optical thickness itself increases with increasing packing density and layer thickness as well as decreasing mean particle diameter. Furthermore, they show that independent of the powder bed's optical thickness the major amount of energy is absorbed in the uppermost part of the powder bed. The basic effects of absorption within a powder bed are illustrated in Fig. 2.2.

In contrast to this homogenized powder bed approach, Streek et al. [96] elaborated a ray tracing technique to further investigate the dependencies and influences within the powder bed. Due to the tracking of a large amount of single rays the spatial resolution within the absorption characteristics is higher. They showed that the absorbed energy is confined to a volume that consists of a cylindrical shape at the top of the powder layer and a cone shape with decreasing diameter for the lower powder bed regions. Regarding the dependencies of absorptivity from the parameters of packing density and mean particle diameter, Streek et al. support the findings of Gusarov et al. They showed as well that most of the energy is absorbed in the uppermost regions of the powder bed. Boley et al. [9] as well elaborated ray tracing but were focusing on the influence of the particle size distribution on the overall absorptivity as well as its influence on the fluctuation of absorptivity along a track. Starting with a powder bed that consists of single sized particles in dense hexagonal

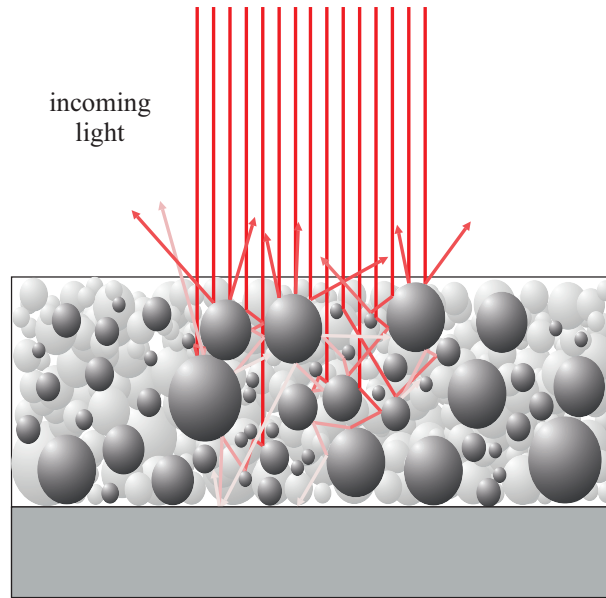


Figure 2.2: Illustration of the basic effects of light propagating into a powder bed of opaque particles. The reflection is idealized to be two-dimensional. The color of the photons is representative for the amount of residual energy. The more red it is, the higher the energy.

close-packing, they showed that the absorptivity is significantly increased due to multiple scattering within the powder bed. The increase is dependent on the bulk absorptivity. The higher the bulk value the lower the increase. Hence, for silver an absorptivity increase of factor 7.2 and for stainless steel of factor 1.7 can be achieved when irradiating a powder bed instead of a bulk surface. In addition, they showed that the absorptivity fluctuates by about 20 % (for this configuration) when scanning along a track. This is explained by the changing amount of irradiated top particle surfaces. With Gaussian or bimodal particle size distributions the fluctuation of absorptivity can be reduced since smaller particles are filling the gaps between the larger ones. Boley et al. estimated the absorptivity of a $43 \mu\text{m}$ powder layer with stainless steel particles of Gaussian size distribution with an average radius of $13.5 \mu\text{m}$ to be about 58 %.

Recently first experimental results have been published in which configurations close to the SLM process have been used. The measurements were done using calorimetry. Rubenchik et al. [82] used a thin disk of refractory metal which is located on thin wires to minimize the amount of heat that is conducted out of the system. The influence of heat losses due to conduction and convection were investigated before and Rubenchik et al. showed that those effects can be neglected within this setup. A 970 nm laser with 50 W power was used to heat the powder materials, stainless steel 316L, TiAl6V4 and 99.9 % pure aluminium, to temperatures as high as $500 \text{ }^\circ\text{C}$. So, no extensive oxidization or even melting occurred within these experiments. The measurements resulted in absorptivities of about 60 % to

65% for SS316L, about 70% for TiAl6V4 and about 50% to 55% for the aluminium powder bed and therefore proved that multiple reflection in powder beds significantly increases the overall absorptivity.

Trapp et al. [101, 64] were using an improved calorimetry setup. In this the disc that holds a $100\ \mu\text{m}$ layer of powder is located on porous alumina tubes. The setup is located in an argon atmosphere and a $1070\ \text{nm}$ laser source with up to $600\ \text{W}$ and a focal diameter of about $60\ \mu\text{m}$ is used. Trapp et al. started with the investigation of single tracks on bulk material to get an idea about the influence of heat conduction welding and deep penetration welding. For SS316L bulk material the absorptivity is increased from 30% in heat conduction welding to over 75% in deep penetration welding due to multiple reflection in the keyhole. The same values are achievable when irradiating a powder bed with the same parameters. For faster scan speeds the change to deep penetration welding obviously moves to higher powers. In case of a powder layer the initial absorptivity at very low powers is significantly higher compared to the bulk material. With increasing powers the powder melts, resulting in a reduced overall absorptivity. In contrast, when the deep penetration welding like process window is reached, the absorptivity increases significantly. Compared to the bulk material the deep penetration state is reached earlier in case of the powder layer but its extent is not as strong. Trapp et al. [101] suggested that the porosity of the powder layer supports the build-up of the keyhole, but that particles that pass the laser beam are preventing the keyhole from reaching its maximum extent. Within a reasonable processing parameter window Trapp et al. measured an absorptivity of about 60% to 70% for SS316L. A possible effect of heat loss due to evaporated material was neglected. The basic effects of energy absorption within reasonable process parameters are illustrated in Fig. 2.3.

Summarizing these numerical and experimental investigations, one has to keep the following unique effects in mind when thinking about the energy input for the SLM process.

1. Due to multiple reflection the overall absorptivity in powder beds is significantly higher than it is for bulk materials. For reasonably absorbing materials like steel, nickel-base superalloys or titanium alloys the increase in absorptivity is lower than factor 2. But for highly reflective materials such as aluminium, copper, silver or gold the increase can be as high as factor 7.
2. Most of the power is absorbed by the uppermost particles within the powder layer.
3. Increasing layer thickness and packing density as well as reducing the mean particle diameter leads to an increased overall absorptivity.

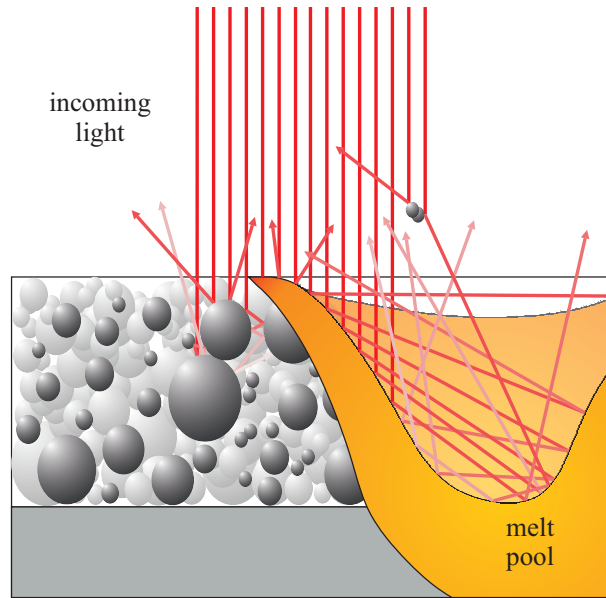


Figure 2.3: Illustration of the absorption characteristics during the SLM process. A part of the incoming laser power is absorbed within the powder bed, a large part within the melt pool and a keyhole-like dent and even some photons are reflected at spatter particles that cross the incoming light. The reflection is idealized to be two-dimensional. The color of the photons is representing the amount of residual energy. The more red it is, the higher the energy.

4. Wide particle size distributions can decrease fluctuations of absorptivity along a scan vector.
5. For processing parameters there are three distinct regimes. For low energy densities the absorptivity is quite high due to multiple reflection in the powder bed. This regime is not applicable because no melt pool is generated. For a small region of medium high energy densities the absorptivity is low because the absorption is mainly taking place on the melt pool surface. For high energy densities the absorptivity is high due to multiple reflections in the keyhole or a keyhole-like dent in the front of the melt pool.

2.1.2 Heat Flow

Understanding the heat flow within the melt pool vicinity is very important to guarantee good part quality, because the melt pool shape is a result of the, ideally steady state, difference of absorbed power and the heat flow that is leaving the melt pool and its vicinity. Due to the high laser beam deflection speeds and the small melt pool size on a comparably large part, a closer look into the effects that result in heat flow within and out of the melt pool region is important.

The common understanding in SLM is that heat conduction has the largest part in taking energy away from the melt pool and therefore is the main reason for the incredibly high cooling speeds of $10^6 K/s$ and more. This is due to the fact that the melt pool usually just takes a volume in the range of about $100 \mu m$ depth x $200 \mu m$ width x $1000 \mu m$ length. This size is tiny when being compared to part volumes of some cubic centimeters. Therefore, the melt pool can often be considered to be moving on an infinitely large metallic heat sink, although heat accumulates within the build over time. This assumption is just applicable for heat being conducted to lower layers. As Sih and Barlow [87] and Rombouts et al. [80] showed, the thermal conductivity within the powder bed has to be considered being significantly lower. Rombouts et al. showed that the thermal conductivity of SLM powder beds is mainly dependent on the the packing density as well as the particle shape and not of the bulk material's thermal conductivity. They show that the thermal conductivity of a stainless steel powder bed is about as high as the thermal conductivity within a copper powder bed, with both being about $0.1 W/m K$ to $0.2 W/m K$. Khairallah and Anderson [46] supported these results with simulative studies. The influence of the bulk material's thermal conductivity increases for particles in the millimeter range because in that case the number of contact points is significantly reduced and the thermal conductivity within single particles is getting more important [80]. Consequently, the material configuration next to the melt pool is of high importance. As Clijsters et al. [15] showed, the melt pool size differs between the heat flow being dominated by surrounding powder or by surrounding bulk material. So the melt pool size increases in case of overhanging structures because the heat flow is constrained by the surrounding and underlying powder particles and only a small portion of the melt pool is in contact with bulk material.

The influence of convective losses to the surrounding gas atmosphere is commonly assumed to be negligible for the melt pool itself. King et al. [49] suggested that the importance increases when taking a look on the part scale. Neglecting the effect of radiative losses is usually not discussed because the implementation within simulation models is too easy to neglect it. Still, it's easy to approximate its part being far smaller than 1% of the overall heat flow, mainly because of the small melt pool size. In contrast, heat loss due to evaporation is of crucial importance. Early simulation models demonstrated the importance of evaporation by showing that the melt severely overheats if no evaporative heat loss is considered. As shown by Khairallah et al. [47] the evaporative heat flux can be estimated with a quite simple equation. They estimated that about $0.1 \mu g$ material evaporates per millimeter molten track, but little information is given about the elaborated values. Using the numerical model which is presented in later sections, one can estimate the amount of evaporated material to be even higher than $1 \mu g/mm$ and in consequence the heat loss due to evaporation to be higher than $7.5 W$. Heat loss due to spattering has not yet been

discussed in any publication. Yet, as explained in section 2.1.5, the most common kind of spatter consists of particles that are entrained by the gas flow and rapidly heated within the vapor jet of evaporated material. Accordingly, no additional heat is taken out of the melt pool vicinity by those spatter particles. The fraction of spatter that is ejected from the melt pool is fairly small and is subject to a certain randomness. Hence, the heat loss due to melt pool spatter can not be considered as a constant heat flow out of the melt pool region.

The last major influencing factor are the melt pool dynamics. While no heat loss is present due to melt flow, a significant redistribution of heat is present within the melt pool. Lee and Zhang [58] stated that in contrast to heat conduction being the dominant mechanism for heat flow out of the melt pool, melt flow is dominating the heat flow within the melt pool. The melt pool dynamics are discussed in the upcoming section. In addition, the heat of fusion cannot be neglected when modeling the temperature field, even though it also cannot be considered a heat flow or heat loss. Instead, it has to be considered a temporal storage of energy which is filled in between solidus and liquidus temperature during melting and emptied between liquidus and solidus temperature during solidification. The main aspects of heat flow in SLM are summarized in Fig. 2.4.

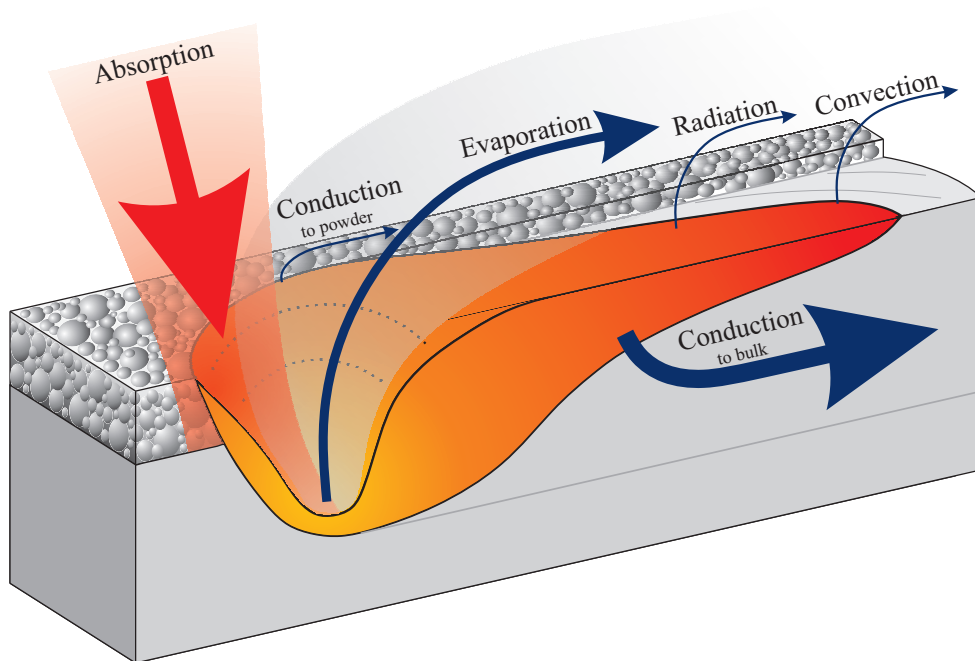


Figure 2.4: Summary of the basic effects in heat flow. The importance of the effects is illustrated by the width of the depicted heat flows. (in accordance with [15, 16])

2.1.3 Melt Pool Dynamics

Due to the small dimensions and high speeds of the process, most of SLM melt pool dynamics is known from simulation studies. Today's understanding of the melt pool dynamics is that it is driven by capillary forces, the Marangoni effect and recoil pressure due to evaporation as well as, to a far lesser extent, by buoyancy forces. Rombouts et al. [81] have been one of the first to describe the importance of the Marangoni effect in SLM melt pools. The Marangoni effect is defined by the minimization of surface energy in case of surface tension gradients. Therefore, melt is flowing from areas of low surface tension to areas of high surface tension. Surface tension gradients arise in the melt pools due to the temperature coefficients of surface tension, resulting in low surface tension in hot areas and high surface tension in cold melt pool areas for most commonly used alloys. Hence, melt is flowing from the center of the laser irradiated melt pool to the colder outside regions and therefore widening the melt pool. However surface active alloying elements, e.g. sulfur and oxygen in iron, can invert the temperature coefficient [81]. Gu et al. [19, 30] showed that the Marangoni effect is strong enough to neglect the buoyancy forces when simulating SLM melt pools. While the buoyancy effect alone results in velocities of only a few tenth of meters per second, melt pool velocities can be as high as some meters per second when considering the Marangoni effect.

Khairallah and Anderson [46] discussed the importance of the capillary effects. They used a simulated powder bed to show that without the capillary effect the melt pool does not consolidate, just resulting in neighboring melt droplets. In contrast, when capillary forces are considered a melt pool forms which is wetting the underlying substrate. Recent studies showed that it is important to also take evaporation into account when simulating melt pool dynamics. Lee and Zhang [58] as well as Khairallah et al. [47] came to that conclusion based on simulative studies, while Zhao et al. [111] employed experimental methods using high speed x-ray imaging. The evaporation of material in the front of the melt pool results in a recoil pressure on the melt pools surface. The recoil pressure induces a strong downward and rearward flow, pushing the melt away from the area of highest temperature, thereby commonly generating a keyhole-like dent or for very high energy densities even keyholes comparable to what is known from welding literature.

Therefore, Khairallah et al. [47] proposed to divide the melt pool in three distinct areas when discussing the melt pool dynamics, as illustrated in Fig. 2.5. First, the keyhole-like dent in the very front of the melt pool which is dominated by recoil pressure that induces melt pool velocities of about 10 m/s . Second, the melt pool tail which is dominated by Marangoni effect and capillary forces, resulting in melt pool velocities of about 2.5 m/s or less [30]. And third, the transition zone between front and tail which is dominated by the

melt that is pushed rearwards by recoil pressure. Hence, a cross section is underlying three significant phases when being irradiated. It starts with the laser beam rapidly heating the material to evaporation temperature, resulting in recoil pressure that pushes the melt away, generates a cavity and drives the melt pool in higher depth. It is followed by a stage when the cavity is filled by the rearward melt flow and ending with a Marangoni and capillary effect driven stage that is generating the final melt pool shape.

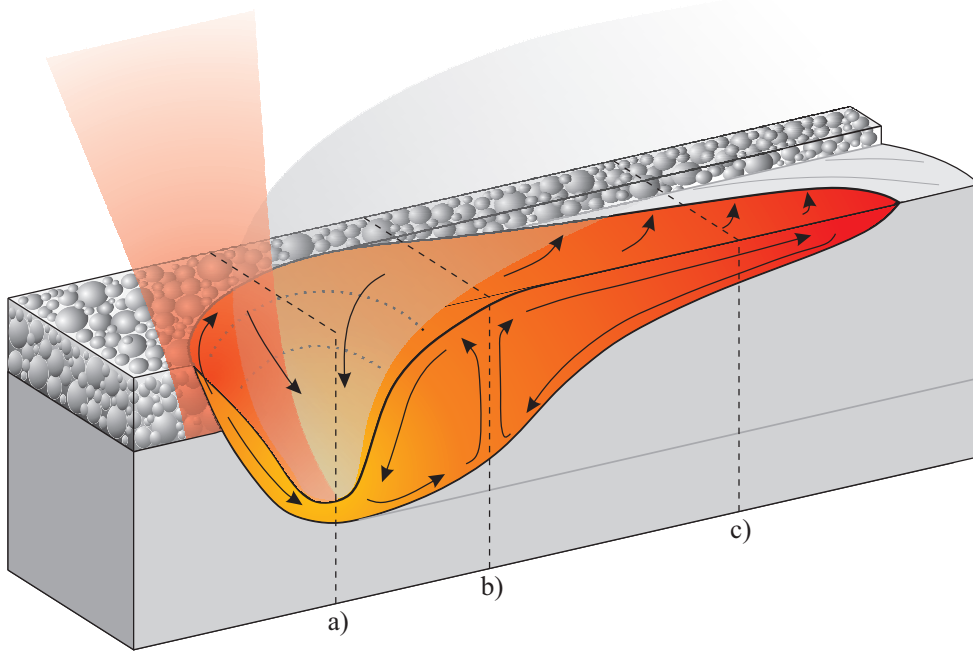


Figure 2.5: Illustration of the dominating melt pool flows, a) melt is pushed away by recoil pressure, b) cross section is filled with rearward flow, c) final shape is generated by Marangoni and capillary effects (in accordance with [47, 58, 111])

In addition, it is worth noting that the randomness of the powder bed is influencing the melt pool dynamics and therefore the resulting melt pool as well. As Koerner et al. [51] showed for electron beam melting, the initial material configuration is significantly influencing the melt pool shape due to the wetting of the melt pool to the surrounding material. Although in laser based processes a far lower amount of material is molten on powder material due to the heat flow problem described in 2.1.2, an influence of the powder particle configuration on the SLM process can be assumed, especially in overhanging areas. In summary, the following aspects are of high importance to the melt pool dynamics.

1. The melt pool dynamics are mainly driven by the recoil pressure, the Marangoni effect and capillary forces. Buoyancy forces are too small to significantly affect the melt pool dynamics.

2. Within a melt pool three distinct areas should be considered. First, the keyhole-like dent in the melt pool front which is driven by recoil pressure. Second, a transition zone between front and tail. Third, the melt pool tail in which the dynamics are driven by Marangoni convection and capillary forces.
3. Around the keyhole-like dent melt pool velocities are as high as 10 m/s . In the back of the melt pool the velocities might be as high as 2.5 m/s .

2.1.4 Microstructural Effects

The following section discusses a small selection of publications concerning the basic effects in microstructural development and characteristics of SLM parts. By now a large number of publications is available for almost every alloy system that is used within this process (see Gu et al. [29]). Kruth et al. [53] described that the microstructure of SLM parts is driven by very high cooling speeds of 10^6 K/s and temperature gradients of 10^6 K/m . Therefore, very fine grains are formed during solidification. These grains are commonly equiaxed in the build plane but highly elongated along the build direction due to epitaxial growth. Thereby, a strong anisotropic microstructure is formed. The general trends are illustrated in Fig. 2.6.

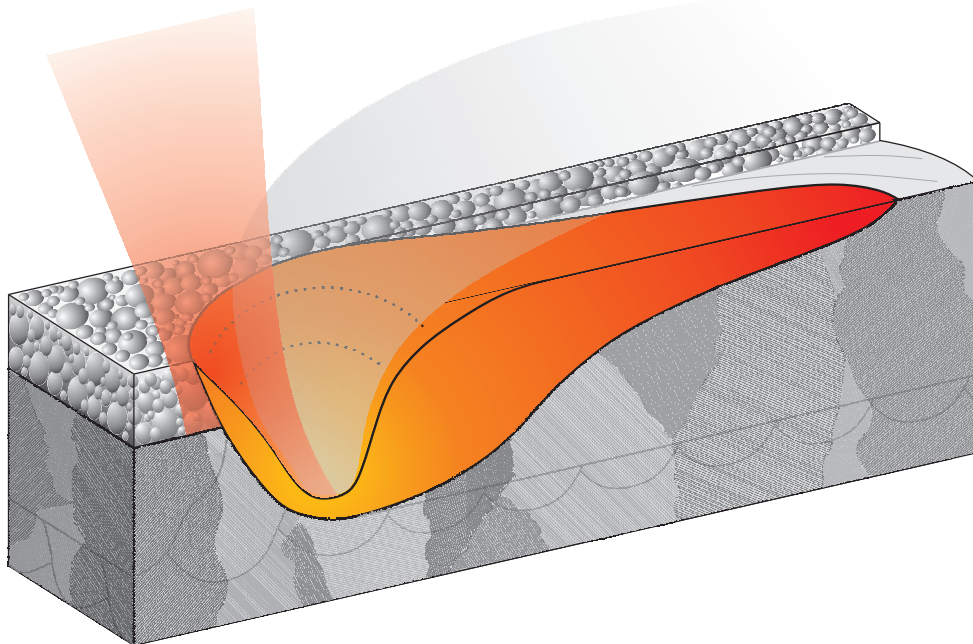


Figure 2.6: Illustration of the general trends in SLM microstructure. An alternating scan pattern is shown in which the direction of laser movement is rotated by 90° after every layer. The grains are significantly larger in build direction, but equiaxed within the plane.

Riemer et al. [79] discussed this behavior for stainless steel 316L. They show the columnar growth of grains over several layers and investigate how heat treatment can be used to reduce this anisotropy. They showed that a two hour heat treatment at 650°C even increases the grade of anisotropy because of grain growth, while a hot isostatic pressing (HIP) treatment at 1150°C and 1000 bar can induce a reconfiguration of the grain structure and therefore significantly reduce anisotropy. Niendorf et al. [71] investigated how process parameters influence the microstructure of stainless steel 316L, showing that higher layer thicknesses and higher energy densities increase the columnar grain growth. As Wang et al. [104] showed for IN718, Amato et al. [3] for IN625 and Kunze et al. [56, 27, 17] for IN738LC, the same characteristics can be found for nickel-based superalloys. Cloots et al. [17] showed that on the other hand, segregation of minor alloying elements is probable because liquidus and solidus temperature are shifted and the temperature range in between is severely increased. This is due to the non-equilibrium solidification at high cooling speeds and large temperature gradients. Titanium alloys are subject to the same columnar grain growth [25, 103, 99]. In case of aluminium alloys a less severe columnar grain growth can be observed [77, 98, 95]. Rather, multiple regions are apparent. For AlSi10Mg Thijs et al. [98] showed a columnar growth from the melt pool boundaries to the center of the melt pool's top surface, at which a equiaxed grain could be found. Thereby, the columnar growth over several layers with a strong alignment to the build direction is not formed. In case of scandium and zirconium modified aluminium alloys Spierings et al. [95] observed bands of very fine grains at the melt pool boundaries that are preventing grains from growing over several layers. Hence, aluminum alloys show less anisotropic behavior than most other common alloy systems in SLM.

These microstructural characteristics obviously define the mechanical properties. The anisotropy induces a dependency on part properties of the part's orientation within the build chamber. In general, the elongated grains result in a lower Young's modulus and yield strength as well as a higher elongation at break when loaded along the elongated direction. Loading perpendicular to it results in a higher Young's modulus, a higher yield strength and a lower elongation at break. Still, the yield strength is higher and the elongation at break lower as for cast material because of the smaller average grain size of SLM parts. To reduce this anisotropic mechanical behavior a HIP treatment is often used as a post-processing step. Thereby, comparable mechanical properties as cast material can be reached as shown by several researchers [100, 56, 112].

2.1.5 Evaporation and Spattering

Because of the rapid and extensive heating of the material by a highly focused laser beam, a fraction of the material is commonly heated up to its boiling temperature in SLM. Therefore, evaporation is a major driving force in SLM process dynamics, strongly influencing the melt pool as well as spatter characteristics [55]. While its influence on the heat flow is discussed in section 2.1.2 and its influence on the melt pool dynamics in section 2.1.3, the focus of this section is on the resulting vapor jet and its relation to spattering.

Today's common understanding of the evaporation in SLM is that it is a result of the high intensities of easily 10^6 W/cm^2 that are induced to the material by the focused laser beam. The rapid temperature increase results in severe and highly localized evaporation. Due to the evaporation a recoil pressure is induced onto the melt pool surface. The recoil pressure, which easily reaches more than 5 bar , is pushing the melt pool surface downwards, forming a strong keyhole-like dent or a keyhole as it is known from welding [47]. Ly et al. [61] showed that the actual shape is mainly dependent on the laser power and the scan speed. Furthermore, they showed that the evaporated material is leaving the irradiation zone as a vapor jet, while its direction is dependent on the actual shape of the melt pool. High powers and low scan speeds result in vertical keyholes so that the vapor jet is directed vertically as well. Medium powers or higher scan speeds result in an inclined melt pool front, leading to a rearward directed vapor jet that has a certain angle to the vertical. Bidare et al. [8] even observed a forward directed vapor jet when using very low scan speeds. They estimated the vapor jet speed to be as high as 1200 m/s and the vapor temperature to be as high as 3500 K for stainless steel. Hence, the vapor jet induces a strong flow within the surrounding gas, resulting in gas flowing to the origin of the vapor jet due to the Bernoulli effect. These flows easily reach speeds of 10 m/s and more, which is why powder particles next to the melt pool are moved around or even sucked into the vapor jet and accelerated with up to 10^6 m/s^2 [61].

Commonly three different kinds of spatter particles are being differentiated. First, melt pool spatter, often referred to as droplet spatter, which is a result of melt droplets that escape the melt pool due to high fluid flow velocities. Second and third, powder spatter either hot or cold, meaning surrounding powder particles which are entrained by the vapor jet induced gas flows. Cold powder spatter is staying in the surrounding gas flow while being ejected along the vapor jet direction. In contrast, other powder particles are moving into and along the vapor jet, resulting in rapid heating within the jet and therefore hot powder spatter as discussed by Ly et al. [61]. A fraction of the entrained particles is also consumed by the melt pool and therefore not being observed as spatter. The basic mechanisms are depicted in Fig. 2.7.

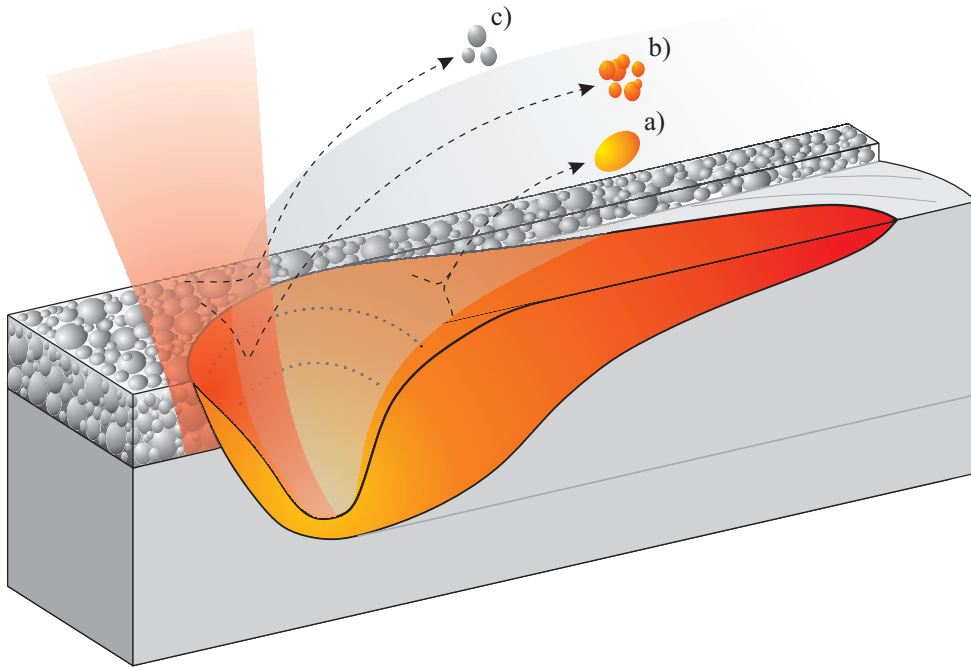


Figure 2.7: Illustration of the three characteristic kinds of spatter particles, their origin and way of travel. a) melt pool spatter, b) hot powder spatter, c) cold powder spatter (in accordance with [60, 61, 111])

Ly et al. estimated that the spatter which is observed within SLM is made up of 60% hot powder spatter, 25% cold powder spatter and 15% melt pool spatter, respectively. The spatter particle velocities are depending on the particle size, the kind of particle and the strength of the vapor jet which itself is depending on several process parameters. Different references [63, 8, 61, 111] reported velocities smaller than 5 m/s for cold powder spatter, up to 10 m/s for melt pool spatter and velocities up to 20 m/s for hot powder spatter. The difference between the melt pool and hot powder spatter velocities arise from the different sizes. Melt pool spatter is considered to be significantly larger. Spatter particle diameters three to ten times the size of the average powder particle diameter have been reported for melt pool spatter [60, 5]. Simonelli et al. [88] as well as Liu et al. [60] investigated the chemical composition and shape of spatter particles. They showed that spatter of materials with alloying elements that are prone to oxidization tend to do so, although the residual oxygen level is reduced to a minimum. The oxides can be found on the particle's surface, while the core just changes in regard to larger grain sizes due to the comparably slow cooling during the particle's flight in the gas atmosphere. The spatter particles are still mainly spherical. Some particles contain small satellites on the outside which are either particles that collided with the spatter mid-air or when landing on the powder bed.

Due to the problems that may arise because of larger, possibly oxidized particles in the powder bed or the reorganization of the particles within the powder bed due to gas flow, the amount of spatter as well as the significance of the vapor jet are commonly tried to be kept at a minimum. Mumtaz and Hopkinson [67] tried to do that by using pulse shaping, meaning the control of power over time that is emitted within the duration of a pulse. They showed that ramp-up pulses might be an option to reduce spattering. They suggested that at first the lower power level is beneficial to carefully generate a melt pool before the high power level is irradiating it. Therefore, less movement is generated within the vicinity of the melt pool. In addition, when using a low peak intensity evaporation can be reduced. Experimental comparisons to ramp-down and rectangular pulses are supporting this assumption. Matthews et al. [63] on the other hand were controlling the ambient pressure. With that they were aiming for getting rid of the entrainment of particles within the gas flow. Thereby powder spatter would be significantly reduced. They showed that within a range from about 0.5 mbar to 1000 mbar pressure within the build chamber the size of the denudation zone is significantly different, meaning the zone in which powder particles are pushed away or sucked in by the induced gas flow. The results showed that working with low pressures is problematic because the denudation zone tends to increase with decreasing pressures. But at pressures below about 10 mbar a change in the vapor jet dynamics could be observed. For pressures lower than that the vapor jet starts to push in all directions instead of being directed rearwards. This results in powder particles being pushed away from the track instead. But at about 3 mbar argon atmosphere a sweet spot could be found, at which the effects of gas being sucked in due to the Bernoulli effect and being pushed away due to evaporation at low pressures negate each other. Therefore, a minimum sized denudation zone could be found. Since at this point no powder is carried to the melt pool anymore, problems with the resulting track height arise [63].

Summarizing this section, the following key aspects should be kept in mind.

1. Severe evaporation takes place in SLM due to the highly focused laser beams and its high intensities, respectively.
2. Evaporated material is leaving the irradiation zone with speeds faster than 1000 m/s , resulting in surrounding gas flows of 10 m/s and higher that are directed to the origin of the vapor jet (except for very low ambient pressure).
3. Three kinds of spatter may arise because of that. Melt pool spatter, hot powder spatter and cold powder spatter, with hot powder spatter commonly being expected to be the largest fraction.

2.1.6 Residual Stresses and Distortion

High thermal gradients as well as rapid heating and cooling are increasing the risk for high residual stresses and distortion in SLM parts. The common understanding of the build-up of residual stresses is based on two main effects. The first one is the temperature gradient mechanism (TGM) that leads to higher residual stresses for higher temperature gradients and is known from the laser bending process and reported to be the main driver in SLM in several publications [65, 110, 54, 85]. Due to the laser beam the material rapidly heats up resulting in a need to expand. But since the material stiffness is decreased by the high temperatures, the expansion is largely prevented by the colder surrounding material. So, strains are mostly induced within the heated material. As soon as the elastic strain limit is reached the material is plastically compressed. If the material melts the strains are neutralized in the molten material. After the laser passed by, the material cools down and shrinks. Since during melting plastic strains within the melt pool were equalized, the strains do not equal out but tensile residual stresses are left in the area of rapidly heated and cooled material. The second effect is not independent of the first one but considered to increase this effect. Mercelis et al. [65, 54] called it the cool-down phase effect which induces tensile stresses to the newly added track or layer because of the shrinkage during solidification and cooling that is constrained by the underlying layers. Shiomi et al. [86] supported this theory simulatively. It is proven by several methods [65, 110, 54, 86, 13, 36] that these two effects lead to significant residual tensile stresses as high as the material's yield strength in the uppermost layers of SLM parts. The layers below are influenced by the compressive stresses that are induced by following layers and possible stress relief due to an elevated temperature.

The layer-wise superposition of old and new stresses is resulting in a complex stress field within the part. Thereby, cutting a perfectly fine part of the support or build plate can result in severe distortion, leaving the part useless. Therefore, heat treatment of the parts is a common post-processing step before cutting the part of the build plate. The effect of unfolding distortion due to residual stresses when cutting of the part is commonly used to quantify the processing strategies influence on residual stresses. To do so, cantilever samples are built which are connected to the build plate. With cutting the support the residual stresses are released and the distortion of the cantilever can be used as an indicator for residual stresses as shown in various publications [110, 74, 68]. Direct measurement of residual stresses in SLM parts is possible as well. Available techniques are the hole drilling method, x-ray diffraction and neutron diffraction, with neutron diffraction certainly being the most complicated but as well most detailed way [11, 4].

2.1.7 Defect Generation

The aforementioned processes and effects are all contributing differently to various kinds of defects within SLM parts. Commonly two different basic microstructural defects can be differentiated, porosity and cracking. Both should be avoided as good as possible to achieve good geometrical accuracy, especially cracking of support structures, and mechanical properties. An overview of defects is illustrated in Fig. 2.8.

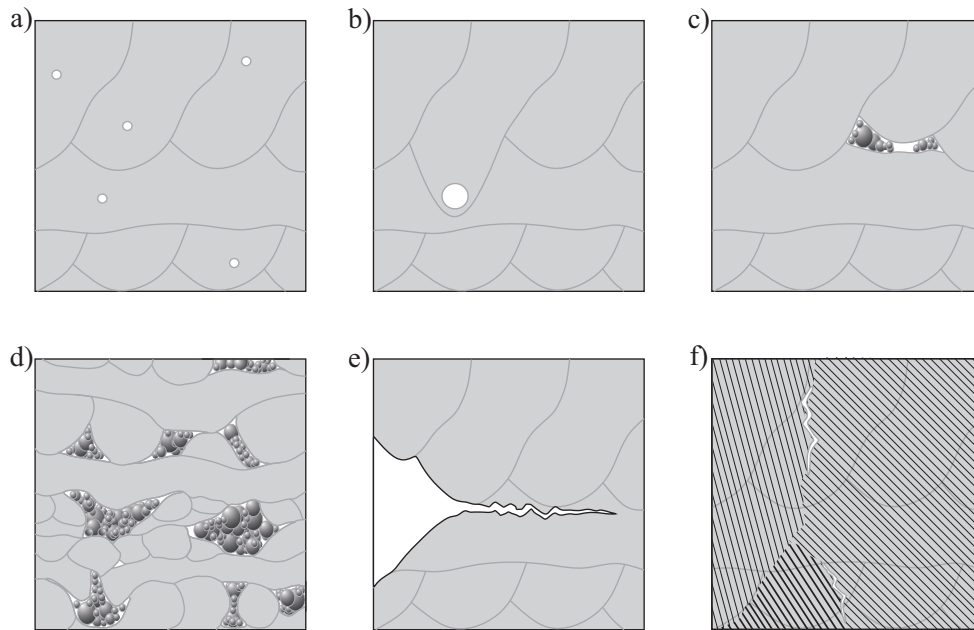


Figure 2.8: Overview of different defects. a) spherical porosity due to entrapped gas in particles, b) spherical porosity due to entrapment at keyhole collapse, c) slight lack of fusion (random error), d) severe lack of fusion (wrong process parameter set), e) cold cracking and f) hot cracking (here cracking at grain boundaries)

Everything that is reducing the overall density is considered porosity as long as it is no crack. Hence, there are different reasons for different kinds of porosity in SLM. One can differentiate irregular shaped pores, that are filled with unmolten powder particles, due to a lack of fusion and spherical pores due to entrapped gas [113, 97, 43]. Lack of fusion is the most common kind of porosity because its main reason is the use of too low powers as discussed in several publications [7, 28, 106]. There are different ways for lack of fusion to arise when using low powers. Bauereiss et al. [7] showed for electron beam melting that one aspect is the reduction of the melt pool wetting capabilities at low powers which results in spherical melt pool cross sections with high contact angles. For even stronger magnitudes, in which the melt pool results in a drop-like structure, the effect is called “balling”. In that case the Rayleigh-Plateau instability takes control of the insufficiently wetting melt pool,

which means that the surface energy is reduced by splitting a long cylindrical melt pool into several drop-like ones. Those melt pools significantly increase the inhomogeneity of the top surface. Thereby, the following powder layer is defined by strong variations of its thickness. With a layer thickness larger than the anticipated one, the risk of powder being not melted due to insufficient heat input increases. This can even lead to a self-enhancing effect, resulting in vertically growing porosity [7]. The case of higher layer thicknesses can also arise by errors of the recoating device or random spatter particles that drop on the not yet irradiated powder bed. Therefore, the defect mechanism is not self-enhancing in these cases. Furthermore, insufficient heat input might as well occur if the laser beam is attenuated by spatter particles that cross its path.

The reasons for gaseous pores differ more, with three different effects being observed so far. First, comparably small gas entrapments can be found due to residual gas within the powder particles that are used for the powder bed. Powder suppliers try to get rid of that but have not yet reached a perfect success rate. Therefore, a small amount of gaseous pores remains in every powder and every additively manufactured part as reported by Bauereiss et al. [7]. Second, keyhole porosity can be observed within SLM parts if high energy densities are used. With high energy densities the melt pool depth increases significantly as soon as the deep penetration welding regime is reached. Within this regime the keyhole tends to frequently collapse due to melt pool dynamics or fluctuations of the incoming laser power. In that case, the gas at the bottom of the keyhole is commonly entrapped because of rapid solidification of the melt pool as discussed in several cases [28, 113, 97, 43]. Kasperovich et al. [43] showed that the amount of keyhole porosity is even increasing linearly with increasing energy density as soon as a certain threshold is passed. Third, as Weingarten et al. [106] reported, humidity in the powder bed can induce another source for gaseous pores, especially within aluminium parts. They show that humidity within the powder bed is solved within the melt pool. Since the solubility is far lower within the solidified material, hydrogen is being enriched at the solidification front and hence small bubbles are formed and entrapped within the part. When comparing the influence of irregular shaped and spherical porosity on mechanical properties it should be noted that spherical pores are less problematic. Gong et al. [28] reported that spherical porosity of even 1% is not significantly reducing tensile properties. In contrast, 1% of irregular shaped porosity might result in brittle material behavior. As Kabir et al. [41] showed simulatively, the reason for that might be that for spherical pores the stress concentration is distributed equally over the pore surface and not concentrated to some edges.

For cracking also two major effects have to be differentiated which are both a result of high residual stresses within SLM manufactured parts. First, cold cracking at which the residual stresses are higher than the ultimate tensile strength (UTS) of the alloy. And second, hot

cracking at which the UTS is locally reduced because of the segregation of low melting low strength elements. Cold cracking can basically occur within all SLM parts if the geometry is not supported correctly. Most often it is observed for high carbon steels and titanium alloys due to martensitic solidification [114, 45]. The cracks are comparably large and are commonly starting from the sides of the part or other microstructural defects. In contrast, hot cracking is commonly found in nickel-based superalloy parts with equally, or even periodically, distributed cracks of a few hundred microns each [26, 56, 3]. Therefore, cold cracking commonly leads to unacceptable parts, while hot cracking can be handled with post-processing steps like hot isostatic pressing.

Summarizing, when thinking about defects in SLM parts, one should consider the following.

1. Two kinds of porosity can be found. First, irregular shaped pores due to lack of fusion as a result of too high layer thicknesses or too low power. And second, spherical porosity due to too high powers (keyhole porosity) or entrapped gas that originates from powder particles or humidity within the powder bed.
2. Two kinds of cracks can be found. First, large cold cracks which leave the part unusable and can be observed if the stresses surpass the UTS of the alloy. Second, smaller hot cracks at which low strength elements are locally segregated during the solidification.
3. Spherical defects are more forgiving regarding the tensile properties of a part.

2.2 Simulation of the SLM Process

As discussed in the previous section, there has already been some effort to model the SLM process with the goal to deepen the understanding of it. Two basic approaches can be found due to different time scales and dimensions as well as the resulting computational effort. While the first numerical models were only investigating the thermal behavior on either the scale of a single track or a part, most of recent research can be classified into combined thermal and fluid dynamics modeling or thermal and structure mechanics modeling. Therefore, either the melt pool dynamics on the scale of a single track or residual stresses and distortion of larger geometries are the topic of interest in these works. Purely thermal models are not discussed in the following because thermal models are the basis of the latter two approaches and are therefore included in all of them. Some ideas of multi-scale approaches and some publications about the simulation of microstructural evolution are available as well, but are not discussed in the upcoming subsections.

2.2.1 Simulation of Fluid Dynamics

The simulation of the fluid dynamics within the melt pool can be used to predict the melt pool dimensions. These can be used to estimate the usefulness of the investigated parameter sets in the process. But the previous section shows that the melt pool is subject to a range of physical effects that induce a highly dynamic fluid flow. So, to numerically model the melt pool to get further information about the dynamics of the melt pool and the resulting dimensions one has to take care of those. Therefore, a good absorption model, a differentiation between powder, melt and solid as well as surface tension and evaporation driven flows have to be implemented. Furthermore, the availability of temperature-dependent material properties over the range from room to evaporation temperature is necessary. And putting these necessary effects together within one simulation tool is computationally expensive, which is why only few detailed fluid dynamics models have been published. The ones worth noting in SLM are of the group around Khairallah et al. [46, 49, 47, 61], of a group around Gu et al. [109, 20, 21, 108] and a recent publication by Lee and Zhang [58] as well as for EBM the work within the group of Koerner et al. [51, 62, 78]. Therefore, those models are discussed in the following to get an overview of the current state of the art.

Khairallah et al. started with a detailed representation of the powder bed. They used a self-developed particle packing algorithm which is positioning different-sized powder particles within the powder bed until a certain packing density is achieved. The layer thickness was controlled by deleting all particles that cross the chosen layer height [49]. Although Boley et al. [9] showed that this tool can be used to assemble a detailed representation of the powder bed, the detail was reduced in the framework of melt pool simulation by taking out particles smaller than a certain size. Because otherwise the mesh size of the simulation would need to be refined until the computational effort makes the simulation tool impractical to use. With a chosen mesh size of $3\ \mu\text{m}$ the resulting computational effort already reached the order of $100'000\ \text{CPUh}$ for a $1\ \text{mm}$ track [46]. Yet, by leaving out the smaller particles it is probable that the influence of the particle placement on the melt pool dynamics, especially in the outer melt pool regions, is overestimated. The absorption was modeled using a simplified ray-tracing technique that stops tracking the ray after its first encounter with a powder particle. Thereby absorption on the highly complex powder bed surface could be realized but the propagation of the rays into the powder bed due to multiple reflection and therefore an increase in absorptivity was neglected [47]. Buoyancy, capillary and recoil pressure induced forces were considered within the momentum equation of the Navier-Stokes equations which are solved using a splitting of operators approach within a arbitrary Lagrangian-Eulerian method. The Marangoni effect was mimicked by

a similar process that is driven by density gradients, but no more detail was given on this implementation [46]. By using this detailed representation of the powder bed and the fluid dynamics inducing effects the numerical model allowed to investigate the complete range of effects that are coupled to the melt pool dynamics, meaning for example spattering, residual porosity or balling. The model's main issue is the incredibly high computational effort and the fact that until now no quantitative validation has been published. Rather, single cross sections or single effects that have been imaged by a high speed camera have been used to show a similarity to the simulation. Nevertheless, the results seem to be reasonable and the model can currently be considered to be the most detailed one.

Gu et al. started off with modeling the powder bed as a continuum but recently progressed to a more detailed representation of the powder bed as described by Xia et al. [108]. They used a single layer of same-sized powder particles that were randomly distributed on the substrate. Therefore again, an overestimation of the influence of the particle distribution and shape has to be assumed. A three dimensional Gaussian heat source model was used as an implementation for the absorption of laser energy. Therefore, a constant absorptivity was assumed and connected with a Beer-Lambert extinction coefficient to imitate the reduction of laser energy deeper within the powder bed [21]. Thereby, the laser energy was induced within a volume and not onto a surface. The fluid flow simulation was done using the commercial software tool "fluent" which solves the Navier-Stokes equations using a volume of fluid (VOF) approach. They as well elaborated the main effects, meaning buoyancy, Marangoni and capillary forces as well as recently recoil pressure induced surface forces [30, 108]. Thereby, a good approximation of the melt pool dynamics can be expected. They used the numerical model to investigate the influence of the melt flow onto the distribution of strengthening particles within the final part as well as surface roughness [109, 108]. Looking at the numbers of the most recent publication, the melt pool velocities seem reasonable but the temperatures comparably low and no effect of the evaporation on the melt pool shape seems to be present. Furthermore, no quantitative validation has been published until now. This leaves at least some open questions about the quality of this numerical representation of the process.

Lee and Zhang [58] as well used a detailed powder bed which was generated by the rain-drop method and the use of a discrete element method. Therefore, particles of different sizes, equivalent to the desired particle size distribution, were randomly positioned within a container and freely dropped onto the substrate resulting in a packed powder bed. To control the powder bed density single particles can be deleted until the desired value is achieved. They as well used a Gaussian volume heat source for energy input and include the previously discussed effects that are necessary for a detailed representation of the process. Due to the use of a commercial solver, "Flow3D" which uses a VOF method, the

calculation times are very low, in the range of a some 10 *h* per 1.8 *mm* scan track. A small quantitative validation is available that shows a good accuracy of the simulation with an error of less than 10%. Sadly, the validation is based on two single melt pools that were taken out of a cubic sample. Thereby, stochastic effects are completely neglected and it has to be questioned how the two experimental melt pools have been chosen. But the overall effects and numbers seem reasonable, although the melt pool and keyhole-like dent seem to be too spherical for the used parameter sets. As well, the fact that a two track simulation was performed has to be noted. With that the influence of the asymmetric behavior of the melt pool with powder on the one and bulk material on the other side could be mimicked.

The work of Koerner et al. [62] has to be discussed as well, although the focus is on electron beam melting. That changes the modeling, for example evaporation can be neglected without any harm, and thereby the dynamics of the melt pool change as well, but their modeling is interesting because it significantly differs from the previously mentioned ones. First, they commonly used a two dimensional representation in which the electron beam is always moving perpendicular to the modeled plane to keep the computational effort low, although a three dimensional representation is available. But second, they were investigating multi-track, multi-layer processes, thus being able to investigate larger scale effects of the melt pool dynamics [78]. The two dimensional initial material configuration was achieved by the rain-drop method [51], similar to the one of Lee and Zhang. The fluid flow field was solved by using a lattice Boltzmann model with a volume of fluid approach for free surfaces and buoyancy, Marangoni and capillary forces were implemented. The detailed two dimensional model offered the chance to investigate the influence of previous tracks and layers on the current melt pool like the defect growth over several layers as discussed in section 2.1.7.

Other models are available as well but often fall short regarding some physical effects, especially evaporation and recoil pressure induced forces on the surface in the very front of the melt pool. The presented models are following a trend of using a detailed representation of the powder bed to account for the randomness of the particle distribution, but lack a comprehensive, especially quantitative, validation. Either way, the models show the power of representing the physical effects within and around the melt pool and are a useful way of getting more information about these processes.

2.2.2 Simulation of Residual Stresses

The influence of residual stresses on the quality of a part has to be evaluated on larger scales, at least a single layer, because with every new irradiated track the stress field is changed. Therefore, the models can be classified regarding the investigated scales, either single layers or a part. Additionally, depending on the chosen scale different assumptions and simplifications are necessary to handle the computational effort. The larger the scale, the more simplifications are commonly necessary.

Single layer simulations are used to evaluate the influence of scan strategies on the layer's residual stresses. In case low residual stresses within a single square layer are achieved, it is assumed that the tendencies are the same for larger parts. The amount of elements for a thermo-mechanical simulation of a single layer is comparably easy to handle with today's computational power if fluid dynamics are neglected, which is why less simplifications are necessary. Cheng et al. [14] and Parry et al. [75] showed that the heat source can be modeled as a Gaussian volume heat source and that the complete irradiation process can be simulated, meaning the line-wise movement of the heat source on the modeled material configuration. Thereby, the heat accumulation and its influence for different scan strategies can be evaluated. But most current simulation models go a step further and simulate the residual stresses within a complex part, which can be used to pre-compensate the distortion or to optimize the support structures, so that distortion can be kept at a minimum. A small amount of publications are investigating the part scale by still using a moving heat source as it is done for single layer simulations. The increased computational effort is compensated by adaptive meshing strategies [23] or massive parallelization [35]. The more common way of simulating on part scale is by using a multi-step approach. For that, first a single line's temperature field is simulated and super-positioned to a single layer [74, 44, 68] or a single layer's temperature field is simulated [52, 10]. The heat source is often modeled as a Gaussian volume heat source or as a Goldak heat source which is known from welding simulations. Secondly, the part is loaded with the calculated layer's temperature field over and over again to estimate the final part's residual stresses. Another, even faster option is to skip the thermal modeling and load the model with equivalent strains, as explained by Alvarez et al. [2]. Yet, in these cases no heat accumulation or annealing processes as well as their influence on the stresses can be accounted for. Either way, all of these modeling strategies are said to result in good approximations of the final part's residual stresses and distortion as summarized by Schoinochoritis et al. [84].

In contrast to the simulation of melt pool dynamics, there are already a lot of commercial software tools available to simulate the residual stresses on part scale by elaborating the previously discussed strategies. These suppliers used the knowledge gathered within other processes that strongly suffer under thermo-mechanical effects, e.g. welding, to quickly respond to the market's needs for AM-dedicated tools.

2.3 Improving the SLM Process

The problems that are discussed in the sections 2.1.5, 2.1.6 and 2.1.7 require to be overcome within the build-up process because getting rid of them afterwards is either expensive, regarding costs as well as time, or impossible. Changing scan strategies to improve the process has shown itself to be not sufficient. Also, the scan strategies that have shown some potential to reduce residual stresses often include multiple irradiation of every single layer [65, 54, 86, 53] so that productivity is decreased significantly. Hence, other strategies are currently in focus of improving the process of melting and solidification itself, especially the preheating of the build plate as well as changes on the side of the laser source. While the option of preheating the build plate or the build volume can be found on nearly any current commercial SLM machine, changes on the laser side are limited to laboratory machines. Process monitoring and control as well is a topic of high interest within the SLM community, but it is not related to any topics of this thesis and therefore not discussed in the following.

Preheating of the build plate is known to be an option to influence the microstructure as well as to reduce residual stresses and thereby reduce cracking and distortion. Shiomi et al. [86] measured up to 40 % less residual stresses, with a strain gauge placed on the bottom of the build plate, for preheating temperatures of 160 °C when processing a steel-nickel-copper powder mixture. Kruth et al. [54] showed a reduction of the bending angle of bridge structures by 10 % when heating the base plate to 180 °C while processing stainless steel 316L. For M2 high speed steel Kempen et al. [45] showed that at 200 °C base plate temperature no more cracking occurs and Zumofen et al. [114] showed that at 400 °C distortion is reduced to a minimum. Furthermore, Mertens et al. [66] showed that in case of hot working steel H13 a base plate temperature of 400 °C can make heat treatment obsolete regarding tensile properties. On the other hand, Mertens et al. showed that in case of H13 a reduced martensitic transformation reduces the amount of compressive stresses that are induced by this transformation due to the volume increase at phase transformation. This results in a linear increase of residual stresses in the top surface from about -300 MPa to about 400 MPa . Furthermore, microhardness is reduced. Li et al. [59] investigated the influence of temperatures in the range of 150 °C to 350 °C on a titanium alloy and showed that higher temperatures result in larger grains and a stronger anisotropy. Additionally, Demir and Previtali [22] showed that heating the base plate to 170 °C reduces the microhardness of the maraging steel 18Ni300 by more than 10 % and increases the radial error of cylindrical samples by about 30 %.

Summarizing this information, preheating the base plate can be an option to reduce residual stresses and cracking for a range of materials while one has to accept the change in microstructure and therefore a change in mechanical properties. Still, the positive effects

of reduced thermal gradients outweigh the negative ones as long as the part can be built without any important defects because the microstructure is commonly changed by a post-process heat treatment. Rather, the fact that all parts as well as the surrounding powder material is heated to high temperatures and has to cool down afterwards has to be evaluated. Although the additional heat can be used to speed up the process, cooling down the material within the machine can significantly increase the processing time. Furthermore, no flexibility is available for different part geometries.

Changes of the laser intensity profile have to be classified into temporal (pulsed mode) and spatial (beam shaping) changes. The use of ultrashort laser pulses in SLM is a recent approach to make elements with high melting points, high thermal conductivities or high reflectivity like tungsten or copper processable. Ebert et al. [24] and Nie et al. [69, 70, 6] showed that femtosecond pulses can be used to achieve the necessary pulse energies for melting tungsten, rhenium or ceramics to single layers or parts. Still, as Kaden et al. [42] discussed for the case of copper, the pulse energy has to be adjusted carefully so that the ablation threshold is not reached. In fact, the necessary heat to melt the material has to be accumulated within the powder over several pulses. Therefore, high repetition rates, in the megahertz range, are beneficial to stay below the ablation threshold but induce the necessary heat within a short time. And as already discussed in section 2.1.5 the use of pulse shaping can beneficially influence the spattering behavior when ramp-up pulses are used, because those are carefully melting the material before the peak power is reached [67]. When using beam shaping the intensity profile of the laser beam is rearranged. Thereby it is assumed that the melting and solidification behavior can be influenced beneficially. Okunkova et al. [72] showed that top-hat as well as donut profiles reduce the amount of evaporation and spattering due to lower peak intensities. Thereby, the amount of movement within the powder bed is reduced as well. Okunkova et al. suggested that this can have a positive effect on part accuracy because irregularities within the powder bed are reduced. And since the peak intensity is reduced top-hat as well as donut profiles result in more shallow but wider melt pools. Cloots et al. [18] supported the findings of more shallow but wider melt pools, which seem to reduce the hot cracking susceptibility of the nickel-based superalloy IN738LC.

These results show that changing the laser intensity profile either temporally or spatially can significantly influence the process to either widen the range of materials or to stabilize it for common materials.

Chapter 3

Research Gap

The selective laser melting process still needs improvement regarding productivity, robustness and quality, although a wide range of the process dynamics are mostly understood. The knowledge of the process indicates that it is important to get the high dynamics in the vicinity of the melt pool under control. Yet, while doing so, the flexibility of the process shall not be restricted, so it's still possible to benefit from the processes' full potential. Since the high thermal gradients and the intensity profile of the laser beam have the greatest impact on the process dynamics, working on the intensity profile seems to be a reasonable choice. Still, beam shaping does not offer the necessary spatial flexibility that one might wish for, which is why the use of two independent laser beams is proposed which can be synchronized to adjust the temperature field in the vicinity of the melt pool as needed. Abe et al. [1] even tried using a fiber and a CO2 laser for SLM in 2001 but did not investigate it further, yet similar approaches are known from welding technologies. With the first preliminary experiments Abe et al. showed that by using two beams with different beam diameters in a defined offset mechanical properties of metal parts can be enhanced. Since laser as well as scan head technologies improved significantly in the last years, this approach is picked up again in this thesis to investigate in detail how the process is influenced and what improvements can be achieved.

3.1 Objectives and Work Packages

The objectives of this thesis can be defined as developing an SLM process in which two laser beams can work synchronously on the same part and to use it to understand and quantify how these strategies are influencing basic key indicators. To do so the following work packages are necessary.

1. The state of the art shows that understanding the process dynamics without numerical support is close to impossible. Consequently, a simulation tool needs to be developed that is capable to reproduce the high process dynamics. As discussed in section 2.2.1, a coupled thermal and fluid flow simulation is a good choice to do so. Special attention has to be paid to the absorption modeling to achieve a detailed representation of the temperature field. Yet, the computational effort has to be kept at a minimum. The numerical model has to be validated qualitatively as well as quantitatively to make sure that it offers a sufficiently detailed representation of the process. The basic equations, algorithms and approximations are described in the upcoming chapter 4.
2. Since no commercially available machine offers the possibility to work with two laser beams on a single part in a synchronized manner, a laboratory machine has to be developed that is capable to take care of all essential functions that are necessary for the SLM process. A proof of concept has to be performed to evaluate the capabilities of hardware and controls. The concept, setup and start-up of the laboratory machine as well as other necessary tools and methods are discussed in chapter 5.
3. Using two beams in a synchronized manner is the core of this thesis and will thus be investigated in detail. To understand the influence of the applied changes to the temperature field, simulation as well as experiments are taken into account. The influences are discussed on the basis on the key indicators of microstructure, density, spattering, surface roughness and distortion in chapter 6.
4. While the previous work packages shall use a very well established and investigated SLM material, stainless steel 316L, it is necessary to see whether possible improvements are transferable to other alloys and can offer the chance to widen the material range by getting rid of some of the process' drawbacks. This is discussed on the basis of crack susceptibility of a higher carbon content steel in chapter 7.
5. The influences and possible improvements need to be discussed on the basis of the complexity and costs of the two-beam setup to evaluate if this approach might be an option for industrial application or if alternatives might offer the same result. This is done in chapter 8.

In consequence, the following chapters start with the explanation of the numerical modeling and are followed up by the experimental setup, methods and tools to experimentally as well as numerically investigate the two-beam strategies before checking the transferability of the strategies to another alloy. The thesis closes with a discussion about the potential and applicability of these strategies for industrial processes.

Chapter 4

Numerical Modeling

The upcoming sections describe the numerical model starting with the basic idea, followed by the modeling of the heat as well as fluid flow and closing with a validation of the resulting simulation tool so that in the end of this chapter the question is answered whether the tool is fit to be used for further investigations into two-beam strategies or not.

4.1 Concept

A two step approach of heat and fluid flow simulation is chosen which elaborates a weak coupling. This means that heat and fluid flow are calculated after one another and that the results of one calculation are used as the input of the other one. Thereby, more flexibility in choosing the solvers for each problem can be accomplished because both problems do not need to converge at once but after one another, which means that even a combination of an explicit and an implicit method can be elaborated. This is exactly what is done within the modeling which is presented in the following. While the temperature field is calculated based on an explicit finite difference scheme, a combined level set volume of fluid (CLSVOF) method and an implicit pressure implicit splitting of operators (PISO) solver are used to calculate the fluid flow.

Hence, absorption, heat flow due to conduction, convection and radiation as well as melting, solidification, evaporation and the change of temperature dependent material properties are considered within the temperature field simulation. Those result in an update of the temperature field, the elements' states as well as material properties. Taking these as input parameters for the fluid flow simulation, first the surface of the melt pool is reconstructed to get the material configuration, so that capillary forces can be calculated and placed at the correct positions, together with other surface forces. Surface and body

forces as well as the material properties and state are the input parameters for the fluid flow solver. The resulting fluid flow field is then used to calculate the volume and heat flow due to convection within the melt pool which results in an updated temperature field as well as updated material properties, states and configuration. Here and in the following the heat flow due to melt flow is considered to be a part of the fluid flow simulation rather than being part of the temperature field simulation because it is directly linked to the volume flow which is the result of the fluid flow calculation. The updated material properties, states and configuration as well as the updated temperature field are needed for the next iteration that again starts with the calculation of a new temperature field. A simplification of this procedure is illustrated in Fig. 4.1.

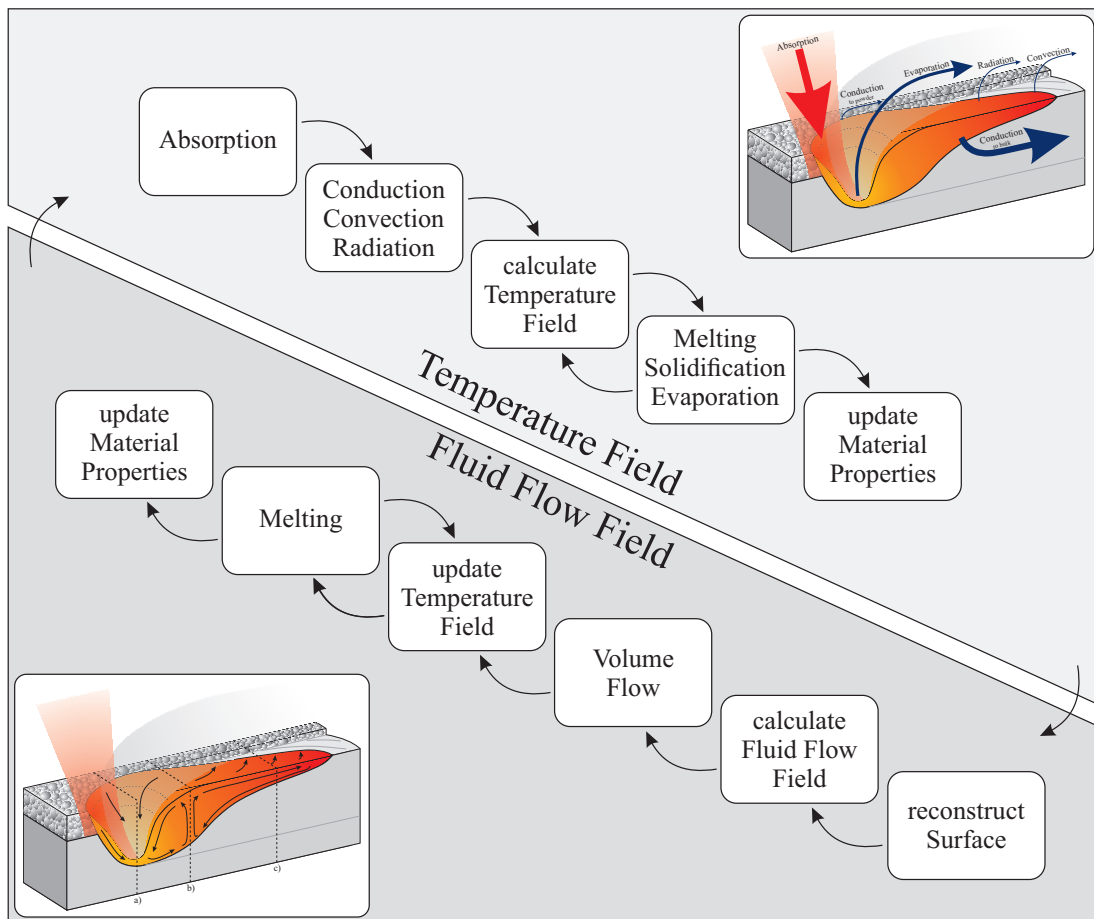


Figure 4.1: Illustration of the concept of the simulation tool. Temperature and fluid flow simulation are modeled by elaborating a weak coupling. The results of each step are used as input parameters for the other step. While the fluid flow simulation requires the updated temperature field, material properties and state, the temperature field simulation needs the current material configuration for a more precise calculation of absorbed power as well as the updated temperature field and material properties and states due to melt pool convection.

The methods are used on a three-dimensional staggered grid of cubic elements, which means that material properties as well as most state variables are fixed to the elements' center points, while fluid flow velocities are located on the elements' faces. The powder bed is implemented as a continuum of equally filled elements with a filling degree equal to the desired powder bed packing density. When the powder melts the powder bed consolidates to a melt pool because the material is filling up the lower, partly filled elements. Thereby, the upper elements are left empty.

4.1.1 Initial Configuration

The initial configuration is defined by this homogenized powder bed located next to a ideally solidified, previous track. Hence, the asymmetric behavior of multi-track experiments can be investigated easily, although no heat accumulation is accounted for. The initial configuration is illustrated in Fig. 4.2. The beam is simulated to be moving along the center line of this configuration.

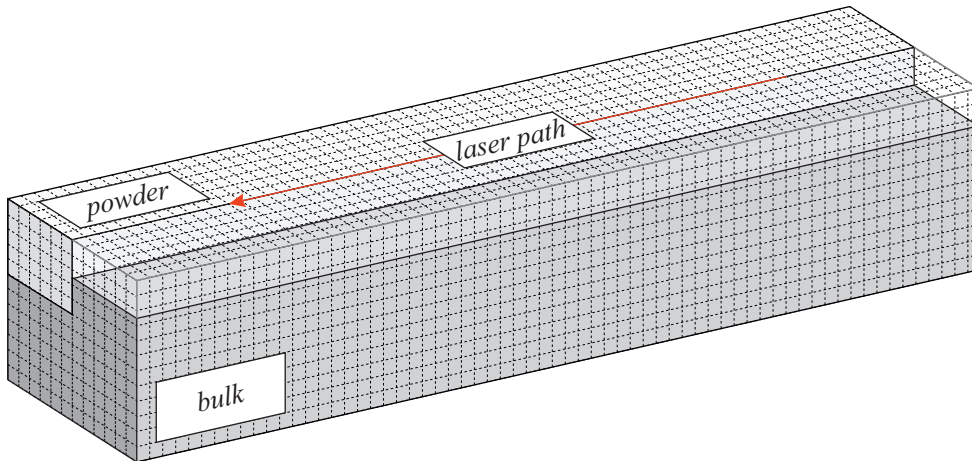


Figure 4.2: Illustration of the meshing and the initial material configuration that is used for the simulation of a single track next to an already solidified track. The height of the already solidified track is approximated as the powder layer height times the powder bed packing density.

Thermal conductivities, during the fluid flow simulation, as well as densities and viscosities of not completely filled elements are weighted with their filling degree F .

$$\alpha(T) = F \cdot \alpha_b(T) + (1 - F) \cdot \alpha_g \quad (4.1)$$

With $\alpha_b(T)$ representing the temperature dependent bulk material property and α_g the equivalent gas property. Temperature-dependent material properties are interpolated be-

tween the given data points. The thermal conductivity of the powder bed is handled separately, since as earlier discussed multiple studies have shown that the thermal conductivity of a powder bed is significantly smaller [87, 80]. Therefore, the thermal conductivity within the powder bed is fixed to a value of 0.2 W/m K . The value is changed to the temperature-dependent bulk value as soon as the powder melts. Material expansion is not considered and thus the density is kept constant over temperature.

4.2 Modeling Heat Flow

The temperature change is the result of the balance of heat flows and can be calculated according to Eq. (4.2). Since heat flow due to melt pool convection is considered within the fluid flow model, at this point the balance of heat flows accounts for absorbed power P_{abs} , conducted heat \dot{Q}_{cond} in x, y and z as well as heat loss due to radiation \dot{Q}_{rad} and convection to the surrounding atmosphere \dot{Q}_{conv} . Hence, the element's predicted temperature of the current time step T_{pred}^n

$$T_{pred}^n = T^{n-1} + \frac{P_{abs} + \dot{Q}_{cond,x} + \dot{Q}_{cond,y} + \dot{Q}_{cond,z} + \dot{Q}_{rad} + \dot{Q}_{conv}}{\rho \cdot c_p \cdot F \cdot V} \cdot \Delta t \quad (4.2)$$

is calculated based on these heat flows as well as the temperature of the previous time step T^{n-1} and is then used to evaluate melting, solidification and evaporation as explained in subsection 4.2.3. In these cases T_{pred}^n is corrected to comply with these effects. Additionally, Δt is the time step size, ρ the material's density, c_p the specific heat capacity, V the element volume and F the filling degree of this element. The boundary conditions are allowing heat to flow out of the model at the sides and bottom while being insulated at the top.

4.2.1 Absorption

As discussed in various earlier sections, an accurate absorption model is the key to a detailed representation of the process. Since a homogeneous powder bed makes using ray tracing impossible, the absorption model of Gusarov et al. [31, 33] is used and numerically improved to calculate the detailed three-dimensional power input. It calculates the three-dimensional power distribution as follows.

$$\begin{aligned}
P_{abs}(x, y, \xi) = P_0(x, y) \cdot \left\{ \frac{r a}{(4r - 3) D} [(1 - r^2)e^{-\lambda_{opt}} [(1 - r)e^{-2a\xi} + (1 + a)e^{2a\xi}] \right. \\
- (3 - re^{-2\lambda_{opt}}) \cdot [(1 + a + r(1 - a))e^{2a(\lambda_{opt} - \xi)} \\
\left. + (1 - a - r(1 + a))e^{2a(\xi - \lambda_{opt})}] \right] - \frac{3(1 - r)(e^{-\xi} - re^{\xi - 2\lambda_{opt}})}{4r - 3} \left. \right\}
\end{aligned} \quad (4.3)$$

$P_0(x, y, \xi)$ is the power input at the surface of position (x, y) and dimensional depth ξ which is the product of the depth z and the extinction coefficient β . a , D and the optical thickness λ_{opt} are derived on the basis of the hemispherical reflectivity r as well as the powder bed properties of relative powder layer density ρ_{pl} , powder layer height h_{pl} and mean powder particle diameter d_{pp} as explained in [33].

$$a = \sqrt{1 - r} \quad (4.4)$$

$$\beta = \frac{3}{2} \cdot \frac{\rho_{pl}}{1 - \rho_{pl}} \cdot \frac{1}{d_{pp}} \quad (4.5)$$

$$\lambda_{opt} = \beta \cdot h_{pl} \quad (4.6)$$

$$\begin{aligned}
D = (1 - a)[1 - a - r \cdot (1 + a)]e^{-2a\lambda_{opt}} \\
- (1 + a)[1 + a - r \cdot (1 - a)]e^{2a\lambda_{opt}}
\end{aligned} \quad (4.7)$$

The detailed derivation of these equations can be found in the publications of Gusarov et al. [31, 33]. It is based on solving the radiation transfer equation

$$\mu_{opt} \frac{\partial I(z, \mu_{opt})}{\partial z} = \beta \cdot \left(\frac{\omega}{2} \int_{-1}^1 I(z, \mu'_{opt}) \cdot P(\mu'_{opt}, \mu_{opt}) d\mu'_{opt} - I(z, \mu_{opt}) \right) \quad (4.8)$$

for collimated incident laser power normal to a thin powder layer. With $\mu_{opt} = \cos \theta$ and θ being the radiation propagation angle, ω the scattering coefficient, $I(z, \mu_{opt})$ the depth resolved intensity and $P(\mu'_{opt}, \mu_{opt})$ the scattering phase function. As discussed in subsection 2.1.1, Gusarov et al. use a two-flux approach to solve the radiation transfer equation. Therefore, $I(z, \mu_{opt})$ is split into a flux which is propagating deeper into the powder layer $Q_+(z)$ and a flux which is leaving the powder bed $Q_-(z)$ because of reflection. Furthermore, a scattering term $S(z, \mu_{opt})$ is included to account for multiple reflection in the powder bed. This results in Eq. (4.9), with δ being the Dirac delta function as discussed in [33].

$$I(z, \mu_{opt}) = \frac{Q_+(z)}{2\pi} \delta(\mu_{opt} - 1) + \frac{Q_-(z)}{2\pi} \delta(\mu_{opt} + 1) + S(z, \mu_{opt}) \quad (4.9)$$

The equation can be used to solve the radiation transfer equation when taking boundary conditions at the powder and substrate surface into account as well as assuming geometrical optics.

The main issue with this derivation and the resulting equation of the three-dimensional power distribution is that it is only representing light being absorbed within a homogeneous thin powder layer, but doesn't feature any differentiation for consolidated melt or solidified material in its original form. Yet, the power of Eq. (4.3) is that it is accurate for opaque, and thus solid surfaces, resulting in an absorptivity equal to $1 - r$ [33].

Therefore, it is proposed to subdivide the powder bed in stacks of elements with the same xy-coordinates and to evaluate the powder bed properties h_{pl} and ρ_{pl} for every single element stack in every time step based on its current configuration as illustrated in Fig. 4.3.

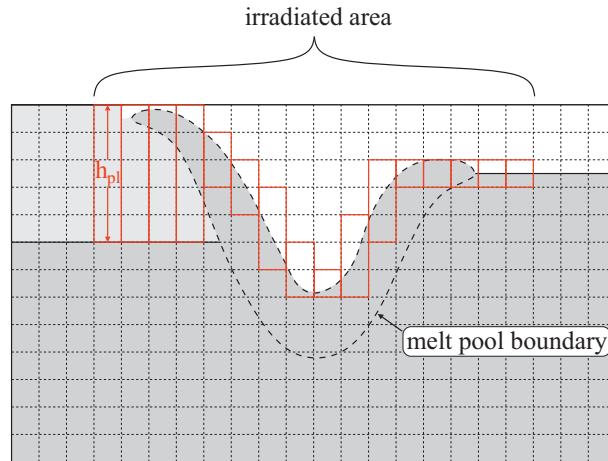


Figure 4.3: Illustration of the dynamic evaluation of the powder layer height for the adjusted absorption model in a cross section of the melt pool front which is shaping a keyhole-like dent. Light gray indicates powder, dark gray bulk or melt and white gaseous phase

The powder layer height of an element stack is considered to be the difference of the uppermost not empty, not completely filled element and the uppermost completely filled element. The powder layer density is calculated as the average filling degree of elements that are considered to be part of the current element stack's powder layer. To account for the possibly strongly varying filling degrees within the element stack, the absorbing length of an element is weighted by the ratio of its filling degree to the element stack's average powder layer density. This is necessary to keep elements with a very low filling degree from artificial overheating. Although these changes are not perfectly accurate from the analytical point of view, it is possible to increase the spatial resolution of the Gusarov absorption model significantly by taking these changes into account for the numerical model.

Furthermore, not only absorption in powder and on solid material can be differentiated but also steep flanks and more or less even melt pool surface areas because a flank angle of $\geq 45^\circ$ results in more than one not completely filled element in an element stack and thus induces multiple reflection to the keyhole-like dents as well.

4.2.2 Conduction, Convection and Radiation

Additionally to the absorption model, thermal conduction, convection and radiation are considered to calculate the temperature field. Since the time step size is very small due to the needs of the melt flow simulation, an explicit finite difference scheme is used to solve the three-dimensional inhomogeneous heat conduction equation. Therefore, the conductive heat flow in x-direction $\dot{Q}_{cond,x,i,j,k}$ is exemplarily discretized, and due to the cubic elements simplified to

$$\begin{aligned} \dot{Q}_{cond,x,i,j,k} = & 2 \cdot \Delta x \cdot \frac{\lambda_{i,j,k} \cdot \lambda_{i+1,j,k}}{\lambda_{i,j,k} + \lambda_{i+1,j,k}} \cdot (T_{i+1,j,k} - T_{i,j,k}) \\ & + 2 \cdot \Delta x \cdot \frac{\lambda_{i,j,k} \cdot \lambda_{i-1,j,k}}{\lambda_{i,j,k} + \lambda_{i-1,j,k}} \cdot (T_{i-1,j,k} - T_{i,j,k}) \end{aligned} \quad (4.10)$$

as described by [76]. Here $\lambda_{i,j,k}$ is the temperature dependent thermal conductivity of element (i, j, k) . As Eq. (4.10) shows, the thermal conductivity over the boundary of two neighboring elements is not averaged but evaluated on the basis of a series of thermal resistances. This allows a more accurate representation of the heat conduction over phase boundaries, like from melt to powder or melt to atmosphere.

Heat flows due to radiation

$$\dot{Q}_{rad} = \epsilon \cdot \sigma_B \cdot A \cdot T^4 \quad (4.11)$$

and convection

$$\dot{Q}_{conv} = \alpha_{conv} \cdot A \cdot \Delta T \quad (4.12)$$

are implemented as well. In those ϵ is the material's emissivity, σ_B the Stefan Boltzmann constant, α_{conv} the heat transfer coefficient and A the surface.

4.2.3 Melting, Solidification and Evaporation

The heat of fusion is considered as a separate heat sink during melting and heat source during solidification, instead of being represented by an increase of the specific heat capacity in the range between solidus and liquidus temperature. The separate handling is beneficial for the implementation within the explicit scheme. Therefore, as soon as solidus

temperature is reached the surplus of energy is consumed by the heat of fusion. Thereby, the amount of equivalent energy E_{eq} accumulates step by step until the necessary energy for melting E_{fusion} is overcome. As soon as the necessary amount is achieved the temperature increase takes place as usual. In between the actual temperature T^n is set to be the interpolation between solidus and liquidus temperature on the basis of the ratio of accumulated and necessary energy. When the material solidifies the same process is reversed, starting at liquidus temperature. The procedure is illustrated in Fig. 4.4 and the necessary equations are given for the case of melting as

$$\Delta T^n = T_{pred}^n - T^{n-1} \quad (4.13)$$

$$E_{eq}^n = E_{eq}^{n-1} + \Delta T^n \cdot \rho \cdot c_p \cdot F \cdot V \quad (4.14)$$

$$T^n = T_{solidus} + \frac{E_{eq}^n}{E_{fusion}} \cdot (T_{liquidus} - T_{solidus}). \quad (4.15)$$

By taking T^{n-1} to calculate the surplus of energy explicitly a small error is accepted.

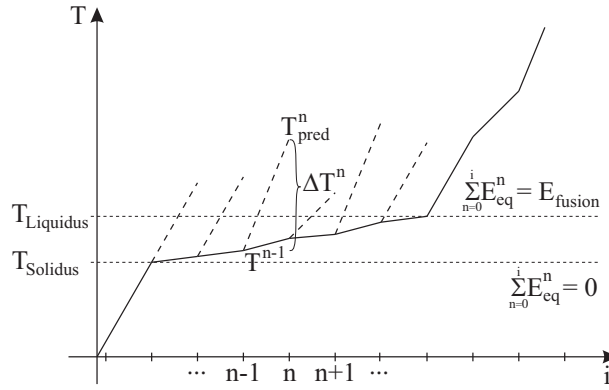


Figure 4.4: Illustration of the explicit procedure with which heat of fusion is handled within the presented model. The temperature difference is used to calculate the equivalent energy according to Eq. (4.14).

Evaporation needs to be handled differently because it is dependent on the surrounding pressure according to the saturated vapor pressure curve described by the Clausius-Clapeyron equation. Since evaporation leads to a recoil pressure which increases the value of the surrounding pressure, first the recoil pressure has to be approximated. Various approaches are known to do so, either more detailed ones that include a modeling of the Knudsen layer [48, 50], or experimentally supported ones [47, 57]. Still, the approaches lead to a similar result:

$$p_{rec}^n = 0.54 \cdot p_0 \cdot e^{\frac{L_{evap} \cdot M_{mol}}{R} \cdot \left(\frac{1}{T_0} - \frac{1}{T_{pred}^n} \right)} \quad (4.16)$$

In that the Clausius-Clapeyron equation is weighted by a factor of 0.54 to account for the backwards directed flux of evaporated material which is resulting in a recoil pressure on the surface [47, 50, 57]. Within the Clausius-Clapeyron equation p_0 and T_0 are the known pressure and temperature at which evaporation occurs while p_{rec} is the approximated recoil pressure at the predicted temperature. L_{evap} is the heat of evaporation, M_{mol} the molar mass and R the universal gas constant.

The recoil pressure is used to map the predicted temperature back to the saturated vapor pressure curve to get the actual temperature of the time step T^n .

$$T^n = \left(\frac{1}{T_0} - \frac{\ln\left(\frac{p_{rec}^n}{p_0}\right) \cdot R}{L_{evap} \cdot M_{mol}} \right)^{-1} \quad (4.17)$$

The temperature difference is used to calculate the amount of evaporated material that is necessary to guarantee the conservation of energy. The volume change ΔV^n

$$\Delta V^n = \frac{(T^n - T_{pred}^n) \cdot c_p \cdot F \cdot V}{L_{evap}} \quad (4.18)$$

can then be used to adjust the element's filling degree.

4.3 Modeling Fluid Flow

Calculating the fluid flow field is a bit more complicated than calculating the heat flow. To do so, the continuity, Eq. (4.19), and momentum equation, Eq. (4.20), (also known as Navier-Stokes equation) have to be solved implicitly.

$$\nabla \cdot \mathbf{u} = 0 \quad (4.19)$$

$$\rho \left(\frac{\partial \mathbf{u}}{\partial t} + \mathbf{u} \cdot \nabla \mathbf{u} \right) = -\nabla p + \nabla \cdot \eta \nabla \mathbf{u} + \frac{\mathbf{b}}{V} \quad (4.20)$$

In these equations \mathbf{u} is the velocity vector, p the pressure, η the dynamic viscosity and \mathbf{b} the vector of body forces. To calculate the body forces, first the melt pool surface has to be reconstructed. The resulting fluid flow field can then be used to calculate the material and heat exchange within the melt pool.

4.3.1 Surface Reconstruction

The reconstruction and tracking of the surface is handled by using a combined level set volume of fluid method (CLSVOF) as presented by Son et al. [94, 92, 93]. It's needed to position the surface forces at the correct locations and under the correct incident angle as well as for the smoothing of material properties across the surface to improve the converging behavior of the fluid flow solver. The CLSVOF method contains four major steps in regards to handling the surface. First, identifying the surface elements. Second, reconstructing the surface. Third, initializing the level set function. Fourth, using the level set function to smooth the material properties. Some changes within different criteria are necessary to account for the material configuration within the powder bed. Those are explained at appropriate parts of the following, detailed explanation of the CLSVOF approach.

As explained, surface elements have to be identified first. To do so, the volume of fluid function F is used which is equal to the previously mentioned filling degree. In its basic form any element with a volume of fluid function smaller than one, meaning any not completely filled element, is considered a surface element. This is a viable approach for common problems like bubbles within a liquid [94] because it offers a high resolution. The problem within the SLM model is that any element within the powder bed is not completely filled in its initial configuration which is why an alternative approach is necessary. Therefore, in the SLM model any non-empty element that has at least one empty element next to it is considered a surface element. This allows to handle the consolidation of material from powder to melt pool without any problems but coarsens the resolution of detectable porosity and bubbles to sizes of at least a single completely empty element.

The next step is to reconstruct the surface. This means that the material configuration that results in a continuous surface has to be found. Therefore, the normals of the previous time step as well as the volume of fluid function are used. Using these two variables the configuration within the melt pool can be calculated based on some standard cases as depicted in Fig. 4.5 in a linear-piece-wise manner as discussed in [93]. The information about the shortest distance of the surface to the element's corner and about the intersection of the material with the element boundaries is necessary for the following step.

In the third step the level set function φ is (re-)initialized. The level set function is defined as the shortest distance to the surface and is negative for the gaseous phase, positive for the liquid phase and zero for the surface itself. Hence, the shortest distance of any element to the surface is calculated. These distances are used to recalculate the normals \mathbf{n}

$$\mathbf{n} = \frac{\nabla\varphi}{|\nabla\varphi|} \quad (4.21)$$

and the surface curvature κ

$$\kappa = \nabla \cdot \mathbf{n}, \quad (4.22)$$

which are then discretized using a central differencing scheme as explained by [93].

The level set function is also used to smooth the material properties across the melt pool surface. For that a smoothing function H is used which is commonly zero in the gaseous phase and one in the liquid phase, but can be calculated near the surface according to

$$H = 0.5 + \frac{\varphi}{3\Delta x} + \frac{\sin(2\pi\varphi)/(3\Delta x)}{2\pi} \quad \text{if } |\varphi| < 1.25\Delta x \quad (4.23)$$

as proposed by [92], using the level set function as well as the element size Δx . The smoothing function can then be used to smooth density ρ and viscosity η , defining the change of values across the surface as

$$\rho = \rho_g + (\rho_l - \rho_g) \cdot H \quad (4.24)$$

$$\eta = \eta_g + (\eta_l - \eta_g) \cdot H \quad (4.25)$$

to improve the converging behavior of the fluid flow solver.

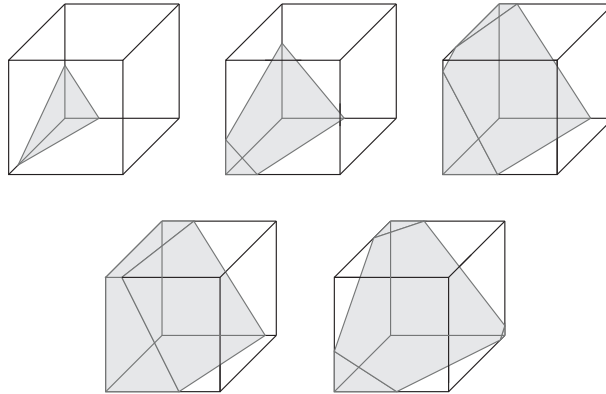


Figure 4.5: Depiction of the five standard configurations that can be used to characterize the material within a surface element (see [92]). Any material configuration within an element can be rotated to be comparable to one of the five shown standard configurations.

4.3.2 Driving Forces

The driving forces of the fluid flow are the body force due to the buoyancy effect \mathbf{b}_{buo} as well as the surface forces due to capillary effects \mathbf{b}_{cap} , the Marangoni effect \mathbf{b}_{mar} and recoil pressure \mathbf{b}_{rec} . The surface forces are dependent on the surface normal which is reinitialized by the CLSVOF method. To restrict the forces to the surface a $\delta(\varphi)$ -function is included

which is one for surface elements and zero for all other. Hence, the following equations can be used to calculate the driving forces that are considered within the momentum equation.

$$\mathbf{b}_{buo} = \mathbf{g} \cdot \rho \cdot V \quad (4.26)$$

$$\mathbf{b}_{cap} = -\mathbf{n} \cdot \sigma \cdot \kappa \cdot A \cdot \delta(\varphi) \quad (4.27)$$

$$\mathbf{b}_{mar} = [(\mathbf{I} - \mathbf{n} \otimes \mathbf{n}) \cdot \nabla] \cdot \sigma \cdot A \cdot \delta(\varphi) \quad (4.28)$$

$$\mathbf{b}_{rec} = \mathbf{n} \cdot p_{rec} \cdot A \cdot \delta(\varphi) \quad (4.29)$$

In these \mathbf{g} is the vector of gravitational acceleration, σ the surface tension and \mathbf{I} the three-dimensional identity matrix.

4.3.3 Fluid Flow Solver

To solve the momentum equation of fluid flow (the Navier-Stokes equation) a pressure implicit splitting of operators scheme is used as proposed by Issa [39], which is discretized using the methods of general transportation phenomena as shown by Versteeg and Malalasekera [102]. The PISO scheme splits the calculation of the velocity and pressure field up in multiple steps as follows.

1. The velocity field \mathbf{u}^* is calculated based on the driving forces and a guessed pressure field \mathbf{p}^* which is commonly taken as the pressure field of the previous time step \mathbf{p}^{n-1} . (Eq. (4.30))
2. The necessary correction of the pressure field \mathbf{p}' is then calculated based on the new velocity field. (Eq. (4.31))
3. The pressure field correction is used to get a corrected pressure field \mathbf{p}^{**} as well as a corrected velocity field \mathbf{u}^{**} . (Eqs. (4.32) and (4.33))
4. The correction is repeated once, calculating a second correction \mathbf{p}'' on basis of the corrected velocity field. (Eq. (4.34))
5. The final pressure \mathbf{p}^{***} and velocity field \mathbf{u}^{***} are calculated based on the second corrective term. (Eq. (4.35) and (4.36))

The equations for a discretization in x-direction are given below as shown by [102].

$$a_{i,j,k}^u u_{i,j,k}^* = \sum_{nb} a_{nb}^u u_{nb}^* + (p_{i-1,j,k}^* - p_{i,j,k}^*) \cdot A_{i,j,k} + b_{i,j,k} \quad (4.30)$$

$$a_{i,j,k}^{p^*} p'_{i,j,k} = \sum_{nb} a_{nb}^{p^*} p'_{nb} + c'_{i,j,k} \quad (4.31)$$

$$p_{i,j,k}^{**} = p_{i,j,k}^* + p'_{i,j,k} \quad (4.32)$$

$$u_{i,j,k}^{**} = u_{i,j,k}^* + \frac{A_{i,j,k}}{a_{i,j,k}^{u^*}} (p'_{i-1,j,k} - p'_{i,j,k}) \quad (4.33)$$

$$a_{i,j,k}^{p^{**}} p''_{i,j,k} = \sum_{nb} a_{nb}^{p^{**}} p''_{nb} + c''_{i,j,k} \quad (4.34)$$

$$p_{i,j,k}^{***} = p_{i,j,k}^{**} + p''_{i,j,k} \quad (4.35)$$

$$u_{i,j,k}^{***} = u_{i,j,k}^{**} + \frac{A_{i,j,k}}{a_{i,j,k}^{u^{**}}} (p''_{i-1,j,k} - p''_{i,j,k}) \quad (4.36)$$

Eqs. (4.30), (4.31) and (4.34) consist of implicit linear equation systems because of the dependency on the neighboring values of pressure p_{nb} and velocity u_{nb} and are thus solved using the Matlab internal bi-conjugate gradients stabilized method, while the other equations can be solved explicitly. a^u , a^p and c as well as the asterisk or apostrophe versions are the coefficients of the linear equation systems that are originating from the Navier-Stokes equation and are considering the influences of viscosity, density and inertia. Additionally, b is taking the driving forces into account. The detailed information of how these coefficients are calculated is listed by Versteeg and Malalasekera [102] (pp. 124, 125, 145, 152).

The finally corrected values are checked for convergence, since the PISO scheme is implicit in its nature. Yet, due to the double correction scheme the PISO solver commonly tends to converge within one iteration for sufficiently small time steps [39].

4.3.4 Volume and Heat Exchange

Volume and heat exchange due to melt pool flow are evaluated based on the previous calculation of the fluid flow field and the current material configuration. Therefore, the CLSVOF method is elaborated once more, so that

$$\frac{\partial F}{\partial t} + \nabla \cdot \mathbf{u}F = F \nabla \cdot \mathbf{u} \quad (4.37)$$

can be used to calculate the volume exchange as explained by [94]. It is discretized in all three directions to solve it in a step-wise manner as shown in Eqs. (4.38) to (4.40) as proposed by [92].

$$\frac{F^* - F^{n-1}}{\partial t} + \frac{\Delta u F^{n-1}}{\partial x} = F^* \frac{\partial u}{\partial x} \quad (4.38)$$

$$\frac{F^{**} - F^*}{\partial t} + \frac{\Delta v F^*}{\partial y} = F^* \frac{\partial v}{\partial y} \quad (4.39)$$

$$\frac{F^n - F^{**}}{\partial t} + \frac{\Delta w F^{**}}{\partial z} = F^* \frac{\partial w}{\partial z} \quad (4.40)$$

The equations are again discretized on the staggered grid as exemplary shown in Eq. (4.41) for the x-direction [92].

$$F_{i,j,k}^* = F_{i,j,k}^n dx_i dy_j dz_k + (u dt F^n dy dz)_{i-1/2,j,k} - (u dt F^n dy dz)_{i+1/2,j,k} - F_{i,j,k}^* [(u dt dy dz)_{i-1/2,j,k} - (u dt dy dz)_{i+1/2,j,k}] \quad (4.41)$$

Since $(u dt F^n dy dz)_{i-1/2,j,k}$ equals the volume dV_F which is advected across the face $(i - 1/2, j, k)$, the equation is solved geometrically using the current material configuration. To increase the accuracy of this evaluation the surface is reconstructed after each step. Additionally, to reduce the influence of the sequence, with every time step the sequence is rotated, meaning in the first time step the sequence is x, y, z and in the second time step y, z, x and so on. The heat flow can then simply be calculated by using the heat balance of inherent heat and outgoing as well as incoming heat within every single element.

4.4 Validation

As earlier discussed, a qualitative as well as quantitative validation of the numerical model is necessary to make sure that it's accurate enough to be used for the numerical investigation of the SLM process. Hence, the following subsections start with the qualitative validation of the absorption characteristics and melt pool dynamics based on the references discussed in chapter 2, before a quantitative, experimental validation of the melt pool dimensions is given.

The experimental validation is done using cubic samples of the stainless steel 316L. The cubes are built on a ConceptLaser M2 that utilizes a continuous wave 200 W fiber laser with a center wavelength of 1070 nm. A layer thickness of 30 μm and an unidirectional irradiation is used which is alternated by 90° every layer. The samples are prepared as discussed in subsection 5.3.3. All melt pools of the uppermost layer are measured as shown in Fig. 4.6 to cover the range of values for depth, width and area of the melt pool cross sections.

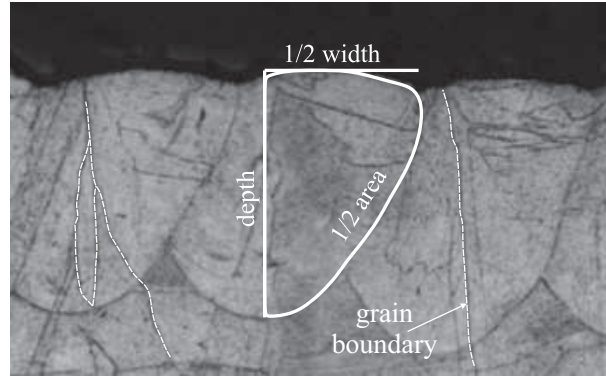


Figure 4.6: Illustration of the defined depth, width and cross section area measures used for validation. The depth is measured from the top to the deepest point of the melt pool. The width is measured from the estimated center of the melt pool to the outer visible side (see [34]). Some grain boundaries are indicated by white dashed lines.

The initial configuration as discussed in subsection 4.1.1 is used to simulate the data which is compared to the experimental data. The data is extracted from the simulation equivalent to the experimental data, meaning that just the measures on the side of the already solidified line are considered.

4.4.1 Material Data

The temperature-dependent material properties that are used to simulate the processing of stainless steel 316L are listed in Tab. 4.1. Just the distinct values at room, solidus, liquidus and evaporation temperature are shown. More data points are listed in the reference [37]. In between these data points the material properties are interpolated.

Table 4.1: Overview of material data that is used in the numerical model [37, 73]. Solidus temperature is at 1405°C , liquidus at 1445°C and evaporation temperature at 2817°C .

material property	25°C	1405°C	1445°C	2817°C	constant
specific heat [$J/kg\text{K}$]	450	700	707	900	
thermal conductivity [$W/m\text{K}$]	13.3	33.8	18.1	22.2	
surface tension [N/m]			1.76	0.41	
dynamic viscosity [$Pa\text{ s}$]			0.0059	0.0014	
heat of fusion [kJ/kg]					270
heat of evaporation [kJ/kg]					7450
hemispherical reflectance					0.64

4.4.2 Absorption Characteristics

The importance of absorption and its modeling is discussed in detail in the previous sections. Therefore, the absorption model is checked for reasonable behavior first, meaning a plausible distribution and amount of absorbed power. To evaluate the spatial distribution, the elements are split into five different categories. The categorization takes place on basis of the elements' temperature, filling degree and material configuration. An element is considered to be powder if its temperature is below the liquidus temperature, if it's not filled completely and if its position is on the powder side of the initial configuration. In case the element is below liquidus, partly filled and not on the powder side it is considered the previous track. If the element is completely filled and still below liquidus temperature it's either previous track or previous layer which is differentiated based on the position in the mesh. Elements with a temperature higher than liquidus are either consolidated melt, meaning the melt pool, or non-consolidated melt, representing powder particles that are melting but are not part of the melt pool yet. Analogue to the determination of the powder layer height in the framework of the absorption modeling, a molten element is being considered consolidated if a completely filled, molten element is underneath. In other cases it is considered non-consolidated melt.

Taking these categories into account, the model offers the chance to get information about how much power is available to the different regions, how much power is absorbed by those and thus how high the different effective absorptivities of these categories are. Fig. 4.7 shows the development of the available power within the regions.

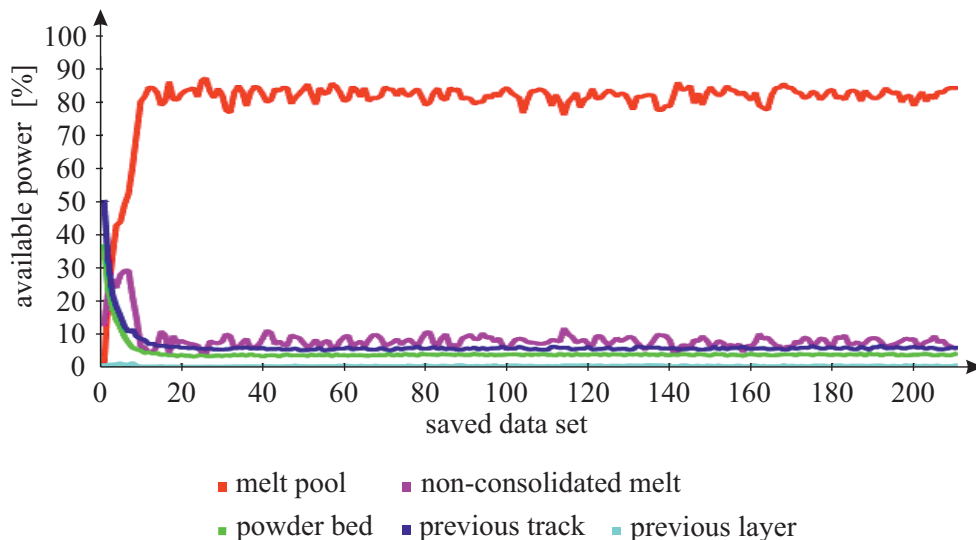


Figure 4.7: Evolution of available power in the listed areas within the process. The shown values are based on a $90\ \mu\text{m}$ focal spot that is moving on the edge of a previous track with $850\ \text{mm/s}$ and $200\ \text{W}$

The figure shows that the available power is equally divided onto power bed and previous track in the beginning, since the laser path is simulated to be moving exactly on the edge. As soon as the irradiation starts the available power on previous track and in the powder decrease. Additionally to this, a distinct peak within the non-consolidated melt in the very beginning of the process can be observed. This peak has to be accounted to the intermediate state of slightly molten powder particles that are not yet consolidated to a melt pool briefly after the irradiation starts. After that short period of time the non-consolidated melt is restricted to the front of the melt pool and thus its amount of absorbed power is dropping to a quasi-constant value. As the material starts melting the available power to be absorbed in the melt pool is continuously increasing until a quasi-steady state is reached. The power which is available for the previous layer is very low at all times because it is covered by powder material. As soon as the melt pool develops it decreases even further to a quasi-constant low value. Throughout the process the available power on the previous track is slightly higher than the one available in the powder which is due to the fact that the melt pool on the side of the previous track is slightly smaller due to a worse absorptivity on the solid material as well as due to a better heat conduction.

In contrast, when having a look into the actually absorbed power within the different regions as depicted in Fig. 4.8, it can be seen that the power absorbed on the previous track is lower than in the powder bed. This can be traced back to the difference in absorptivities. Furthermore, it is shown that the total absorptivity of all regions is more or less constant during all phases of melt pool evolution, although the distribution of absorbed power changes rapidly in the beginning.

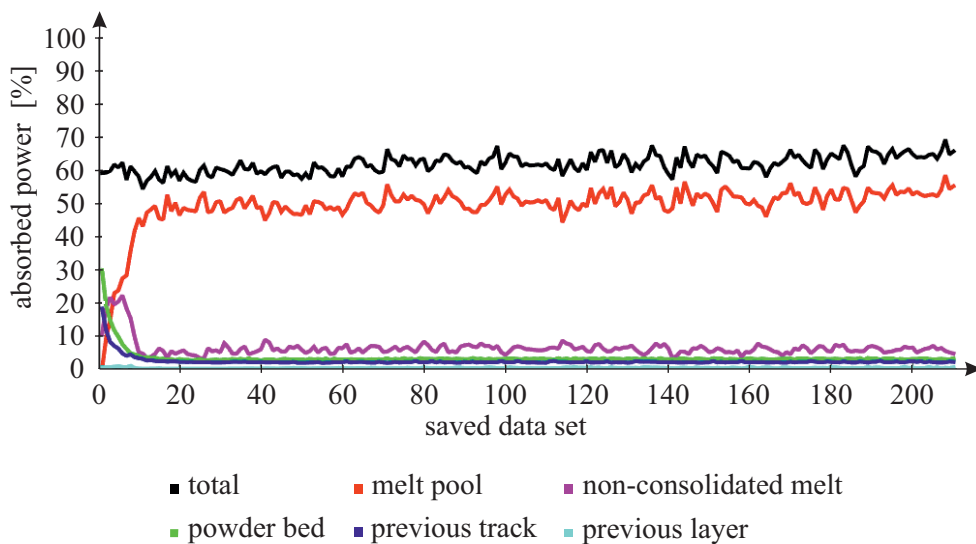


Figure 4.8: Evolution of the absorbed power in and around the melt pool. The shown values are based on a $90\ \mu\text{m}$ focal spot that is moving on the edge of a previous track with $850\ \text{mm/s}$ and $200\ \text{W}$

These observations are present for all investigated scan speeds, although the absolute value of absorbed powers change. This is due to the fact that with increasing scan speed the overlap of the beam with the not yet molten material increases, which can be deduced from the distribution of available power in the different regions, as shown in Fig. 4.9. While the amount of power available in the powder and on the previous track increases, the available power for the melt pool decreases.

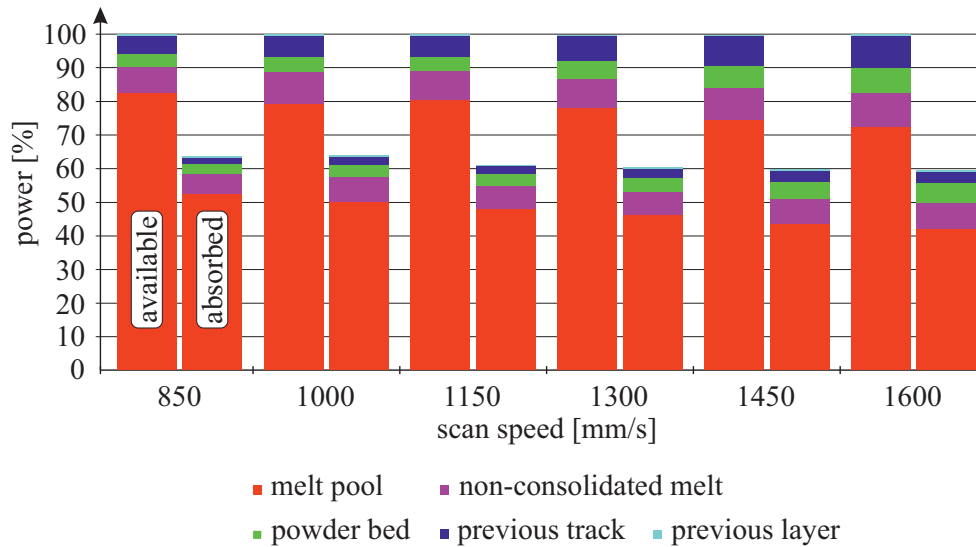


Figure 4.9: Available and absorbed powers for all investigated scan speeds differentiated for the discussed regions in and around the melt pool. Values are averaged over the last 50 saved data sets so that a quasi-steady state can be assumed.

The figure as well shows, the absorbed amount of power which is approximately constant at about 64 % for scan speeds of 850 mm/s and 1000 mm/s and then drops to roughly 60 % for faster scan speeds. Within the constant regions the reducing absorbed power in the melt pool is equalized by an increase of absorbed power in the powder bed and on the previous track. To investigate the reason for the drop of absorptivity between 1000 mm/s and 1150 mm/s the effective absorptivities of the different categories can be evaluated for different scan speeds. The values are listed in Tab. 4.2.

It can be seen that the absorptivities of the powder bed, the previous track and layer are about constant for all scan speeds, which is plausible. In contrast, the effective absorptivity of the melt pool drops by about 4 % in between the two scan speeds between which the drop of overall absorptivity can be observed. Therefore, the drop in the overall value can be accounted for by the drop of the melt pool's value. The drop in effective absorptivity can be estimated to be a consequence of the welding mode, from a more deep penetration welding mode to a more conduction welding mode. Yet, more effects need to be checked to be certain of that. While the melt pool's absorptivity drops by a few percent, the value of

Table 4.2: Effective absorptivities of the different categories at different scan speeds.

scan speed [mm/s]	850	1000	1150	1300	1450	1600
melt pool	0.64	0.64	0.60	0.60	0.59	0.59
non-consolidated melt	0.79	0.78	0.80	0.81	0.80	0.80
powder bed	0.82	0.82	0.82	0.82	0.82	0.82
previous track	0.37	0.37	0.37	0.37	0.37	0.37
previous layer	0.81	0.81	0.82	0.82	0.82	0.81
overall	0.64	0.64	0.61	0.60	0.60	0.60

the non-consolidated melt is increasing. Yet, no significant influence on the overall value can be observed because of the small part of non-consolidated melt which is present in the front of the melt pool. This can as well be seen by having a look at the available powers. The more or less linear drop of absorbed power within the melt pool is compensated by the additional power which is absorbed in powder and on the previous track, since the average absorptivities of both sides roughly equal the average value of the melt pool. The absorptivity of the previous layer is comparably high which is due to the fact that its subject to multiple reflection because of the powder which is on top of it.

Comparing the simulative results of overall absorptivity with the measured values of Trapp et al. [101] a fairly good agreement can be seen. The overall absorptivity is about 60 % to 64 % and the overall absorptivity on the powder bed side, which is more comparable to the experiments of Trapp et al., between 67 % and 70 %. Trapp et al. measured values between 60 % and 70 % for the same material. Together with the plausible temporal and spatial distributions it can be concluded that the implemented absorption model is offering an effective and accurate way to represent the interaction between the incoming laser power and the different kind of material states that are absorbing it.

4.4.3 Melt Pool Dynamics

Further on, it needs to be checked whether the overall melt pool behavior is plausible, meaning if the evolution of the melt pool is comparable to what is known from literature, and if the melt pool velocities are reasonable. Therefore, Fig. 4.10 shows simulated cross sections at different evolutionary steps for two scan speeds. The cross section of the scan speed of 850 mm/s represents a parameter which is defined by severe evaporation, while at 1600 mm/s the energy density is far lower which can as well be seen by comparing the resulting melt pool dimensions.

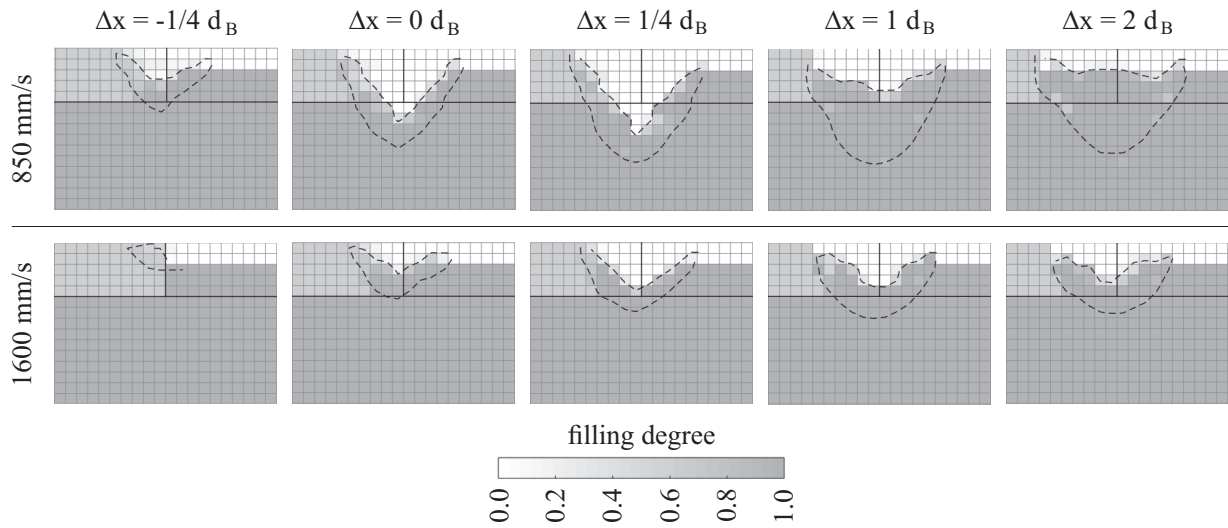


Figure 4.10: Simulated evolution of melt pool geometry and surface distortion due to recoil pressure for scan speeds of 850 mm/s and 1600 mm/s . The dashed lines indicate the melt pool cross sections' outer contours. The laser beam is moving from the back towards the reader. Δx is the distance between the laser beam's center point and the shown cross section. d_B is equivalent to a beam diameter of $90\text{ }\mu\text{m}$. The mesh size is $10\text{ }\mu\text{m}$.

First, the powder bed starts melting and consolidates to a melt pool. Briefly after the laser beam reaches the cross section a distinct cavity forms in case of 850 mm/s . The melt is being pushed away by the recoil pressure that is induced to the melt pool surface by rapid evaporation. The maximum extent of the cavity is reached when the beam center already moved on by about a quarter beam diameter. At this point the cavity even reaches into the previous layer. After that, the cavity fills up again and the melt pool widens in the upper regions. In contrast, at 1600 mm/s no distinct cavity can be observed. Only a small dent within a shallow melt pool evolves. Due to that and the significantly lower energy density the melt pool dimensions remain smaller.

Fig. 4.11 shows the same cross sections for 850 mm/s extended by information on the fluid flow directions and relative magnitude. The fluid flow fields show that recoil pressure is pushing the melt sideways and downwards to form the distinct cavity. Due to the induced downwards flow the melt pool reaches greater depth more easily, since the hot melt of the melt pool surface is pushed into the direction of still solidified material as well due to the fact that only a thin film of melt remains between melt pool surface and solidified material. Thereby the heat input into the solidified material is increased. As the cavity in this cross section closes, an upwards melt flow can be observed, which is a result of the melt that is escaping the cavity when being pushed downwards. As soon as the melt pool is not dominated by the cavity anymore, a Marangoni convection dominated melt flow is established. This is defined by sideways melt flow at the melt pool surface. This melt

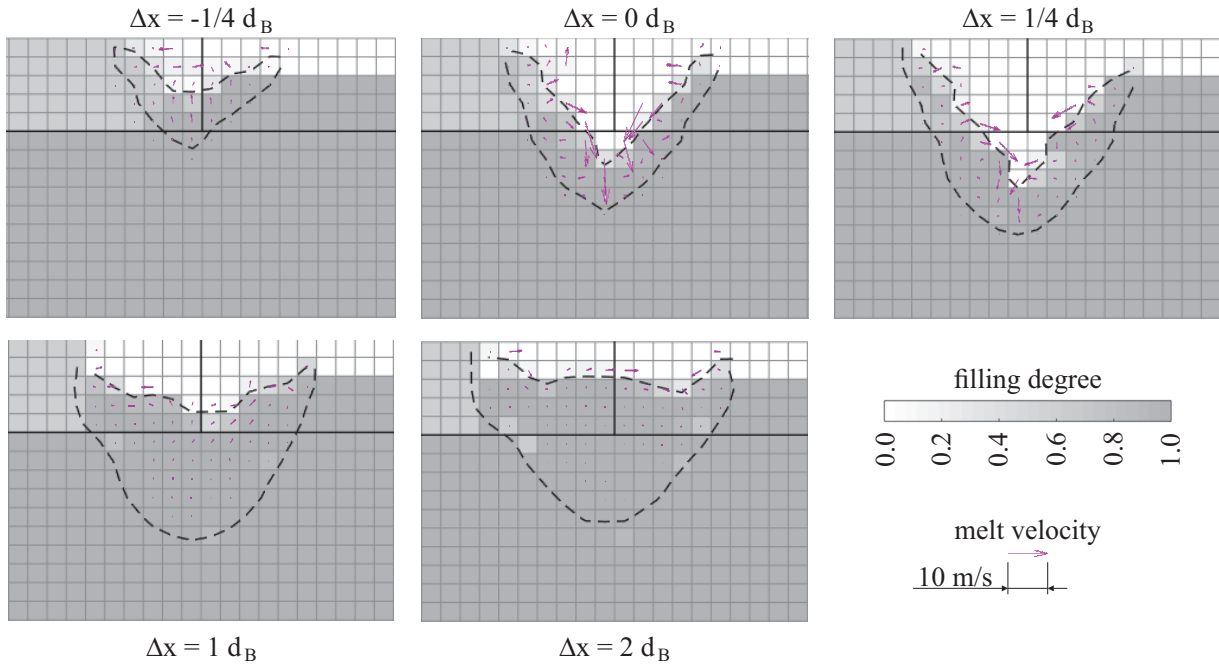


Figure 4.11: Melt pool evolution and melt velocities in cross sections at a scan speed of 850 mm/s . The dashed lines indicate the melt pool cross sections' outer contours. The laser beam is moving from the back towards the reader. Δx is the distance between the laser beam's center point and the shown cross section. d_B is equivalent to a beam diameter of $90 \mu\text{m}$. The mesh size is $10 \mu\text{m}$.

flow transports hot melt to the melt pool boundaries and is thereby increasing the melt pool size in the upper part of the melt pool. This behavior is in perfect accordance with the discussed findings of Khairallah et al. [47] who discussed this behavior on the basis of a more detailed powder bed.

The evolution of maximum absolute fluid flow velocities within the cross section are shown in Fig. 4.12. It shows velocities of about maximum 6 m/s to 14 m/s for the time when the cavity is visible in the cross section, about 4 m/s to 5 m/s when the cavity is closing and 2 m/s to 4 m/s for the Marangoni convection driven melt pool tail. These values show good accordance with the values given by Gu and Yuan [30].

The results show a plausible melt pool behavior as well as reasonable fluid flow velocities. Therefore, it can be concluded that a good representation of the melt pool dynamics by the presented model can be assumed.

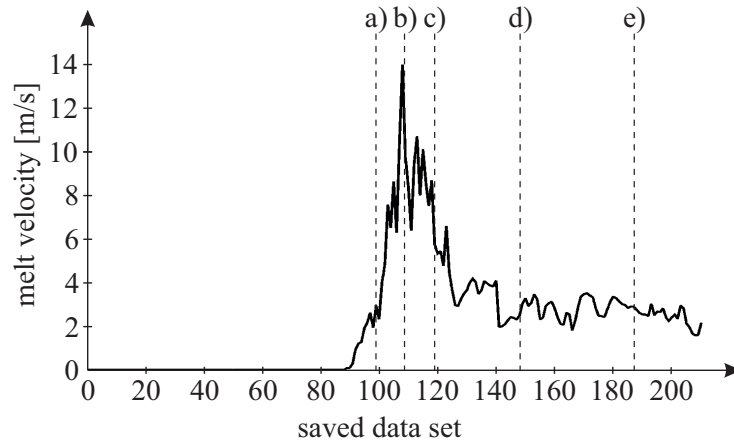


Figure 4.12: Maximum melt velocities within the previously shown cross section at the beam positions of a) $\Delta x = -1/4 d_B$, b) $\Delta x = 0 d_B$, c) $\Delta x = 1/4 d_B$, d) $\Delta x = 1 d_B$ and e) $\Delta x = 2 d_B$ with d_B being equal to a beam diameter of $90 \mu m$, the scan speed is 850 mm/s and the laser power 200 W .

4.4.4 Evaporation

The numerical model offers the possibility to easily check the occurring recoil pressure and amount of evaporated material. Tab. 4.3 lists these values for the investigated scan speeds.

The values show that there are two different zones regarding the recoil pressure. In the first zone for speeds of 850 mm/s and 1000 mm/s the recoil pressure is in between 9.5 bar and 10 bar . In contrast, it drops to a roughly constant value of about 8 bar for faster scan speeds. This drop is supporting the assumption that the welding mode changes between 1000 mm/s and 1150 mm/s , as already discussed on the basis of absorptivity in subsection 4.4.2.

Table 4.3: Simulated values for recoil pressure and mass of evaporated material for different scan speeds. Values are the median of the last 50 data sets so that a quasi-steady state can be assumed.

scan speed [mm/s]	850	1000	1150	1300	1450	1600
recoil pressure [bar]	9.81	9.53	8.01	8.33	7.84	8.17
evaporated material [$\mu\text{g/mm}$]	3.44	3.19	2.76	2.48	2.20	1.96

The same can be observed when having a look at the amount of evaporated material, although it is not that obvious. Still, a larger drop in evaporated material can be observed between 1000 mm/s and 1150 mm/s as well. Starting from a value of about $3.45 \mu\text{g/mm}$ the amount of evaporated material constantly drops by roughly $0.25 \mu\text{g/mm}$ with every 150 mm/s faster scanning. Only in between the two mentioned speeds the difference is about $0.40 \mu\text{g/mm}$.

4.4.5 Melt Pool Dimensions

As already mentioned before, most known simulation tools lack a quantitative validation. Therefore, a set of experiments is done to quantify the error of the simulation tool by comparing the simulated cross section depth, width and area with the experimentally achieved values of the upper layer of a cubic sample as described in section 4.4.

Fig. 4.13 shows the comparison of measured mean values and the simulated values. The graphs show an overall good accordance of experimental and simulated values. The error of every single depth and width value is smaller than 20 %, most even smaller than 10 %. Especially the depth values are in good accordance. The simulated values are all within the standard deviation of the experiments for every investigated scan speed, with the simulated ones always being slightly lower than the experimental values. In contrast, the simulated width is continuously higher than the experimental one, but still within the standard deviation for all except one scan speed.

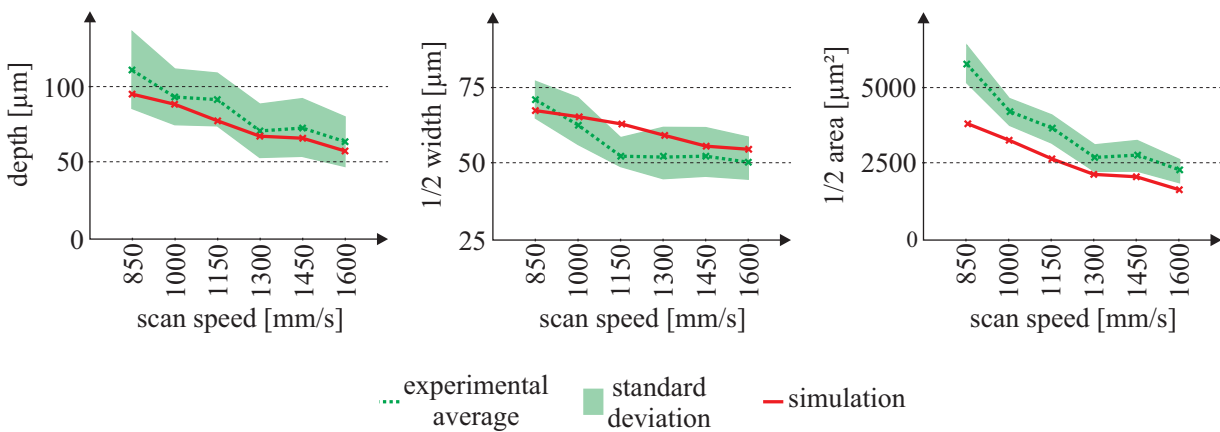


Figure 4.13: Results of simulated and measured melt pool dimensions of cubic samples of stainless steel 316L for different scan speeds at 200 W laser power.

The most noticeable error occurs for the cross section area, with the highest error being about 35 %. The absolute error is continuously decreasing for faster scan speeds. It can be assumed that the difference in the cross section area can be attributed to the residual heat that accumulates in the process from track to track. This heat accumulation is not accounted for in the numerical model, since only one track is simulated, starting at room temperature. With increasing scan speeds the heat up is expected to be lower, which fits to the observed decreasing absolute error with increasing scan speeds.

Still, the overall error of all measures is just 15.2 % (about 10 % in depth, 9 % in width and 27 % in area), which is worth mentioning, since no tuning factor is used to fit the simulated values to the experimental ones. This shows that the numerical model is not

just giving plausible melt pool behavior but also quantitatively reasonable results, although the powder bed is represented in a homogeneous way in the model's initial condition and a quite coarse mesh is used. Especially the elaborated absorption and evaporation models seem to be a good simplification of what is happening within the process. Thus, both are laying the basis for good simulation results due to their dominating influence on the process dynamics. Therefore, the numerical model can be used as a tool to learn more about the effects of known as well as new scan strategies on the melt pool.

Chapter 5

Setup, Tools and Methods

The following sections of this chapter describe and explain the setup of the laboratory machine as well as its initial start-up and the additional setup for high speed imaging, the software tools, that are used additionally to the simulation, to generate the necessary G-code or automatically evaluate the high speed imaging as well as the methods that are used to calibrate the laboratory machine so that two-beam strategies can be used as well as the ones which are used to analyze the experiments' data.

5.1 Experimental Setup

5.1.1 Laboratory Machine

The laboratory machine that is used for the two-beam experiments is self-build from scratch to guarantee the necessary functionality and freedom regarding process changes. The key feature is the combination of two independent laser sources and scan heads which are put together in a way that a large scan field overlap is achieved, so that both laser spots can be moved and turned on or off independently as well as in a synchronized manner. Therefore, two water-cooled IPG YLR-200 continuous wave fiber lasers with a center wavelength of 1070 nm and 200 W laser power each are used. Those offer high stability and a very good beam quality of $M^2 < 1.1$, meaning a Gaussian intensity profile. The beams are deflected by two Scanlab hurrySCAN III with an aperture of 14 mm and focused by f-theta optics with an effective focal length of 420 mm . The working distance of the optics is 510 mm , resulting in two scan fields of $280\text{ mm} \cdot 280\text{ mm}$ each. By putting both scan heads next to each other a scan field overlap of 160 mm in width is achieved, which is essential for the two-beam strategies. The minimum focal spot diameter is about

$70\ \mu\text{m}$, but it can be changed to larger values by using the Sill Optics S6EXZ5310/328 zoom beam expanders which allow to change the angle of divergence to move the beam caustic up and down as well as to change the magnification to influence the focal spot diameter. The setup is depicted in Fig. 5.1.

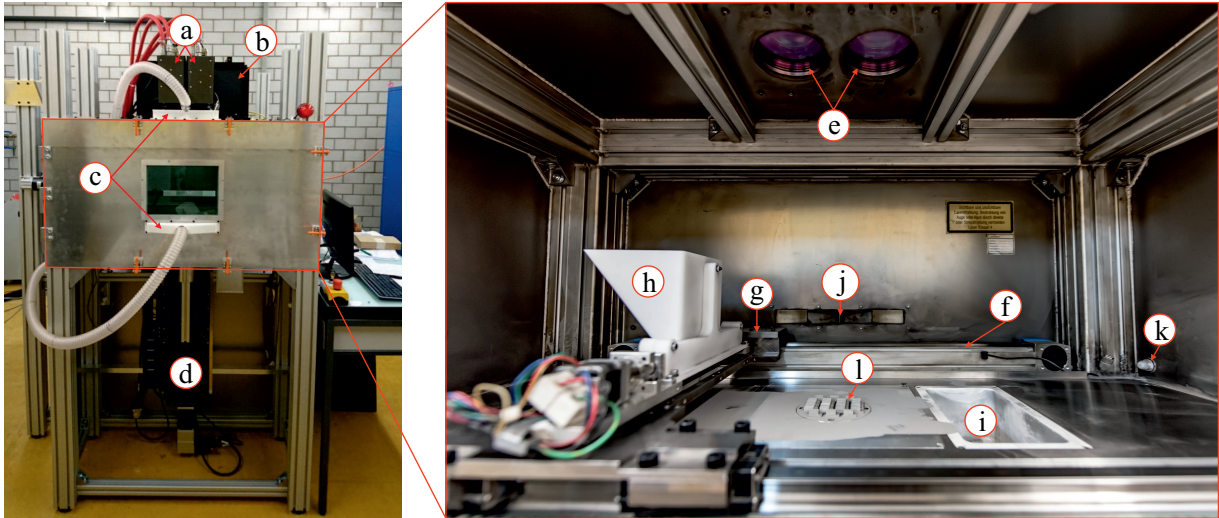


Figure 5.1: Picture of the laboratory machine and a close-up of the build chamber. a) scan head 1 (right) and scan head 2 (left), b) box of beam path including beam expanders, c) shielding gas inlets, d) z-axis, e) laser inlet windows, f) belt drive for powder deposition, g) powder deposition unit, h) powder reservoir, i) powder overflow, j) shielding gas outlet, k) oxygen sensor and l) the build plate, here with parts at an elevated level.

The z-axis is realized by a precise Aerotech PRO225 ball screw drive which allows a travel in z-direction of $250\ \text{mm}$, while the powder deposition axis is a Festo EGC-TB-KF-80-600 belt drive which is driven by an Aerotech BMS280 servomotor to simplify the controls. The build plate is chosen to be $100\ \text{mm}$ in diameter and placed in the center of the scan field overlap. The powder reservoir is on the left of the build chamber above the powder deposition unit. To apply a new powder layer the z-axis is moved down and the powder deposition unit to the left. Then a small amount of powder is dropped onto the base plate by a spline shaft and the powder deposition unit moves to the right again, applying the next powder layer onto the build plate.

The build chamber is filled with nitrogen which is circulated through a filter system and forced into a directed flow over the powder bed from the front to the back. The volume flow over the powder bed is controlled to about $100\ \text{l/min}$. Additionally, a second, not controlled volume flow of about another $100\ \text{l/min}$ keeps the f-theta lenses free of evaporated material. The residual oxygen content is measured in the bottom right corner of the build chamber and controlled to a value of less than 0.5% . In case the value rises over this threshold a valve is opened to add more quasi-pure nitrogen (grade 4.5) to the system.

The control system is made up of an Aerotech A3200 software-based control. The so-called MotionComposer can be used to control the axes via the Aerotech drives as well as the scan heads by using a XY2-100 protocol. Thereby, all available mechanical and optical axes can be controlled fully synchronized by simple G-code programming. It as well includes a software-based programmable logic controller (PLC), called MotionPAC, which is taking care of the digital and analog in- and outputs (I/Os) that are needed for the background machine controls like the control of oxygen content and volume flow, the powder deposition or general machine safety. Yet, MotionPAC is as well capable to control all mentioned axes. MotionComposer and MotionPAC communicate based on shared global variables. A general overview of the control system is given in Fig. 5.2. As the figure shows, in the current machine setup only the optical axes are controlled by the MotionComposer which is fed with G-code, while the mechanical axes are controlled by the MotionPAC. This is done because implementing the powder deposition as a cycle within the background controls, that can be triggered by a global variable out of MotionComposer, allows more simple programs and offers the chance to apply changes to it within the process. In case no synchronized movement of both beams is wanted, controlling both independently, yet simultaneously by separate G-codes is possible as well.

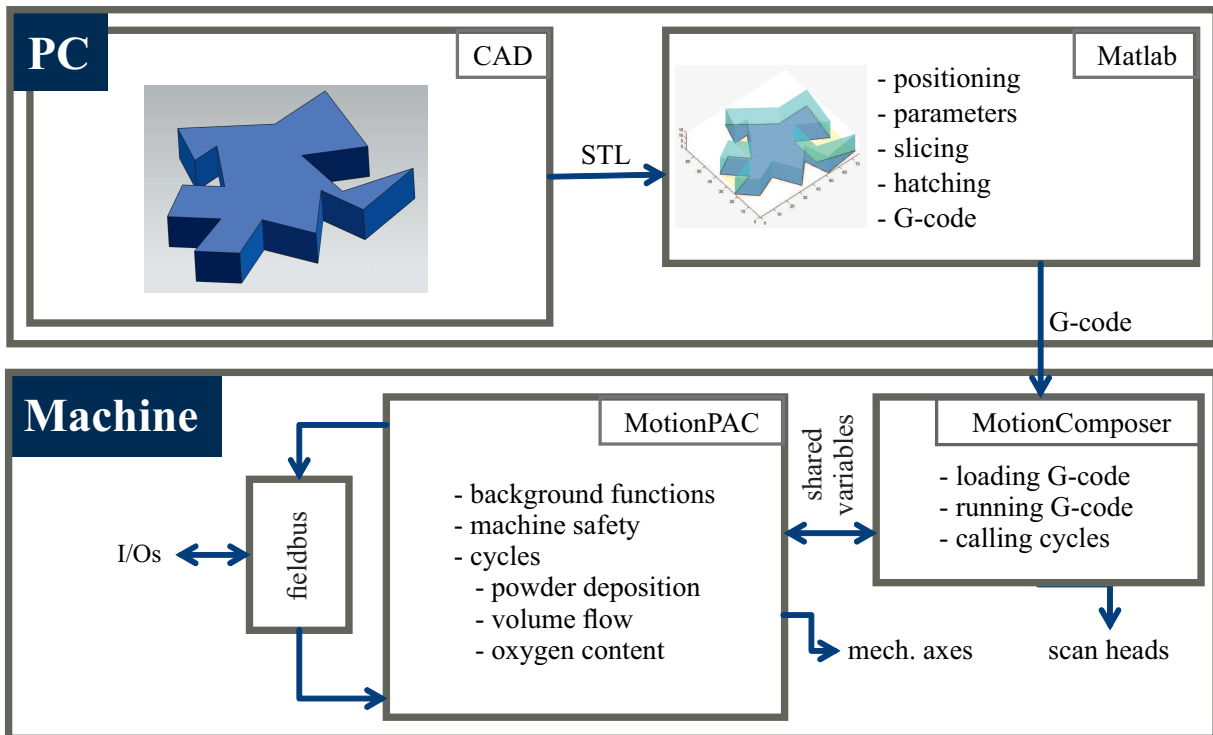


Figure 5.2: Overview of the data preparation and processing in the laboratory machine's control system.

5.1.2 Initial Start-Up

Before using the laboratory machine it is important to check the correlation of the set diode current and the actually available power in the build chamber as well as to check and adjust the spot diameter in the working plane.

The laser power within the build chamber is measured by using a Ophir FL250A-LP1-35 thermopile power meter. The values are checked for both lasers in steps of 5 % of the diode current, starting at the lowest possible value of 10 %. The measured values are listed in Tab. 5.1. The values show a more or less linear correlation of the laser power with the diode current. Yet, a significant offset is observed. Therefore, the measured values are put in a look-up table which is used as a reference in the beam path planning tool to set the correct diode current for the whole range of available powers.

Table 5.1: List of available power of both lasers in the build chamber at different diode currents.

diode current [%]	10	15	20	25	30	35	40	45	50	55
laser power 1 [W]	2	13	24	35	45	56	67	80	91	102
laser power 2 [W]	2	14	25	36	47	58	70	81	92	104
diode current [%]	60	65	70	75	80	85	90	95	100	
laser power 1 [W]	113	124	135	146	157	168	179	191	202	
laser power 2 [W]	115	126	138	149	160	171	182	193	204	

The spot diameter and intensity profile are checked by using a Spiricon SP620U beam camera. The spot is measured off-axis because the beam camera does not fit in the build cylinder. Therefore, first the beam has to be focused to the working plane. The focal spot can be found off-axis since it is defined as the smallest beam diameter in the caustic. When keeping the configuration untouched, the beam diameter in the focal plane can be adjusted. For the initial start-up the beam expander's magnification is used to change the beam diameter in front of the optics which is directly influencing the focal spot diameter. Due to this change the Gaussian profile within the focal spot does not lose any quality. The focal spot size of both lasers is set to roughly $90 \mu m$. For later experiments the second laser's spot size in the working plane needs to be widened. Since reducing the magnification is jeopardizing the optics due to increasing intensities prior to focusing, changing the divergence angle of the beam expander is used to move the caustic so that the focal spot is shifted below the working plane. By doing so, the effective spot diameter in the working plane is increased but the Gaussian profile can be slightly distorted due to optical errors.

5.1.3 High Speed Imaging

The initial setup needs to be changed and extended for high speed imaging. To achieve the necessary, small focal length of the high speed camera's optics, the machine has to be used with an opened front door. To still allow a low oxygen level and a shielding gas flow, the gas inlet is moved to the left of the build chamber. The high speed camera is used with an angle of about 45° to the working plane and the powder bed is strongly irradiated by a separate light source.

A Phantom V12 camera is used for the high speed imaging, recording 30'010 frames per second at $512 \cdot 256$ pixels. An Edmund Optics 1x telecentric objective and a Schneider +3.5 achromatic diopter are used, resulting in an effective pixel size of about $15 \mu m$ along both dimensions and a depth of focus of about $1 mm$. A infrared filter is positioned between sample and optics to shield the high speed camera from possibly harmful reflected laser light. The high speed imaging is done on the basis of $5 mm \cdot 5 mm$ large layers that are located on top of twenty previous layers to guarantee an steady state regarding the deposited powder layer thickness. Preliminary studies showed that a configuration with already solidified lines in the front and the powder bed in the back of the image offers the most information. Therefore, the high speed imaging uses this configuration, in which then the single vectors are directed from the right to the left of the image. The iris is closed almost to its full extent to reduce the overexposure by the laser spot and the resulting material glow. Thereby it is possible to observe the melt pool, the evaporated material, spatter particles as well as neighboring powder of the upcoming tracks.

5.2 Software Tools

5.2.1 Beam Path Planning

A Matlab-based CAD/CAM-tool is implemented to allow the automated generation of G-code while having the maximum freedom in possible processing strategies. The tool starts with the import of a STL-file, similar to the common way of data processing in additive manufacturing. The file is then sliced into a large number of layers with a defined thickness. The layer data is used to identify the contour and the core of the imported parts, which again is needed to assign the irradiation strategies and processing parameters to the different regions of various parts. Additional to the common strategies of uni- or bidirectional hatching with a certain scan speed, laser power and hatch distance and the rotation of the hatching direction with every layer as well as the widely applied island

or checkerboard pattern, the implemented tool offers the use of various new two-beam strategies. Those are described in the following and summarized in Fig. 5.3.

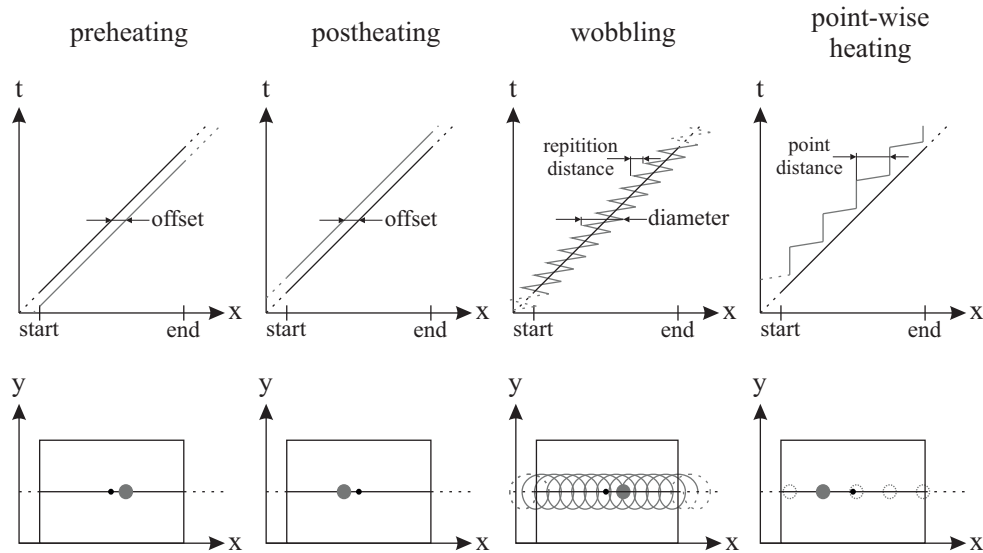


Figure 5.3: Overview of implemented two-beam strategies. Solid lines illustrate movement with laser emission, dashed lines illustrate movement without laser emission. Black lines show the movement of the first laser and gray ones of the second laser.

The first group of strategies are those with a defined, fixed offset which is why those will be referred to as **offset strategies** in the following. In these cases the beams move synchronously along every scan vector. The path is generated by a simple translation of the start and end points of the vector, more precisely the skywriting start and end points, along the desired offset. Skywriting is considered to be an additional movement while the beam is turned off so that the mirrors in the scan head can accelerate and decelerate to the desired speed of the scan vector. The moment of laser emission is adjusted to the actual geometry after translating the points to guarantee geometrical accuracy. Thereby, the skywriting start length of the second beam and the skywriting end length of the first beam are increased if the second is set to follow the first one in a defined offset. The offset can be freely defined in scan direction and perpendicular to it. Yet the start and end times of laser emission of both lasers need to be one clock time apart because the control systems cannot handle it otherwise. Hence, a minimum offset in scan direction of scan speed, for example 1000 mm/s , times the clock time of about $21\ \mu\text{s}$ is necessary, in this case resulting in a minimum offset of $21\ \mu\text{m}$. While offsets perpendicular to the scan direction won't be discussed in further detail in this thesis, the offset strategies in scan direction are differentiated regarding the direction of the offset. If the second beam is moving in front of the first beam the term of **preheating** will be used while the opposite case is referred to as **postheating**.

The second group is the **wobble strategy** which is directly linked to the offset strategies. Wobbling is considered the circular or ellipsoidal movement along a linear vector that can easily be added by overlaying the scan head's input signal with sine-curves in both axes. Hence, the original path is generated using the same functions used for offset strategies and just an additional control specific term is added. In that the movement's radius in scan direction and perpendicular to it as well as the repetition distance is defined. In the following only the second beam will be wobbled, resulting in a circular movement of the second beam around the first one.

The third group is the one of **point-wise heating**. This group is still defined by a motion synchronized control of both beams, but not by a continuous movement of both. While the first beam is continuously irradiating the powder material as a single laser would do, the second beam stays at a point of the scan vector for a short time before moving to the next point which is in a defined distance. The moving speed of the second beam is obviously far higher than the one of the first beam to make the strategy work.

5.2.2 Image Processing

The high speed imaging results in a very large amount of data that needs to be analyzed. Furthermore, the apparent movement speed of spatter particles within the high speed images is still quite fast, although 30'010 frames per second are imaged. Therefore, a Matlab-based image processing tool for identifying, tracking and counting spatter particles is developed.

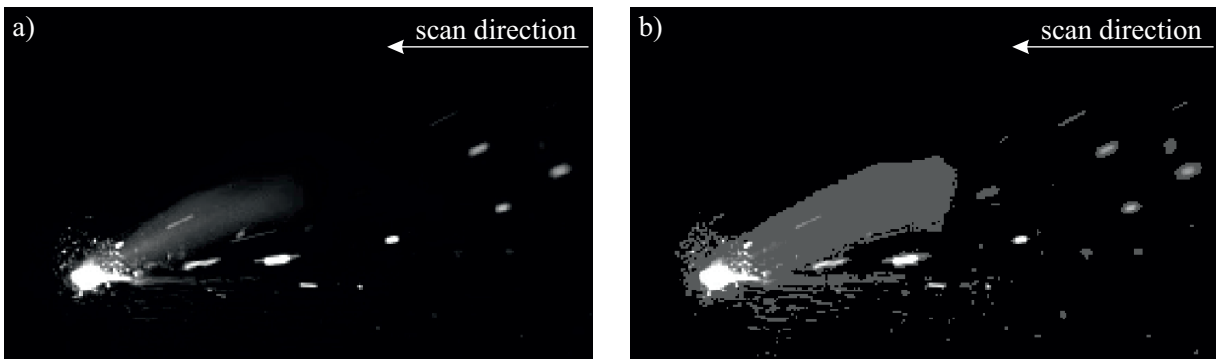


Figure 5.4: Comparison of a) the original image and b) the version which was improved regarding grayscale values to maximize the algorithms capabilities.

First, the images need to be prepared to achieve a higher contrast so that the following algorithms reach a higher accuracy in identifying spatter particles. Hence, grayscale values lower than a threshold of 25 are set to zero and grayscales within the range of 26 to 99 are

boosted to a grayscale value of 100. These values have been calibrated by using different sets of high speed images of different processing parameters. The resulting change of grayscales is depicted in Fig. 5.4.

Second, the modified images are then used to find distinct features within the image by using the Matlab-internal functions of *imfindcircles* and *detectMinEigenFeatures*. While *imfindcircles* tries to fit circles into the image and can thus be used to identify the position of the laser beam, *detectMinEigenFeatures* identifies distinct points based on maximum grayscale gradients. Yet, using grayscale gradient bears the problem that distinct points are not only detected on spatter particles but as well at the border of the bright vapor jet. Therefore, a safe zone is drawn around the identified laser spot, deleting all distinct points within a certain radius around it, as shown in Fig. 5.5. This radius is calibrated to a size of 100 pixels.

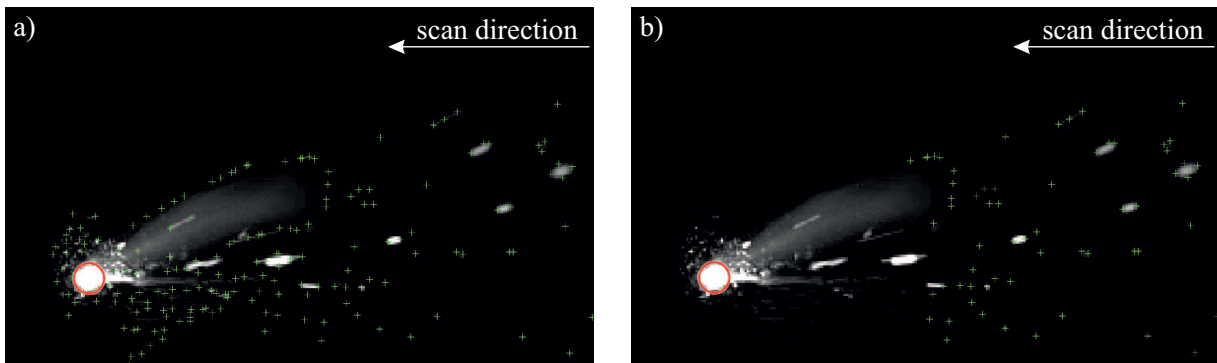


Figure 5.5: Illustration of the numerically identified laser spot and distinct points within the image. a) shows every identified point and b) a cleaned-up version in which most of the distinct points within the vapor jet have been removed.

Third, the identified distinct points need to be tracked over several images to calculate spatter velocities on the one hand and to eliminate residual points, that are not associated to a spatter particle, on the other hand. A distance-based approach is used to do that. Hence, the distance and angle of every distinct point to neighboring points is calculated and saved for every single frame. Under the assumption that spatter particles won't rapidly change size or direction of flight the values of distance and direction can be checked for reoccurrence in a sequence of images. Thereby it is possible to track spatter particles even if the algorithm failed to identify the same distinct points in single images of the sequence. The procedure is depicted in Fig. 5.6.

Since more than two distinct points might be identified by the matlab function on a single spatter particle and since there is a chance that two particles are moving next to each other with roughly the same speed, the tracks need to be filtered and checked for double

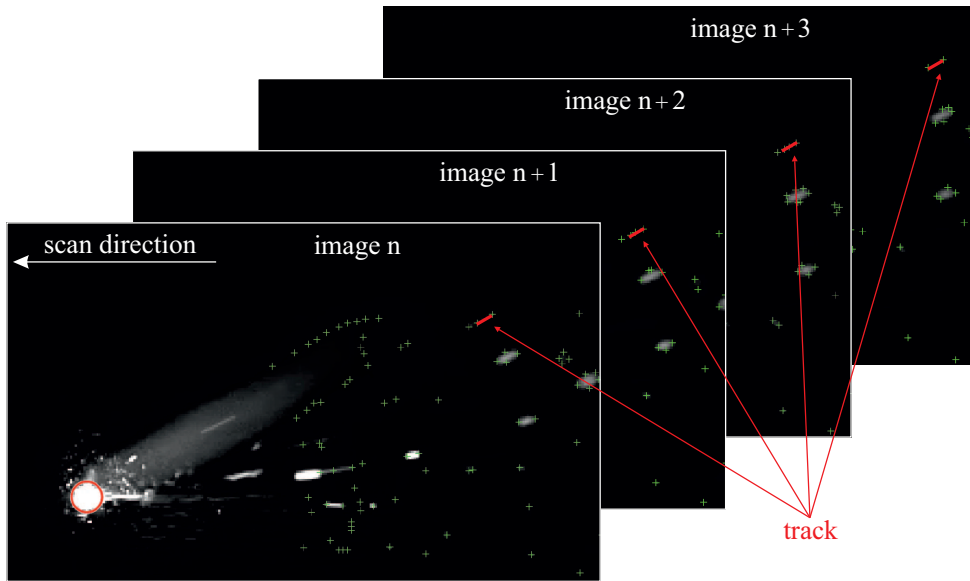


Figure 5.6: Example of the tracking of spatter particles by tracking sets of points with the same distance and angle over a sequence of images.

occurrences. A hand count of spatter particles in three high speed videos showed that about 75 % of the spatter particles are accurately identified by the presented tool.

The spatter particles are differentiated based on the grayscale value. Spatter with a grayscale equaling the boosted value of 100 are considered dark spatter, while particles with a higher grayscale value are referred to as bright spatter. Dark spatter is assumed to be cold powder spatter and bright spatter either hot powder spatter or melt pool spatter. Yet, it is hard to precisely differentiate cold and hot powder spatter based on the grayscale value so that there is a residual factor of uncertainty.

5.3 Methods

5.3.1 Scan Field Calibration

Calibrating the scan fields so that both are perfectly aligned to one another is a necessary step before using two-beam strategies. In the initial set-up both scan fields are just roughly aligned by translation and a small rotation to a common coordinate system which is located in the center of the build plate. Yet, to guarantee the necessary accuracy for parameter sets, in which for example a static beam offset as small as $45 \mu m$ is used, a more precise alignment is necessary. Additionally, because of temperature changes in the shop floor, changes in the build plate thickness and due to the large working distance of $510 mm$, it is necessary to repeat the calibration step before every single two-beam experiment.

To start the calibration process, the build plate is leveled to the desired working plane and is covered by a sample plate with a defined thickness. The z-axis is moved down by the defined thickness, here commonly 2 mm . One laser-scanner-system marks crosses at defined, equidistant positions which are distributed all over the sample plate and the task is repeated with crosses that are rotated by 45° within the xy-plane by the second laser-scanner-system. In a perfectly aligned system the crosses' center points should be right above one another. Thus, the offset of the crosses' center points can be measured at every single position for calibration purposes. The offsets are measured using a Leica DCM3D microscope with a 5x objective, resulting in an effective magnification of 50x.

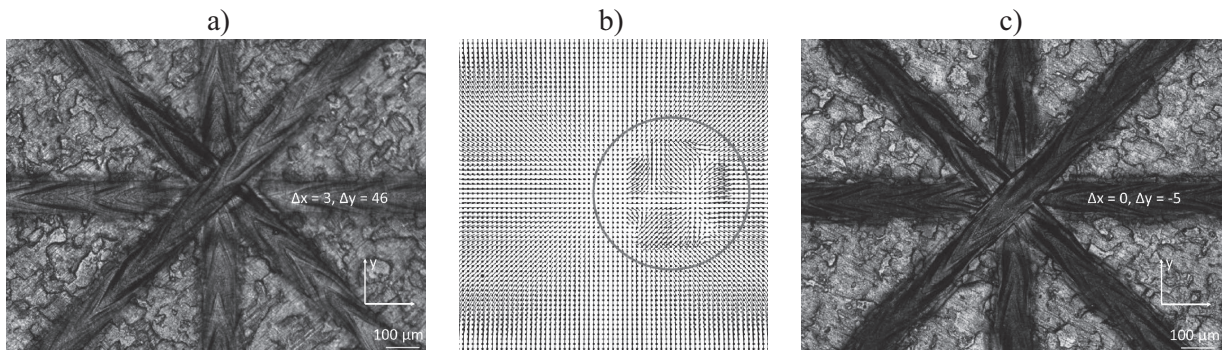


Figure 5.7: Calibration procedure starting with the marking and a) measuring the offset of the sets of crosses, b) changing the scan head's calibration file (here 100 times amplification) and c) checking the calibration.

The data is used to change one scan head's calibration file, which is commonly used to correct errors in the optics and lenses. The values in between the marked crosses are interpolated. Fig. 5.7 shows the procedure on the basis of a single set of crosses and an amplified correction. After correcting the scan head's calibration file the calibration is checked again and if necessary repeated until a residual error of less than $20\ \mu\text{m}$ is achieved for every single set of crosses. A significant change of the calibration during the build-up of parts has not been observed. Still, the calibration procedure is an inherent drawback of the two-beam strategies due to the necessary time that has to be spend in before any two-beam build job.

5.3.2 Density Measurement

Any investigated parameter set is first investigated regarding its resulting density because it is a good indicator for a parameter set's quality. Cubic samples of $10\text{ mm} \cdot 10\text{ mm} \cdot 10\text{ mm}$ are used to do that. The density measurement is done by using the Archimedes principle, meaning that the sample's weight is measured in air and in a fluid. The weight difference

as well as the temperature dependent densities of air and fluid can be used to calculate the samples volume. With the knowledge of weight and volume the sample's density can be calculated. Acetone is chosen as the fluid because it has a low surface tension and thereby minimizes the measurement error due to air bubbles that stick to the samples surface. Yet, using a low surface tension fluid makes it necessary to guarantee a closed contour so that the fluid is not infiltrating the possibly porous sample.

5.3.3 Microstructural Analysis

The microstructural analysis of the samples is necessary to get additional information on the melt pool dimensions and shapes that are directly influencing other indicators such as density and surface roughness. Furthermore, the microstructure offers a great chance to get further insight to what happened during the melting and solidifying of the material. For that the melt pool dimensions and shapes in the uppermost layer of cubic samples are investigated. The samples are cut in a way that the scan direction in the uppermost layer is perpendicular to the cross section.

All samples are embedded, ground using 500 and 1000 grit sand paper and polished using $6\ \mu\text{m}$, $1\ \mu\text{m}$ diamond and $60\ \text{nm}$ alumina solutions. Samples of stainless steel AISI 316L (X2CrNiMo17-12-2) are etched in V2A etchant at $60\ ^\circ\text{C}$ to $70\ ^\circ\text{C}$ for $90\ \text{s}$ each. Samples of AISI 4140 (42CrMoS4) are etched in an alcoholic solution with 3% nitric acid for about $10\ \text{s}$ each.

5.3.4 Distortion Measurement

The resulting distortion of a chosen parameter set is quantified based on cantilever samples, as illustrated in Fig. 5.8. The cantilever's geometry has been optimized to result in a reproducible deflection of maximum extent. The deflection is measured using an Alicona InfiniteFocus with a 5x objective, resulting in an effective magnification of 50x.

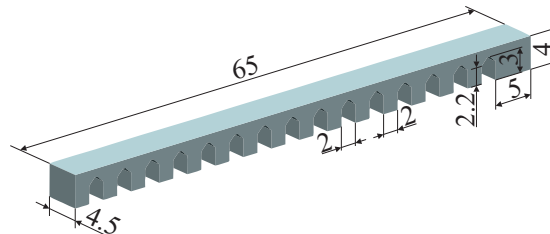


Figure 5.8: Dimensions of the cantilevers that are used for the quantification of the resulting distortion of a chosen parameter set.

The deflection of the cantilevers is evaluated measuring the height profile of the cantilevers perpendicular to its long axis. Therefore, the initial height before releasing the stresses is calculated by the distance from the top of the cantilever to the build plate. After cutting the support of the cantilevers up to the 5 mm wide post and thereby releasing the residual stresses, the measurement is repeated leading to a new height. The difference of the new height to initial height is taken as the cantilever's deflection. The height profile is always measured in a 1 mm distance from the edge of the cantilever. The values are averaged over the cantilever width to decrease the influence of the part's surface roughness.

5.3.5 Crack Penetration Depth Measurement

In contrast to the distortion measurement, the martensitic steel AISI 4140 is investigated in regards to its cracking susceptibility and the strategies' influences on the extent of cracking. Therefore, notched beams, as depicted in Fig. 5.9, are built to have a predetermined breaking point from which a crack penetration depth can be quantified. The beam are irradiated like all other samples with a unidirectional hatching which is rotated by 90° after every layer.

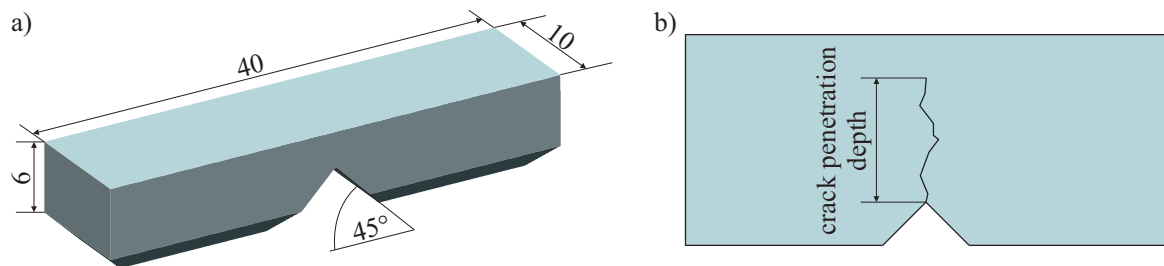


Figure 5.9: a) Dimensions of the notched beam geometry which is used for the quantification of the resulting crack penetration depth. The bottom part is just support structure to simplify the cut-off. b) Way of measuring the crack penetration depth.

The crack penetration depth is measured as the linear distance from the top of the notch to the end of the crack in the investigated cross section. The cross sections are imaged using a Alicona InfiniteFocus with a 20x magnification and thus an effective magnification of 200x.

5.3.6 Surface Roughness Measurement

The focus of the surface roughness measurement lays on the smoothness of the transition between neighboring tracks, since those are limiting the achievable surface roughness if

random effects like spatter and recoating errors are neglected. The surface roughness is evaluated optically by using a Leica DCM3D microscope with a 20x objective, resulting in an effective magnification of 200x. The investigated surface areas are of a size of $2.36\text{ mm} \cdot 1.77\text{ mm}$. Sections with an inclination angle of more than 80° as well as single outliers are excluded from the results because of the high probability that those are a result of measurement errors. The data set is split using a Gaussian filter with a cut-off length of 0.25 mm to differentiate between waviness due to random errors or imperfections and the surface roughness due to neighboring tracks. The surface roughness is then investigated by ten equidistant roughness profiles that are oriented perpendicular to scan direction. The arithmetical mean deviation R_a of surface roughness is calculated based on these ten profiles and used as the indicator for the transition smoothness of neighboring tracks. The procedure and the difference in the two data sets is illustrated in Fig. 5.10.

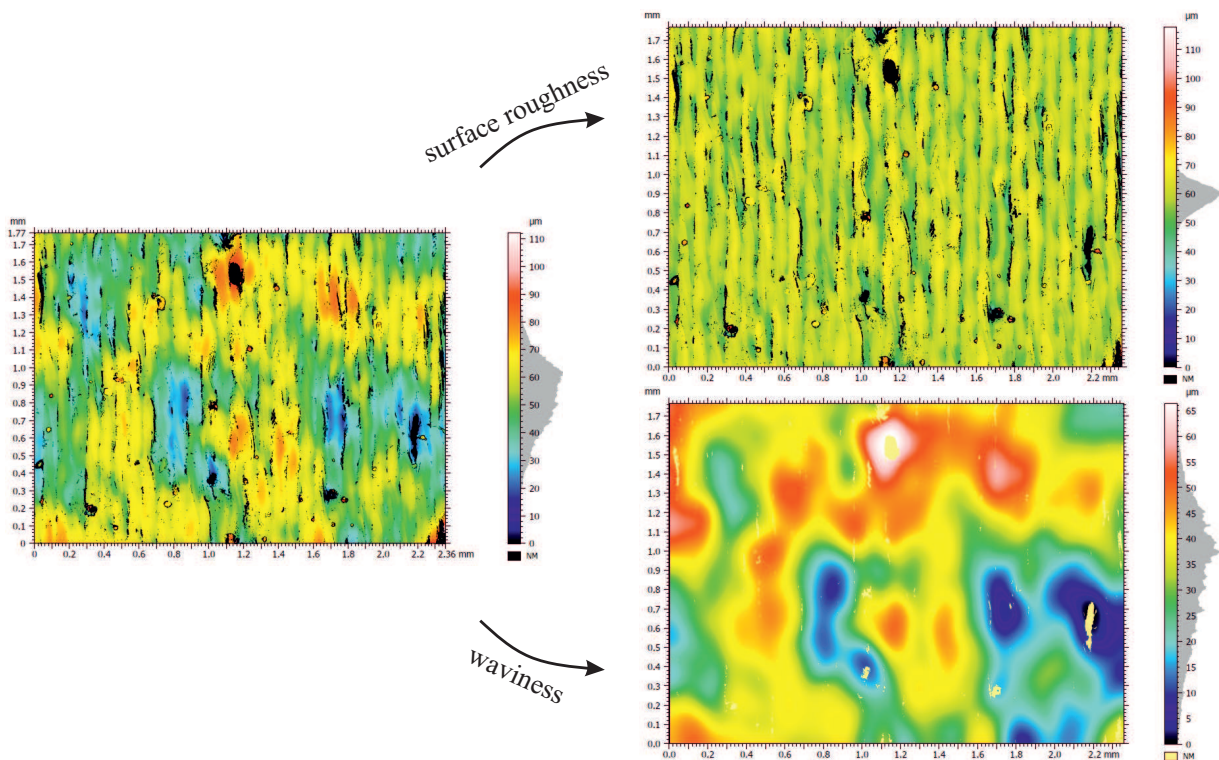


Figure 5.10: Result of splitting the left image by a Gaussian filter with a cut-off length of 0.25 mm into the data sets of surface roughness and waviness. The waviness contains the height profile due to random errors and imperfections, while the surface roughness data set contains the height profile due to neighboring tracks.

Chapter 6

Investigation of Two-Beam Strategies

The two-beam strategies are investigated using experiments which are supported by numerical simulation. The main focus are the offset strategies of preheating and postheating. Wobble strategies as well as point-wise heating are investigated as well but to a lesser extent. The evaluation is based on the criteria of density, microstructure, spatter characteristics, surface roughness and the strategies influence on deflection of cantilever samples. Selected effects are investigated in more detail with the help of the simulation tools. The values are compared with reference values of single-beam samples which are given in the beginning of this chapter.

6.1 Setting a Reference

First, a reference needs to be set with which the different two-beam strategies are compared. Therefore, a single-beam reference is used which could actually be used for the manufacturing of parts on commercial SLM machines. By taking the previously discussed evaluation of the numerical model into account the range of possible process parameters can be decreased to a small number that needs to be investigated because of the change of machines from a commercial ConceptLaser M2 to the IWF laboratory machine. The simulation, that elaborated similar beam diameters and powers as the laboratory machine does, shows that a change of melting behavior can be expected around a scan speed of 1000 mm/s , as it has been discussed in section 4.4. So only the small range of scan speeds (850 mm/s , 1000 mm/s , 1150 mm/s) and hatch distances ($75\text{ }\mu\text{m}$, $82.5\text{ }\mu\text{m}$, $90\text{ }\mu\text{m}$, $97.5\text{ }\mu\text{m}$) is used to transfer the knowledge from the simulation and the commercial machine's experiments and thus to find an optimal processing parameter for the laboratory machine.

The results of the density measurements of those twelve samples are depicted in Fig. 6.1. It shows that the highest density is always achieved at a hatch distance of $82.5 \mu\text{m}$, which is why this is chosen as the hatch distance for the upcoming investigations. At higher as well as lower hatch distances the density drops to lower values. The difference between the scan speeds of 850 mm/s and 1000 mm/s is very small compared to the difference when increasing the scan speed to 1150 mm/s . Therefore 1000 mm/s is chosen as the reference sample's scan speed because of the higher possible productivity.

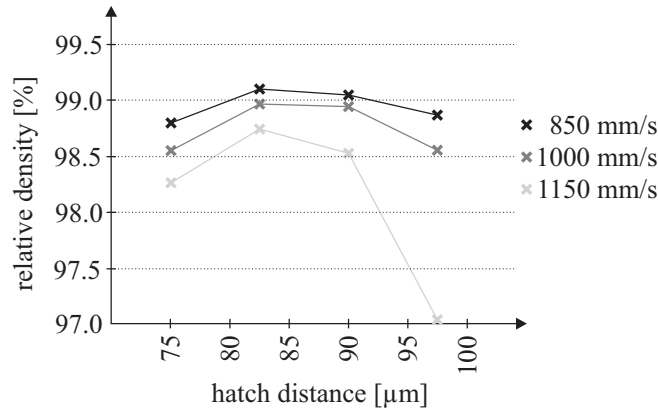


Figure 6.1: Measured densities of the single-beam reference samples for different scan speeds and hatch distances. The power was kept constant at 200 W and the spot diameter at $90 \mu\text{m}$. The densities are set relative to the bulk material density of 7.98 g/cm^3 .

It has to be noted that the density values of about 99% are not as high as they are expected to be when using a commercial SLM machine. This is due to a less effective shielding gas flow that does not transport spatter particles perfectly to the shielding gas outlet, so that spatter particles tend to drop on samples and are thereby increasing the risk for lack of fusion. By optimizing the shielding gas inlet this effect has been reduced but could not be completely extinguished, so that the mean density value increased slightly. Either way, the microstructure is dense in general, as shown in Fig. 6.2 but large pores occur randomly within the samples due to spatter particles that landed on them. Hence, the density values of all samples are set into relation with the reference sample's density to evaluate the change of properties by elaborating two-beam strategies.

Fig. 6.3 depicts high speed images of the chosen reference parameter set to get an idea of how a single-beam strategy with given parameter sets looks like within the high speed imaging. It shows a strongly irradiated melt pool front and a glowing melt pool tail as well as a directed vapor jet to the back of the melt pool and spatter particles in and around the vapor jet. The high speed imaging has been done at two different dates with some month in between, which means that the camera setup (position, incident angle and lighting) changed in between. The different setups led to notably different spatter counts

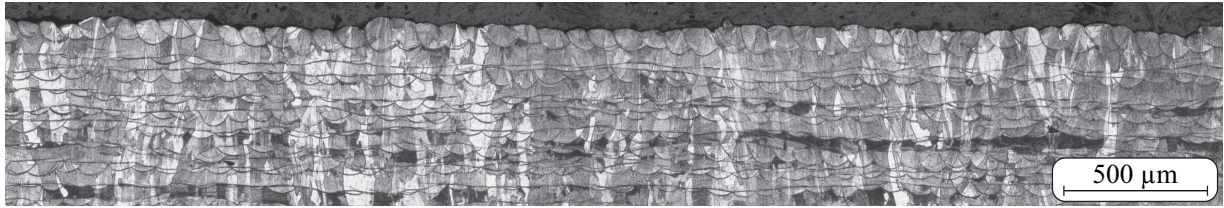


Figure 6.2: Microstructure of the reference sample manufactured at 1000 mm/s , 200 W , $82.5\text{ }\mu\text{m}$ hatch distance and $90\text{ }\mu\text{m}$ spot size. It shows a completely dense microstructure in general which can occasionally be disturbed by large spatter particles and resulting pores due to lack of fusion.

given by the automated processing of the high speed images. Hence the values of the the two beam strategies are set into relation of the same setup reference mean values of 196 particles/mm for the first setup and 278 particles/mm for the second setup.

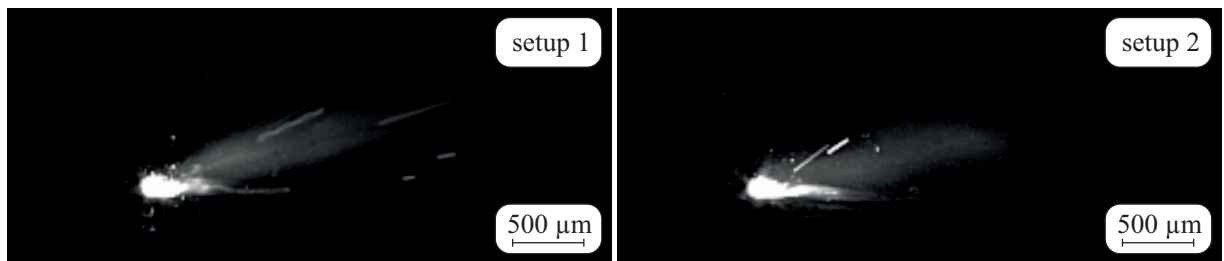


Figure 6.3: High speed images of the reference samples. The beam is moving from right to left.

The difference in lighting can be observed when having a look on the melt pool glow which is overall slightly brighter in the second setup. This indicates a generally brighter image that might make spatter detection easier and thereby results in higher spatter counts.

The unfiltered and filtered surface structure of the reference sample is shown in Fig. 6.4. Within the unfiltered image random height changes can be seen that can be explained by random errors like spatter particles and errors in the powder deposition. The filtered image shows the line structure which is a result of the chosen hatch distance. The mean value of surface roughness after filtering the image to get rid of the waviness is $3.24\text{ }\mu\text{m}$ with a minimum of $2.62\text{ }\mu\text{m}$ and a maximum of $3.61\text{ }\mu\text{m}$ within the ten measured height profiles. The two-beam strategies' values are set into reference of this mean surface roughness.

In case of cantilever samples a reference sample is built within any build job to account for possibly different heat accumulation within the build plate that might change the result of measured deflection. The two-beam strategies' values are thus compared to the same build plate reference sample and the relative deflection is used to evaluate the strategies' influence. The reference sample's mean values of density, spatter count, surface roughness and deflection are given in Tab. 6.1 together with the minimum and maximum values.

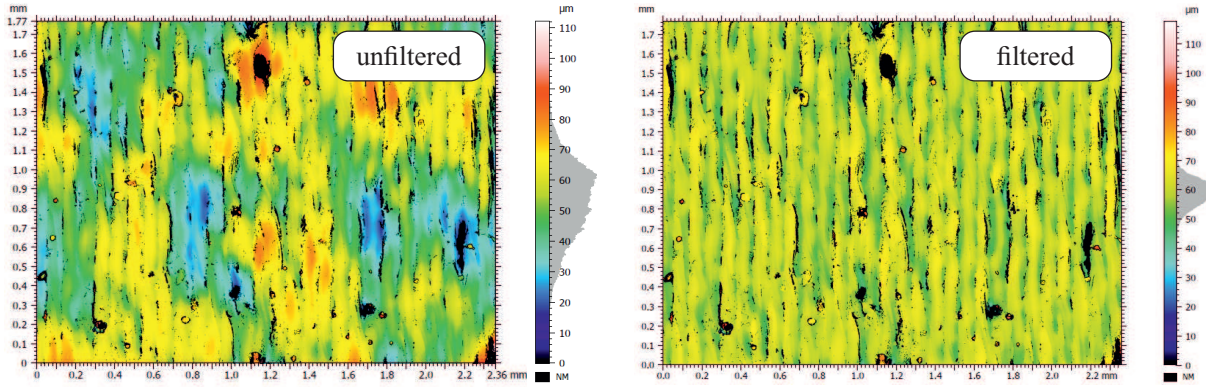


Figure 6.4: Surface profile of the reference sample, unfiltered as well as filtered with a cut-off length of 0.25 mm to exclude the waviness due to random process errors.

Table 6.1: List of mean, minimum and maximum values of the reference sample's density, spatter count, surface roughness as well as deflection. The spatter count is differentiated for the first and second high speed imaging setup.

	Mean	Minimum	Maximum
relative density [%]	99.1	98.9	99.3
spatter count 1st setup [$p./mm$]	196	155	246
spatter count 2nd setup [$p./mm$]	278	185	414
filtered surface roughness [μm]	3.24	2.62	3.61
cantilever deflection [mm]	3.69	3.48	3.90

6.2 Offset Strategies

6.2.1 Experimental Planning

The offset strategies are investigated for two different heating beam diameter and power setups. One being fixed to a beam diameter of $270\ \mu m$ and a power of $100\ W$ and the second being defined by a heating beam diameter of $380\ \mu m$ and $200\ W$. These combinations are chosen because both result in the same peak intensity of the heating beam. The first set results in power being distributed over a nine time as large area than it is the case for the melting beam. In case of the second heating beam setup the power is distributed even over a about eighteen times as large area. Thereby, the amount of melting by the heating beam is kept at a low level, although it is not completely excluded.

The scan speeds are chosen to be in a range from the reference sample's one to a speed that results in the same energy density as the reference sample. Therefore, the first heating beam setup is investigated for speeds of $1000\ mm/s$, $1250\ mm/s$ and $1500\ mm/s$, while the second setup is used for scan speeds of $1000\ mm/s$, $1500\ mm/s$, $1750\ mm/s$ and

2000 mm/s . The offsets are chosen to be $-270 \mu m$ to $450 \mu m$ in $90 \mu m$ steps, with negative offsets being considered preheating and positive offsets postheating. A $0 \mu m$ offset is not possible due to the controls system as explained in subsection 5.2.1. Therefore $\pm 45 \mu m$ offsets are included. A lower maximum offset for preheating strategies is chosen because it is assumed that the power input will otherwise not influence the melt pool anymore.

The melting beam is constantly kept at $90 \mu m$ beam diameter and $200 W$ power, the hatching at $82.5 \mu m$ and the layer thickness at $30 \mu m$. Combining the offset strategy parameters 70 sets will be investigated, 30 for the lower power setup and 40 for the higher power setup.

The high speed images in Fig. 6.5 show the beam configuration and a rough overview of the influence on the melt pool of the maximum offsets for a $380 \mu m$ heating beam at $1000 mm/s$ as a proof of concept.

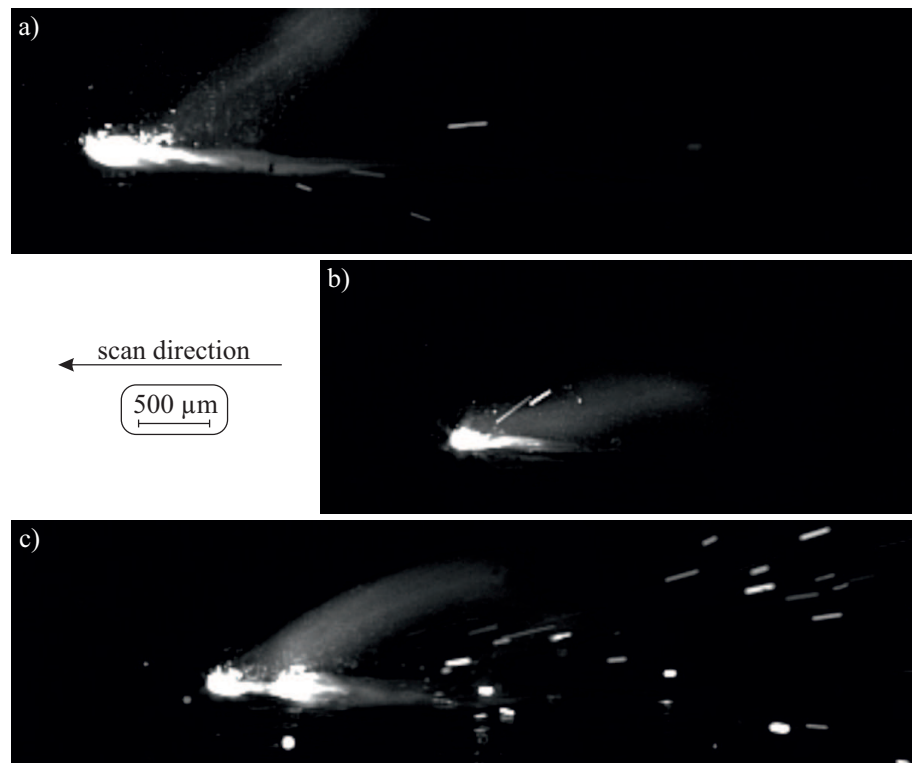


Figure 6.5: Images of the process in case of a $380 \mu m$ heating beam diameter, $200 W$ heating power and a scan speed of $1000 mm/s$. a) preheating with an offset of $-270 \mu m$, b) reference single-beam sample, c) postheating with an offset of $450 \mu m$.

A large difference in the general occurrence of the melting process and melt pool can be seen within these images. In case of preheating the highly glowing front of the melt pool is enlarged but no differentiation between heating and melting beam is possible. Yet, the

origin of the vapor jet indicates that the melting beam is not in the very front of the melt pool. The melt pool length and width are far larger than in case of the reference sample. This is also the case for the postheating parameter set. In contrast to the preheating, a clear differentiation between the two beams is possible when using a postheating offset of $450\ \mu\text{m}$. The front of the melt pool is similar to the reference sample's one. Even a narrow melt pool can be observed in between both beams. Yet, this narrow melt pool is widened significantly by the following heating beam.

The images already show a difference in the melt pool dimensions and spatter count, which are discussed in more detail in the following.

6.2.2 Microstructure and Density

The resulting microstructure and its dependencies of the chosen offset are discussed for each of the seven combinations of speed and heating beam diameter separately. First, the samples with a heating beam diameter of $270\ \mu\text{m}$ and a heating beam power of $100\ \text{W}$ are discussed and then followed up by the $380\ \mu\text{m}$ diameter and $200\ \text{W}$ heating power samples. Although the second beam's power is always referred to as heating power within this thesis, the cross sections show that this additional power is as well taking part within the melting process.

Fig. 6.6 shows the first set of offset samples' cross sections at a scan speed of $1000\ \text{mm/s}$. The first impression is that the melt pools with either low preheating or postheating offsets are significantly larger in their dimensions than the reference sample's ones. This is obviously due to the additional heat input which is leading to enlarged melt pool dimensions. The melt pool depth is increased especially when the additional power is absorbed at the time when the maximum melt pool dimensions are reached. The additional power is then directly increasing the peak intensity of the effective beam profile which is a result of the overlaying intensity profiles of the two single beams.

This effect of enlarged melt pool depths can be observed for offsets from about $-90\ \mu\text{m}$ to $270\ \mu\text{m}$. It shows that the postheating offsets are more beneficial when considering the melt pool dimensions as a criterion for the overall process quality, since larger melt pools allow larger hatch distances and are reducing the risk of lack of fusion errors within the microstructure. The larger range of postheating offsets for enlarged melt pool depth can be accounted to the fact that the highest melt pool depth is achieved slightly behind the melting beam's center point as already discussed in subsections 2.1.3 and 4.4.3. Furthermore, the cool down of the melt pool is slowed in case of postheating which gives heat conduction slightly more time to increase the melt pool dimensions.

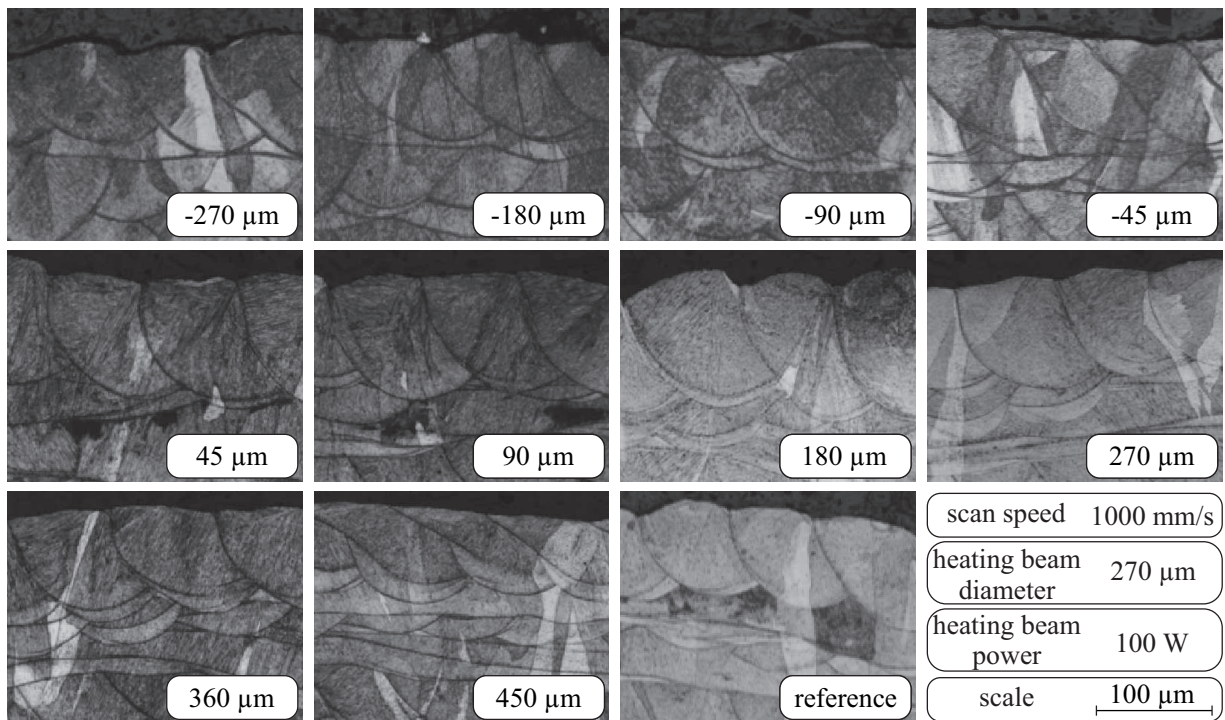


Figure 6.6: Etched cross sections of offset strategy samples manufactured with different offsets. Negative offsets are considered preheating, positive ones postheating. The bottom right image shows the reference sample's cross section.

A second difference in the melt pool cross sections can be seen especially for the postheating offset of $450\ \mu\text{m}$. It shows distinct double melt pool boundaries which are a result of the first beam's melting of the material independent of the heating beam. The maximum depth is already reached and the melt pool starts solidifying before the second beam reaches the position. As soon as the heating beam reaches the cross section the solidification is stopped and possibly a slight remelting of the already solidified material occurs. Thereby a second melt pool boundary is generated. This effect is discussed in more detail later on in subsection 6.2.6 with the help of the simulation tool. Due to the independence of both beams the upper melt pool area is significantly widened because the second beam intensity is leading to a more severe Marangoni convection which is suppressing the capillary forces that are commonly resulting in a half-spherical melt pool shape. The suppression of the capillary forces is as well resulting in a smoothing of the top surface.

A small scale widening of the melt pool's upper regions can occasionally be observed for all offset strategy parameter sets because of the slight remelting of neighboring tracks by the widened heating beam.

Fig. 6.7 shows the same offsets at a scan speed of $1250\ \text{mm/s}$. In general the same effects are occurring but the melt pool dimension of low offsets are not larger than the reference

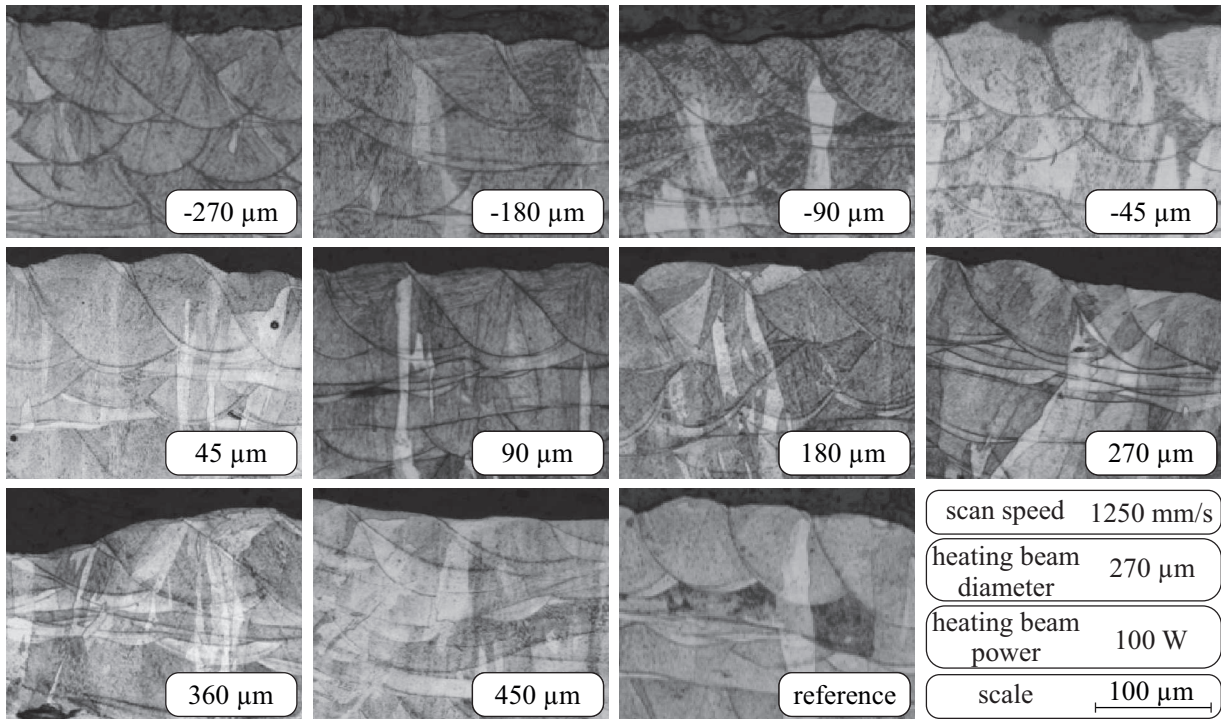


Figure 6.7: Etched cross sections of offset strategy samples manufactured with different offsets. Negative offsets are considered preheating, positive ones postheating. The bottom right image shows the reference sample's cross section.

sample's anymore. Yet, about the same melt pool dimensions are achieved although the scan speed is 25 % higher than the reference sample's one. Additionally, the cross sections show the same double melt pool boundaries but they are already present at postheating offsets as low as $180 \mu m$.

Fig. 6.8 completes the picture of offset strategies with a heating beam diameter of $270 \mu m$ at $100 W$ power by showing the results for a scan speed of $1500 mm/s$. The parameter sets still result in comparable melt pool dimensions for low offsets, which shows that the heating beam power can be fully used for the melting process within these offsets because at this speed the overall energy density is equally high as the reference sample's one. Yet, in case of this heating beam setting a third of the input power is distributed over a nine times as large area.

By using this heating beam diameter and power the changes in melt pool dimensions for preheating parameter sets are less significant. This is due to the fact that the heating power input is done in front of the main melt pool and thereby no significant influence on the melt pool dynamics or solidification process is present. When changing the heating beam setup to a beam diameter of $380 \mu m$ and $200 W$ heating power, the previously discussed effects become more distinct. Fig. 6.9 shows the influences at a scan speed of $1000 mm/s$.

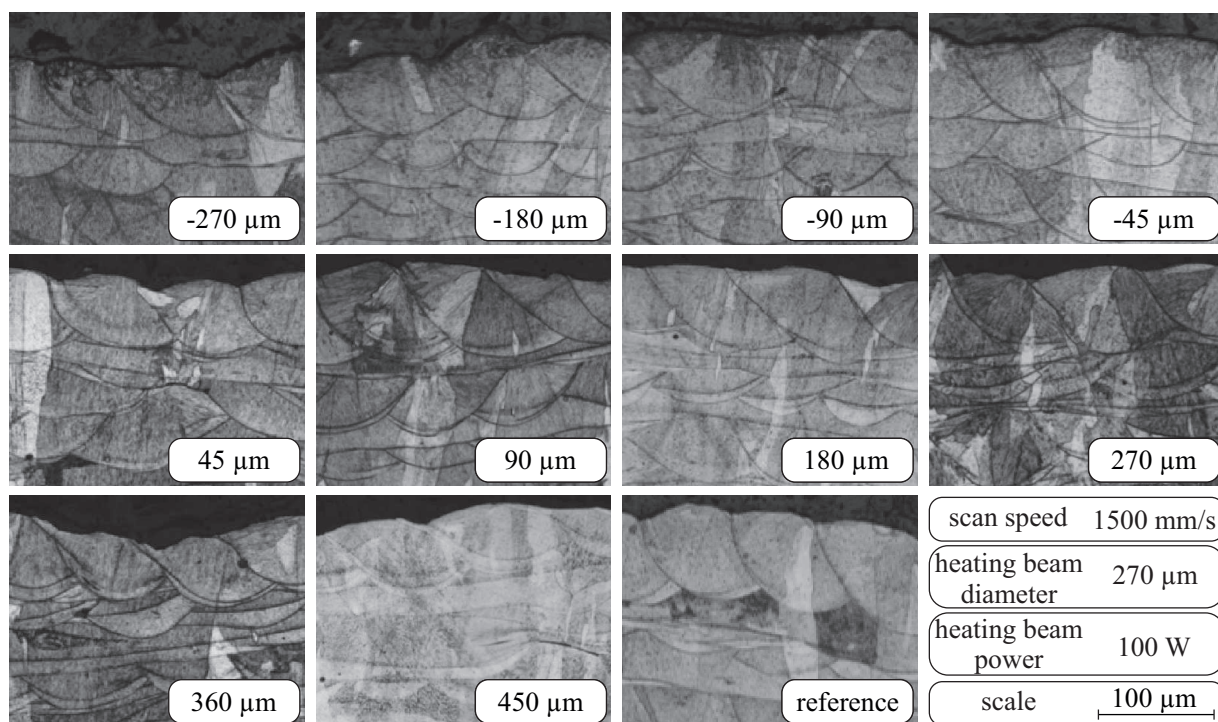


Figure 6.8: Etched cross sections of offset strategy samples manufactured with different offsets. Negative offsets are considered preheating, positive ones postheating. The bottom right image shows the reference sample's cross section.

The cross sections show a significant enlargement of the melt pools as well. In contrast to the smaller heating beam samples, the upper melt pool regions are widened much stronger. The melt pools are reaching widely over the previous tracks which has to be accounted to the larger heating beam diameter. The widening of the upper melt pool regions increases the smoothing effect because the capillary forces fail to form a half-spherical melt pool at such high melt pool widths.

The double melt pool effect can be observed as well. Yet it seems that the extent is more reproducible and the distance between lower and upper melt pool boundary is larger. The higher reproducibility might be due to the fact that the interaction time of the heating beam with the melt pool is longer due to the larger diameter, guaranteeing that the solidification is stopped or reversed for a short period of time.

As Fig. 6.10 shows, the effect of postheating on the dimensions and shape of the melt pool is far stronger than it is for preheating offsets. Especially the remelting of previous tracks is stronger for postheating, which is possibly beneficial for the surface quality as well as the part's density.

When scanning even faster, the in-situ remelting of neighboring tracks as well as for large offsets the currently irradiated one is becoming more important, as Fig. 6.11 shows for a

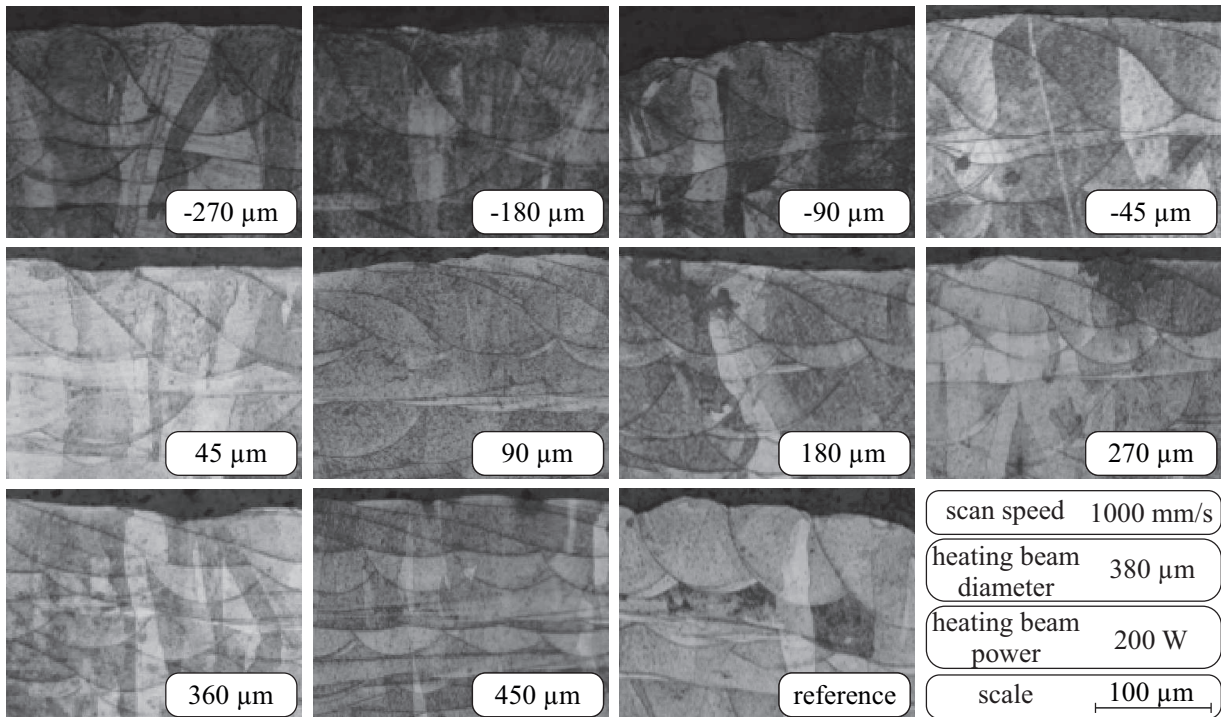


Figure 6.9: Etched cross sections of offset strategy samples manufactured with different offsets. Negative offsets are considered preheating, positive ones postheating. The bottom right image shows the reference sample's cross section.

scan speed of 1750 mm/s . At such high scan speeds a single beam with 200 W struggles to form a proper melt pool because the remelting of the previous layer is very low. Hence, the melt pools tend to ball, forming spherical melt pools with an insufficient interconnection to neighboring tracks or the previous layer. This commonly results in low density values. While at small offsets the additional heat input is large enough so that small but sufficiently large melt pools are formed, at high offsets the bumpy surface is remolten so that still a smooth surface is generated, although the remelting depth is very low.

Thereby, large postheating offsets offer the chance to work with low remelting depths, while achieving a smooth surface which in an ideal process would result in a productive process with high quality. But due to the low remelting depth these parameter sets are susceptible to defects that are induced by spatter particles or variations in the powder layer thickness because the power is far too low to allow a sufficient remelting of larger particles.

This is even more apparent when taking a look at the $450\text{ }\mu\text{m}$ offset at a scan speed of 2000 mm/s as shown in Fig. 6.12. It can be seen that the lower melt pool boundaries of some melt pools are not overlapping at all, but due to the remelting with the wide postheating beam the surface is smoothed and a sufficient overlap can be achieved.

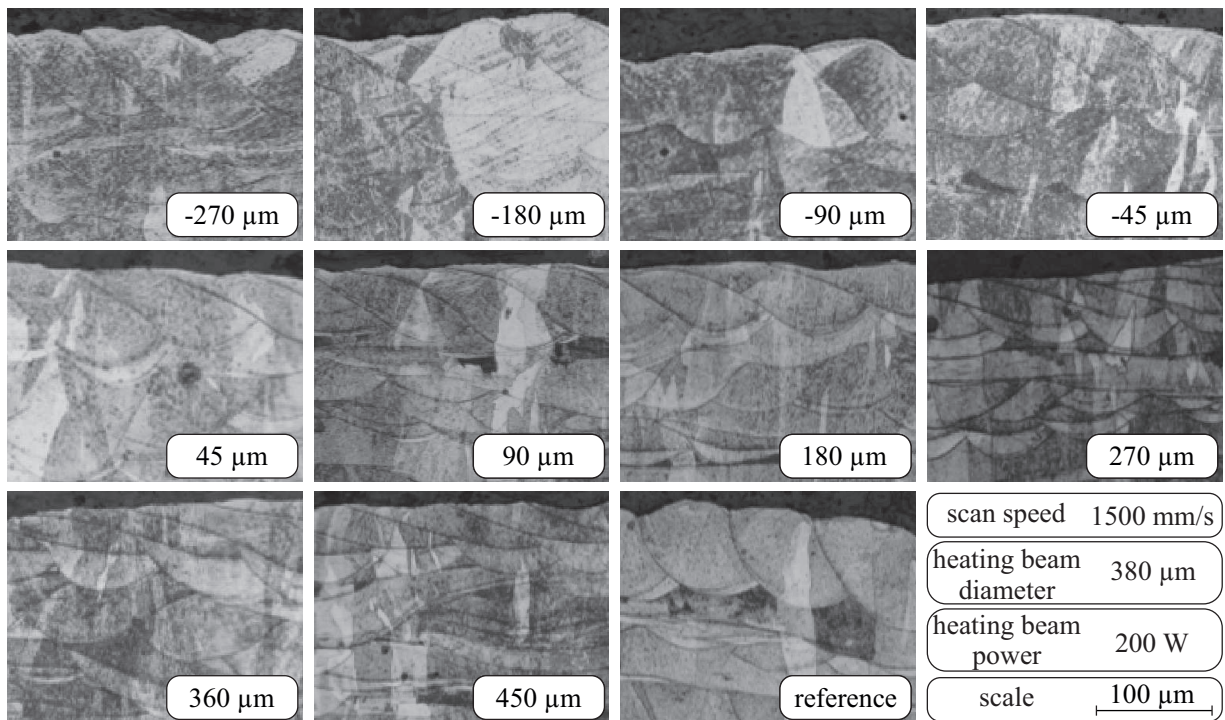


Figure 6.10: Etched cross sections of offset strategy samples manufactured with different offsets. Negative offsets are considered preheating, positive ones postheating. The bottom right image shows the reference sample's cross section.

Summarizing the influence of the different parameter sets it can be concluded that the influence of preheating on the melt pool shape can be neglected if not the effective energy density is much higher than it is in the reference sample. The melt pool dimensions are just slightly widened due to the change in initial temperature of the cross section before the melting beam reaches it. In contrast, postheating offers the chance to influence the melt pool shape, the solidification process as well as the surface quality in-situ.

Fig. 6.13 shows the relative density values in relation to the reference sample's relative density for the previously discussed cubic sample's. The dashed lines furthermore indicate the increase of density due to the use of the additional heating power in comparison to single-beam samples manufactured at the same speed with 200 W power.

The density curves support the previously discussed observations. In case of the far larger melt pool dimensions at low offsets of 1000 mm/s the density as well increases to a value higher than the reference sample's one. The increase on the postheating side is stronger, not only at that speed but for all the investigated ones, which supports the finding that postheating allows a stronger, beneficial influence on the melt pool dimensions and solidification. The trends are more significant in case of the higher heating beam diameter and power, as it can be seen when comparing the cross sections in Fig. 6.6 and Fig. 6.9.

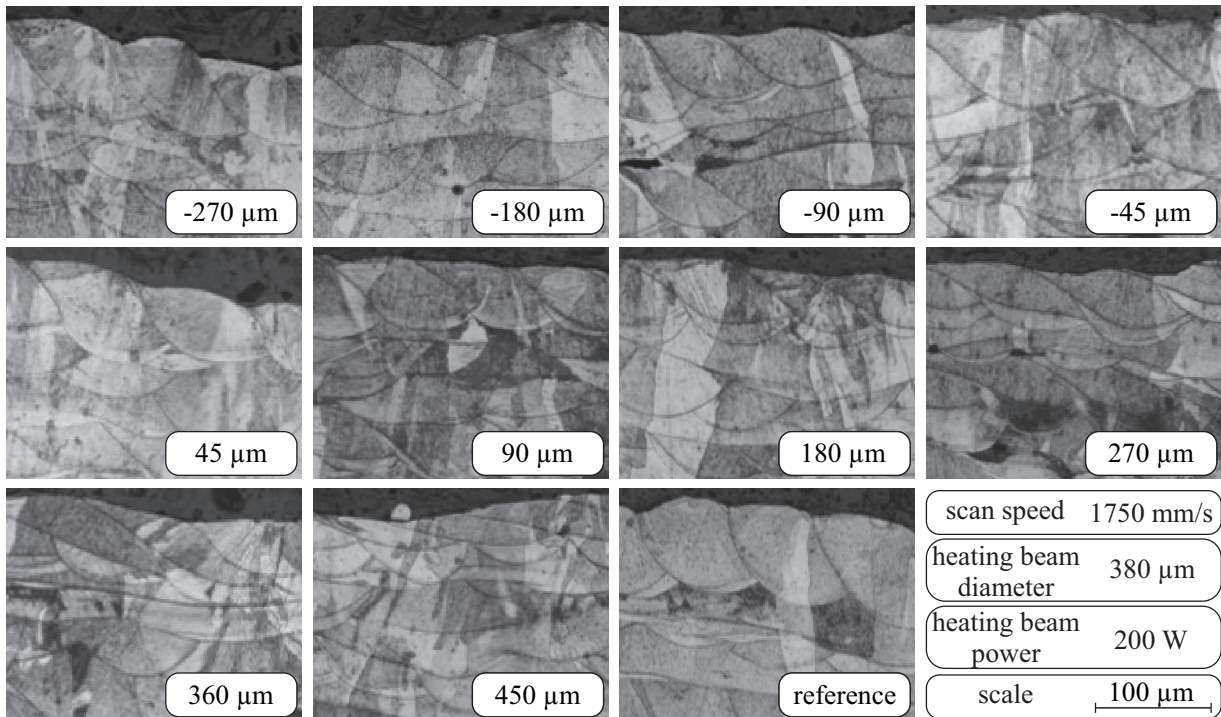


Figure 6.11: Etched cross sections of offset strategy samples manufactured with different offsets. Negative offsets are considered preheating, positive ones postheating. The bottom right image shows the reference sample's cross section.

In case of preheating as well as postheating the density values decrease with increasing beam offsets. It can be concluded that this happens due to the fact that the input power is distributed over a larger area so that the maximum intensity decreases which on the other hand results in smaller melt pool dimensions. Additionally, for large offsets there is a period of time in between both beams' passing in which no power at all is irradiated onto a certain cross section. The fall-off of density is commonly stronger for preheating offsets because those don't influence the solidification process as discussed earlier within this subsection.

The density values of the 2000 *mm/s* sample drop stronger than expected. Yet, it seems that the inherent spattering, which effect is increased due to the flawed shielding gas flow within the laboratory machine, cannot be compensated due to the very shallow melt pools. Still, the additional heating power that leads to an in-situ smoothing of the surface but does not influence the maximum melt pool depth results in an about 2% increase of density compared to the single-beam sample at the same speed without additional heating power.

In general it can be summarized that a higher overall power is beneficial for the density values at constant scan speeds because with a widened beam the risk for keyhole porosity can be neglected and thus the additional power results in larger melt pool dimensions,

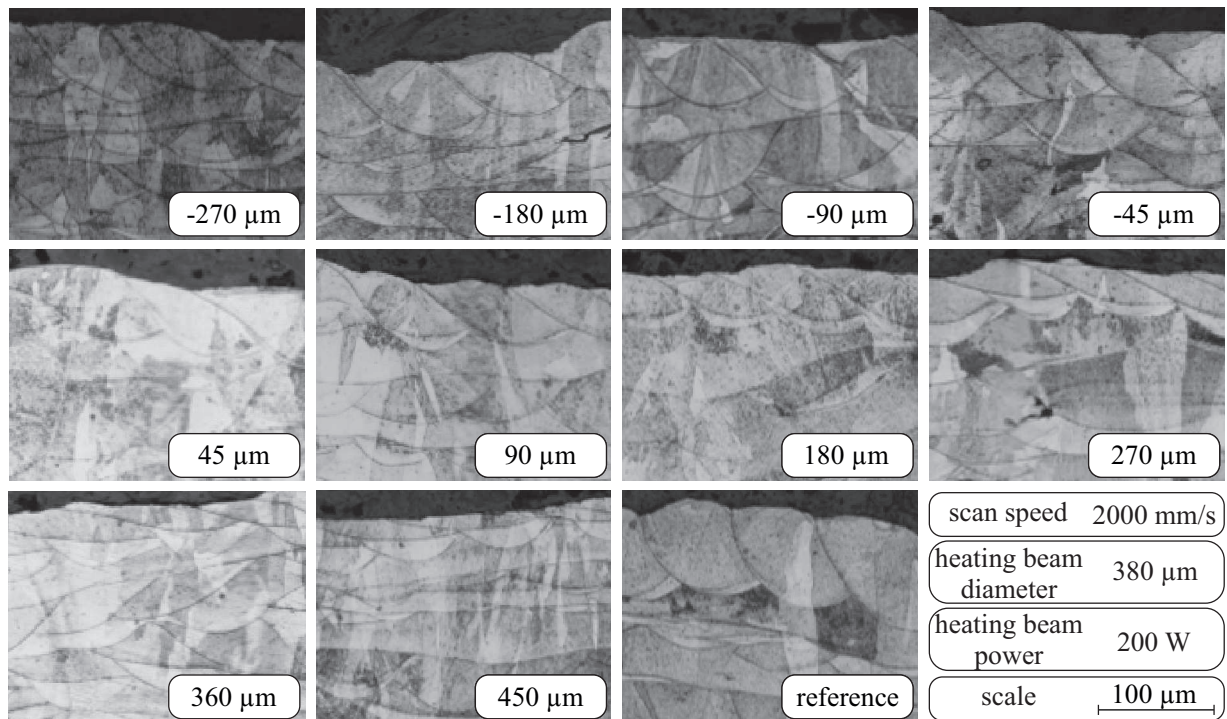


Figure 6.12: Etched cross sections of offset strategy samples manufactured with different offsets. Negative offsets are considered preheating, positive ones postheating. The bottom right image shows the reference sample's cross section.

a larger overlap and thereby a lower risk of lack of fusion errors. Yet, comparing single-beam and two-beam samples with the same energy density or even two-beam samples with different offsets won't work properly in regards to the part's density. In case of comparing single-beam with two-beam samples it has to be considered that the power within the widened heating beam is distributed over a far larger area. In case of two-beam parameter sets with different offsets the energy input is just distributed over a different time frame which results in changes of melting and solidification which are directly interlinked with the resulting melt pool dimensions.

Yet, it can be seen that the density values of preheating as well as postheating offsets of $45\ \mu\text{m}$ are commonly smaller than those for offsets of $90\ \mu\text{m}$ which is inconsistent to the general trend that lower offsets result in higher densities. The simulation does not show any noteworthy changes within the fluid dynamics due to this small change in offsets so that a harmful interaction of the heating beam with the vapor jet of the melting beam is the only remaining possibility to explain this effect, meaning that the effective heating beam power is reduced due to absorption within the vapor jet.

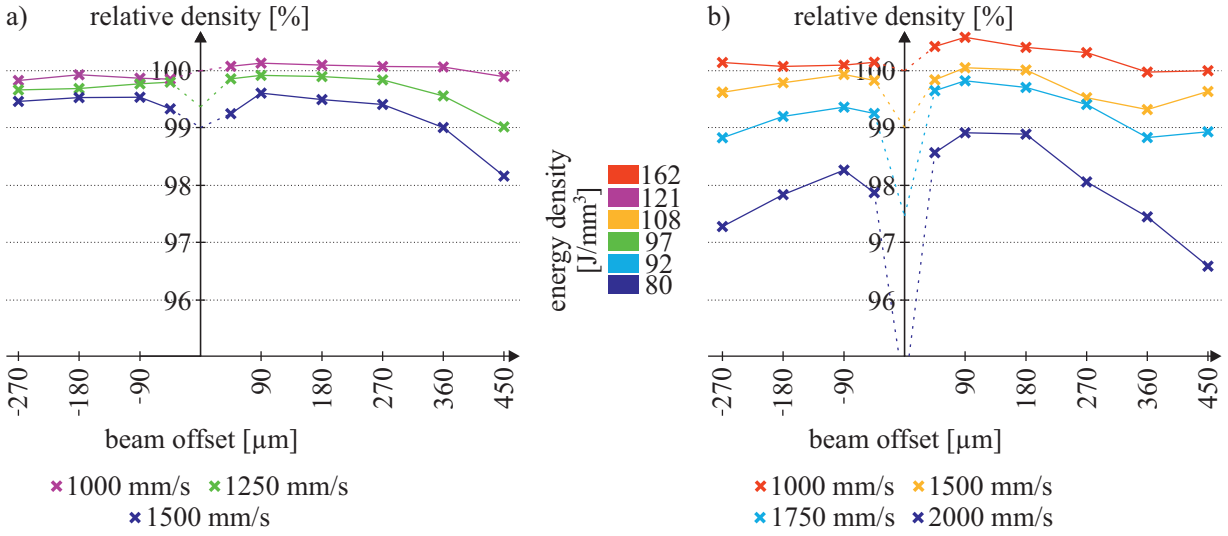


Figure 6.13: Measured relative density values of the samples manufactured by using offset strategies. The values are set in relation to the reference sample's density. Negative offsets indicate preheating, positive offsets postheating strategies. The dashed lines indicate the density increase compared to single-beam samples manufactured at the same speed with a power of 200 W , meaning that the additional heating power is missing. The graphs are divided into the sets of heating beam diameter and power with a) the samples manufactured with a heating beam diameter of $270\text{ }\mu\text{m}$ and 100 W power and b) $380\text{ }\mu\text{m}$ heating beam diameter and 200 W heating power.

6.2.3 Spatter Characteristics

As already seen in the proof of concept in subsection 6.2.1, the offset strategies seem to severely influence the spattering characteristics during the process. The relative spatter counts of the offset strategies are shown in Fig. 6.14. In this case a scan speed of 1250 mm/s hasn't been imaged when using the high speed camera. Yet, the other data points show similar trends and effects so that no lack of data to explain the occurring effects is apparent.

The figure shows that again the beneficial influence of the offset strategies is strongest when using the same scan speed as the reference sample and thereby maximizing the energy density. In these cases the amount of spatter particles decreases with increasing preheating offsets. As discussed in chapter 2, the major amount of spatter particles within the SLM process is originating from the powder bed and not the melt pool itself. These particles can be reduced effectively when using large preheating offsets because the heating beam melts and agglomerates small particles to larger particles which are less likely to be sucked in by the vapor jet due to their higher mass. Thereby, the overall amount of spatter is reduced.

In contrast, postheating offsets are severely increasing the spatter count. This effect increases with increasing postheating offsets. By taking a look into the high speed images it

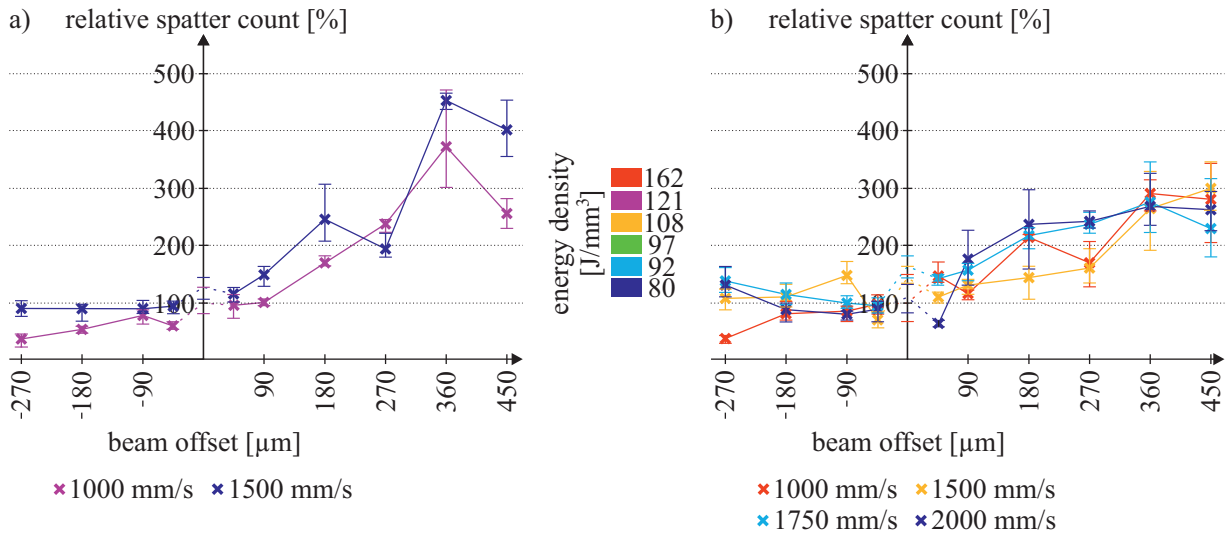


Figure 6.14: Mean, minimum and maximum of automatically counted spatter particles per millimeter of the offset samples relative to the reference sample. Negative offsets indicate preheating, positive offsets postheating strategies. The dashed lines indicate the spatter count of single-beam samples manufactured at the same speed with a power of 200 W. The graphs are divided into the sets of heating beam diameter and power with a) the samples manufactured with a heating beam diameter of $270 \mu\text{m}$ and 100 W power and b) $380 \mu\text{m}$ heating beam diameter and 200 W heating power.

can be observed that spatter particles that are forced backwards by the vapor plume are rapidly heated within the following heating beam. This does increase the detected amount of spatter due to a better visibility, but does not change the process' spatter count. Yet, rapid heating and possibly melting within the heating beam is increasing the risk for cold spatter particles to agglomerate to large particles which are increasing the risk for lack of fusion porosity. Furthermore, it can be observed that melt pool spatter is occasionally disintegrated by the heating beam, resulting in a higher number of small melt pool spatter particles. This obviously increases the spatter count as well but its influence on the process is uncertain due to the fact that the new spatter particles are smaller. Hence, it is not obvious whether the higher postheating spatter count is worse, equally bad or even beneficial. Since spatter particles are accelerated backwards with a certain opening angle, it can safely be assumed that this effect's extent is reduced with further increasing postheating offsets that have not been investigated at this point. A starting reduction can be observed when increasing the offset from $360 \mu\text{m}$ to $450 \mu\text{m}$ and the results of subsection 6.4.3 even show that at offsets as large as $700 \mu\text{m}$ this effect can be neglected.

To get a more complete picture of the influence of offset strategies on the spatter characteristics, Fig. 6.15 shows the portion of detected bright spatter within the spatter count. Thereby, more information about the kind of spatter can be deduced.

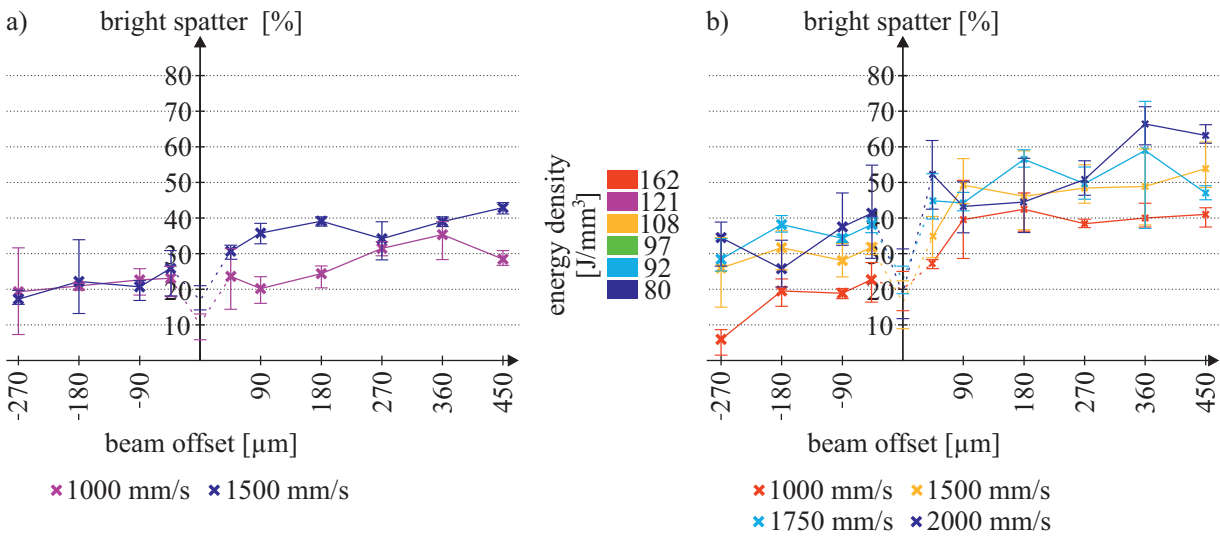


Figure 6.15: Mean, minimum and maximum relative amount of bright spatter particles within the automatically detected spatter count. Negative offsets indicate preheating, positive offsets postheating strategies. The dashed lines indicate the amount of bright particles within of single-beam samples manufactured at the same speed with a power of 200 W. The graphs are divided into the sets of heating beam diameter and power with a) the samples manufactured with a heating beam diameter of $270 \mu\text{m}$ and 100 W power and b) $380 \mu\text{m}$ heating beam diameter and 200 W heating power.

The figure shows that the amount of bright particles within the process is increased for mostly all offset strategy configurations and parameters. Just the high heating power preheating parameter sets at $1000 \text{ mm}/\text{s}$ are deviating from this overall trend. The generally higher amount of bright particles within the postheating strategies of both heating beam setups can easily be explained by the previously mentioned rapid heating of particles, that are sucked into the vapor jet, as well as the disintegration of larger particles that pass the the heating beam. In case of preheating, the heating beam heats up powder particles next to the track that is to be molten. Thereby powder particles that are ejected due to the vapor jet induced gas flows are hot, also if the particle is not traveling within the vapor jet but next to it. Thereby, particles that would have been categorized as cold powder spatter are transformed to hot powder spatter due to the heating beam. In case of the high power heating beam setup at $1000 \text{ mm}/\text{s}$, the melting by the heating beam is very intense so that a large melt pool is formed. Yet, the area of evaporation and the size of the vapor jet stay roughly constant. The large melt pool increases the distance of powder particles to the vapor jet so that the chance of particles being sucked into the jet is very low. Therefore, the major part of spatter particles in this configuration is sucked in the gas stream in the back of the melt pool so that no rapid heating within the laser or the vapor jet, which is less dense at this point, is present. This leads to the significant drop in bright particles compared to the reference sample or other preheating configurations.

Since the automatic data processing of the high speed images does not give any information on the spatter size, the high speed images have to be checked qualitatively to get to a final result on the large spatter count.

The images, depicted in Fig. 6.16, clearly show the increasing amount of spatter particles with increasing postheating offsets, while at preheating the amount of spatter is reduced. Naturally the spattering is not only driven by the parameter set but also by the material configuration, meaning the powder distribution in the layer which is currently being irradiated. Yet, the images have been chosen carefully to represent the spattering characteristics of these parameter sets as good as possible. It can be seen that at high postheating offsets the average spatter size is increased. Measuring single spatter particles shows that the largest spatter particles in these images are of a size of about $75\ \mu\text{m}$ in diameter. If a particle of this size drops onto a not yet irradiated layer, the necessary energy increases, possibly resulting in a small lack of fusion, but the size is too small to result in large pores. Yet, the trend of increasing spatter size and spatter count leads to the assumption that the risk for even larger particles is also increased, but the images do not show a reproducible way of particles that large being created, meaning that a random factor is part of it as well.

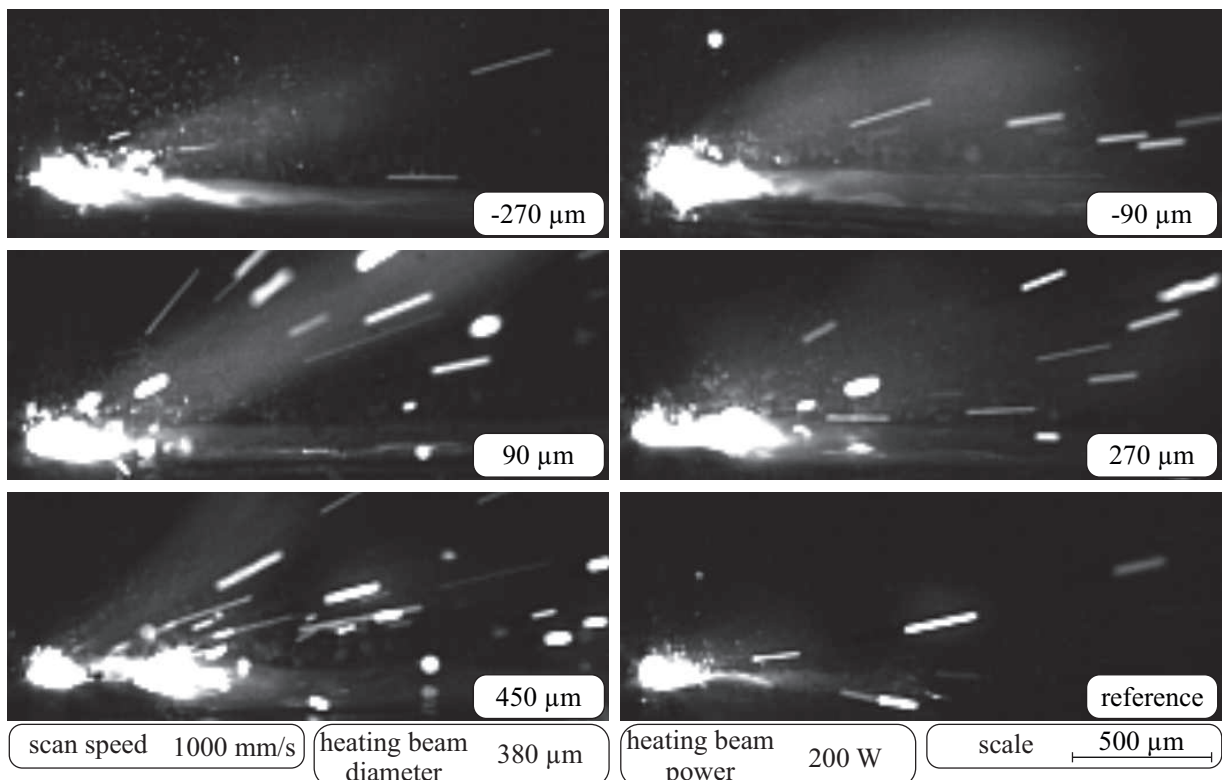


Figure 6.16: Single images of the high speed imaging, qualitatively showing the spatter characteristics when using a $380\ \mu\text{m}$ heating beam with $200\ \text{W}$ power at different offsets. The bottom right image shows a reference parameter set's high speed image.

6.2.4 Surface Roughness

The surface roughness has already been briefly described within the discussion of the etched cross sections. Fig. 6.17 shows the measured mean, minimum and maximum surface roughness of the offset samples in relation to the reference sample.

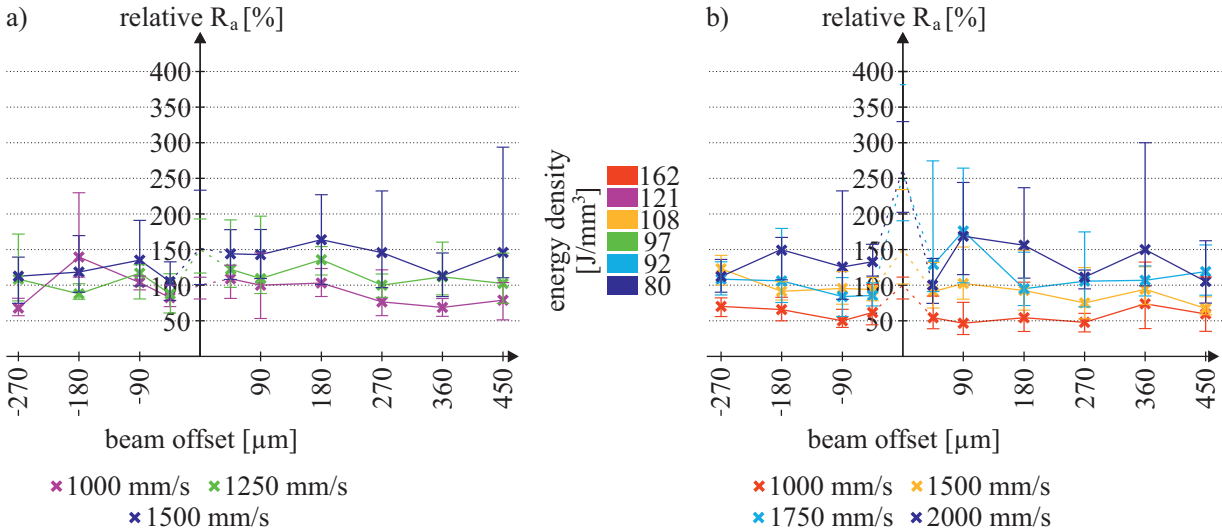


Figure 6.17: Mean, minimum and maximum of measured relative R_a values of the offset samples. The values are set in relation to the reference sample's filtered R_a value. Negative offsets indicate preheating, positive offsets postheating strategies. The dashed lines indicate the roughness decrease compared to single-beam samples manufactured at the same speed with a power of 200 W. The graphs are divided into the sets of heating beam diameter and power with a) the samples manufactured with a heating beam diameter of $270 \mu\text{m}$ and 100 W power and b) $380 \mu\text{m}$ heating beam diameter and 200 W heating power.

On first sight it is again obvious that the higher heating beam power results in a stronger influence. In case of the lower heating power of 100 W no overall trend is present. Only few benefits seem to be available for large offsets. Yet, the surface roughness of any sample is comparable to the one of a single-beam sample of the same scan speed. This leads to the conclusion that a heating power of 100 W is not sufficient when using a beam diameter of $270 \mu\text{m}$ to significantly smooth the overall surface structure of a sample.

In contrast, the $380 \mu\text{m}$, 200 W heating setup shows significant benefits and trends. Independent of the elaborated offset the surface roughness is decreased in comparison to a same speed single-beam sample. At all scan speeds the reduction can be as high as about 50%. When being compared to the reference sample the reduction of surface roughness is only present for scan speeds of 1000 mm/s . Yet, for all other scan speeds the reference sample's surface roughness is achievable when offset strategies are used.

The strong reduction of the surface roughness in comparison to the same speed single-beam samples, on one hand, has to be attributed to the smoothing over several tracks.

The smoothing is a result of very shallow remelting of the surface area of the previous melt tracks. Thereby the interconnection of the tracks is leveled and small prior errors can be corrected. On the other hand, the melt pool width is significantly increased by using the heating beam. Hence, the capillary forces result in a less curved melt pool surface due to a better wetting, which is already positively influencing the surface roughness before a smoothing by the next track is applied. Furthermore, the in-situ smoothing of balling melt pools, as discussed for fast scan speeds, is reducing the surface roughness effectively at high scan speeds.

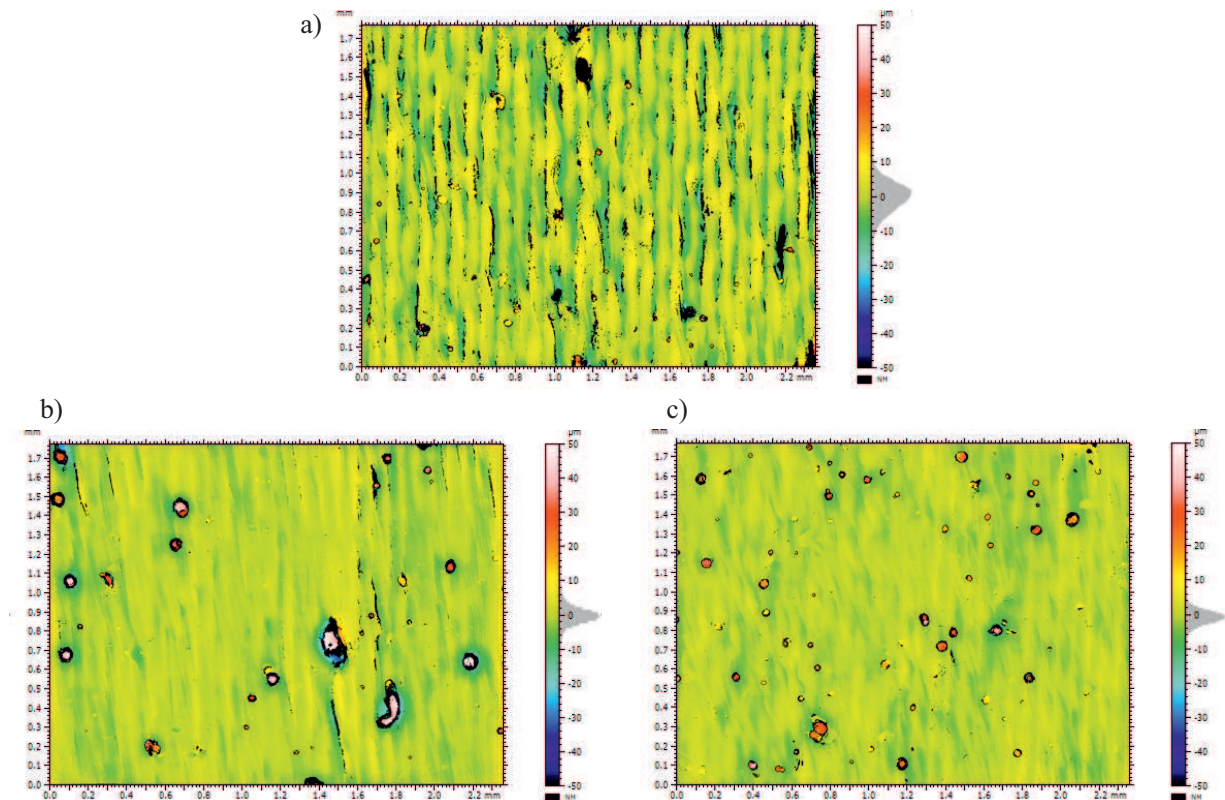


Figure 6.18: Surface topologies of a) the reference sample, b) at an offset of $45 \mu\text{m}$ and c) at an offset of $450 \mu\text{m}$. The scan speed is 1000 mm/s and the heating beam power is 200 W .

Fig. 6.18 shows the surfaces of the reference sample as well as those of a low offset of $45 \mu\text{m}$ and of a large one of $450 \mu\text{m}$ for 1000 mm/s at the high power heating beam setup.

The figure shows that clearly visible tracks in the reference sample are effectively smoothed by the heating beam. This can be seen by the more narrow height histogram on the sides of the surface topologies as well as in the amount of excluded points in between the tracks which are a result of high inclination angles that the microscope struggles to measure. When comparing the two two-beam samples' surfaces a difference is apparent. While at

the low offset the tracks are well visible, the lines blur out in case of the large offset. This is consistent with the previous observations that a small offset results in larger melt pools with a shape similar to single-beam samples. On the other hand, a large offset results in double melt pools, indicating a change in the solidification of the melt pool tail.

6.2.5 Influence on Deflection

The density of the samples is an important factor for the investigation of cantilever deflection because a high amount of porosity lowers the residual stresses as well as the sample's stiffness. Hence, the amount of parameters that are used to investigate the offset strategies' influence on deflection has to be reduced. Offsets of $\pm 90 \mu\text{m}$, $\pm 180 \mu\text{m}$ and $\pm 270 \mu\text{m}$ are chosen for all speeds except 2000 mm/s which is completely excluded from the deflection study. Hence, most of the parameter sets are guaranteeing a density of over 99.5 % of the reference sample's one so that a good comparability can be assumed. The values are shown in Fig. 6.19.

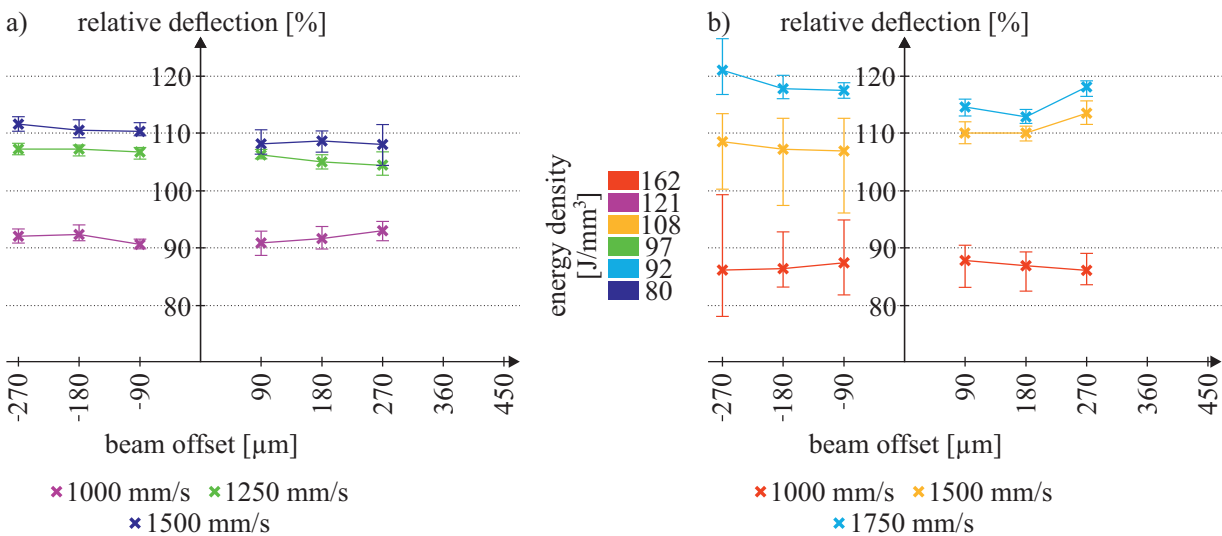


Figure 6.19: Mean, minimum and maximum of measured cantilever deflection of the offset samples. The values are set in relation to the reference sample's mean deflection. Negative offsets indicate preheating, positive offsets postheating strategies. The graphs are divided into the sets of heating beam diameter and power with a) the samples manufactured with a heating beam diameter of $270 \mu\text{m}$ and 100 W power and b) $380 \mu\text{m}$ heating beam diameter and 200 W heating power.

The values show no overall beneficial effect in regards to the deflection. Yet, in case of scan speeds of 1000 mm/s the additional heat allows a reduction of deflection by 10 % for the $270 \mu\text{m}$ heating beam setup and by about 15 % in case of the $380 \mu\text{m}$ setup. When using faster scan speeds the deflection values are all higher than the reference sample's

mean deflection. No overall trend in regards to the change of deflection with increasing offsets is apparent within the small range of offsets. The small variation between minimum and maximum of the deflection values in the $270\ \mu\text{m}$ setup is noteworthy. Tab. 6.2 gives a possible reason for the lack of beneficial influences on deflection at higher scan speeds. It shows the mean deflection values of the two-beam samples for speeds of $1250\ \text{mm/s}$, $1500\ \text{mm/s}$ and $1750\ \text{mm/s}$ as well as the values of single-beam samples manufactured at scan speeds of $500\ \text{mm/s}$, $750\ \text{mm/s}$ and $1000\ \text{mm/s}$. The listed values show a more or less

Table 6.2: List of deflection values in relation to the reference sample's deflection. Deflection values of $1000\ \text{mm/s}$ or less have been measured on single-beam cantilevers. At higher speeds the values of two-beam samples are listed.

scan speeds [mm/s]	500	750	1000	1250	1500	1750
relative deflection [%]	84.58	91.23	100	106.47	109.66	117.28

linear increase of deflection with scan speed independent of the used energy densities. Yet, when considering the $1000\ \text{mm/s}$ two-beam sample with $200\ \text{W}$ heating beam power that results in the same energy density as the $500\ \text{mm/s}$ single-beam sample, roughly the same deflection is observed. In case of faster scan speeds it is unclear whether the additional heat input is beneficial in comparison to same speed samples because those beams would result in low density parts with the available maximum laser power of $200\ \text{W}$. On the other hand, comparing the faster scan speeds to the samples with equally high energy density does not show the same similarity as it is available for the scan speed of $1000\ \text{mm/s}$ but rather higher deflection values for the two-beam samples. A conclusive answer to this effect is not available. It could be assumed that at faster scan speeds the interaction time of the heating beam is too low to beneficially influence the deflection of two-beam cantilevers. Furthermore, the melt pool shape of faster two-beam samples deviates more and more from the common single-beam shape of a half-spherical melt pool. The melt pools are defined by a low melt pool depth, which might be an indicator for higher thermal gradients along the build direction.

Summarizing this information, it seems like offset strategies can reduce the deflection as long as the resulting energy density is higher than the reference one, yet no larger reduction than a single-beam sample with the same energy density would achieve is possible. The influence of offset strategies for parameter sets that result in melt pool shapes that deviate from the common half-spherical shape is unknown because same speed reference samples result in too high porosity so that no comparability can be assumed.

Lateral offsets have not been investigated, although it is known from electron beam welding literature that using heating beams on the sides of the welding beam can reduce warping of metal sheets by reducing transversal stresses. Yet, the extent of this effect is expected to be far smaller in SLM. First, because of the higher speeds and smaller scales. Second, because

of the fact that a large amount of tracks are molten next to one another so that the stress fields are superimposed and third, due to the fact that the lateral preheating can only be done in an asymmetric way in SLM because of the powder bed on one side. Furthermore, the common understanding of residual stresses in SLM is that the longitudinal stresses are up to twice as high as the transversal stresses as shown by [32, 2].

6.2.6 Simulation-Based Investigations

While in the previous sections the experimental results have been discussed, this section will give more insight into the process based on the simulation tool. By that the presented theories are supported and discussed in more detail.

A distinct effect in postheating offset strategies are double melt pool boundaries which are expected to be a result of a stopped or even reversed solidification of the melt pool due to the irradiation by the heating beam. The simulation tool allows to extract the temperature curves for the different parameters which should indicate how the offsets are influencing the solidification process. Fig. 6.20 shows the temperature developments of four elements within the model that are positioned over one another and thereby show a z-resolved influence of the offset strategies on the temperature development. The elements are positioned in the center of the beam within a cross section that is irradiated by two beams in five different offsets.

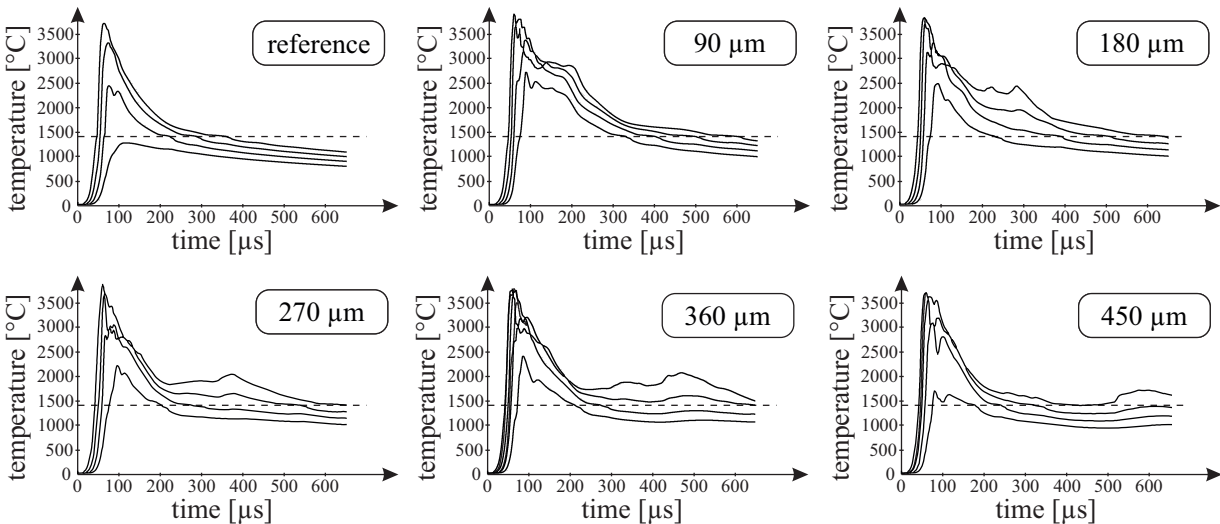


Figure 6.20: Simulated temperature development over time of five different offsets at a heating beam configuration of $270\ \mu\text{m}$ at $100\ \text{W}$ and a scan speed of $1000\ \text{mm/s}$. The lines show four selected elements that are at different z -positions within the center of a cross section that is irradiated. The dashed line indicates solidus temperature. The extracted curves belong to the z -positions of $15\ \mu\text{m}$, $25\ \mu\text{m}$, $35\ \mu\text{m}$ and $45\ \mu\text{m}$ into the previous layer.

The graphs show several interesting effects. First, when using the additional heating power, especially at an offset of $90\ \mu\text{m}$, apparently one more element is molten (surpassing the solidus line) which indicates a larger depth and thereby larger melt pool dimensions which is consistent with the density curves that show the highest density at offsets of $90\ \mu\text{m}$. Second, the distance between melting and heating beam is clearly visible within the temperature development. While at an offset of $90\ \mu\text{m}$ the curve only shows a small plateau at high temperatures in the cool down phase, higher offsets show moments in the cool down phase at which the temperature rises again due to the heating beam. With increasing offsets the distance between the first temperature peak due to the melting beam and the following bump due to the heating beam increases. With increasing distance the temperature at which the second temperature rise occurs decreases.

To support the theory of a stopping or reversed solidification one has to take the temperature around solidus and liquidus temperature into account. At offsets of $90\ \mu\text{m}$ and $180\ \mu\text{m}$ no change of the cool down is present in the range of the solidification of the material. The increase of temperature is restricted to elements which are in the molten state so that no second melt pool boundary is formed but rather the melt pool dimensions are increased. In the case of an offset of $270\ \mu\text{m}$ the strongest second temperature rise happens within the melt as well but in lower levels the temperature is kept constant for about the time that the heating beam needs to pass by ($270\ \mu\text{s}$ in this parameter set). Due to the constant temperature somewhere in between, the solidification needs to stop resulting in a chance that double melt pool boundaries are generated. This is in agreement with double melt pool boundaries that are present for some melt pools within the experimental samples of this parameter set. When investigating the curves of $360\ \mu\text{m}$ and $450\ \mu\text{m}$ offset one can see that the curves are rising over solidus temperature two times. First, the material is molten by the melting beam, then solidifies unto a certain depth and is then remolten by the heating beam before it finally solidifies. When considering that the curves are representing different z-levels within the model, the curves indicate that the remelting of the material starts at a lower level for an offset of $360\ \mu\text{m}$ as it does at $450\ \mu\text{m}$ offset. These details within the simulated temperature developments perfectly explain why the double melt pool boundaries are only present for higher offsets and why the distance between lower and upper melt pool boundary increases with increasing offsets.

In Fig. 6.21 the evolution of the $450\ \mu\text{m}$ offset sample is shown based on simulated cross sections at different time steps. It as well shows the distinct steps that lead to the double melt pool boundaries. First, the maximum depth of the melt pool is reached due to the irradiation of the cross section by the melt pool. The maximum depth is at $50\ \mu\text{m}$ within the previous layer. After the melting beam passed by the melt pool starts solidifying. The solidification is stopped at about a depth of $15\ \mu\text{m}$ within the previous layer and reversed

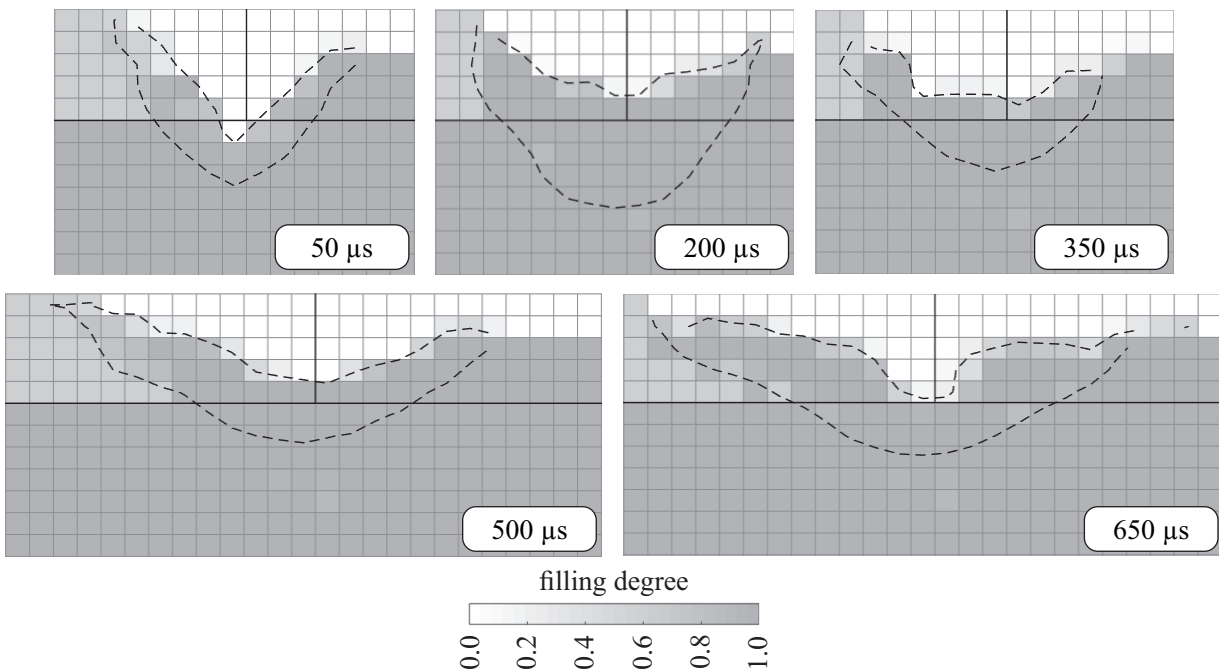


Figure 6.21: Simulated evolution of a melt pool with double melt pool boundaries in a cross section. A heating beam with $270\ \mu\text{m}$ diameter and $100\ \text{W}$ power is used at a speed of $1000\ \text{mm/s}$ and an offset of $450\ \mu\text{m}$. The mesh size is $10\ \mu\text{m}$. The dashed lines indicate the current melt pool shape at the given time step, thus showing the first and second melt pool boundary. The times are in agreement with the ones of the temperature curves.

unto a depth of about $25\ \mu\text{m}$. During the irradiation by the heating beam that reverses the solidification process within the previous layer the upper melt pool width significantly increases because of the larger beam diameter. After reaching the maximum dimensions the melt pool finally solidifies.

Fig. 6.22 shows a comparison of an experimentally achieved cross section and the simulated one each for the side of the previous track, since this side is not overlapped by the next

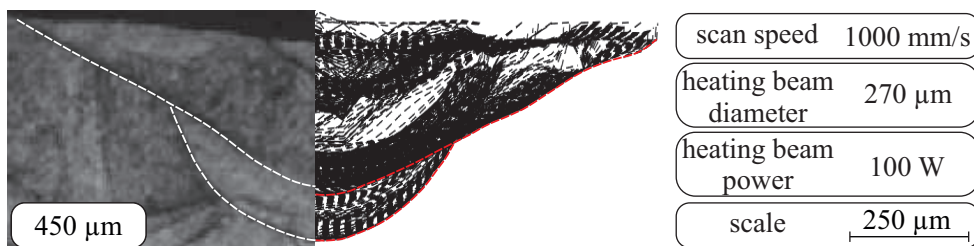


Figure 6.22: Comparison between the simulated melt pool dimensions and an experimental cross section for the given parameter set. The simulated melt pool boundaries are accumulated for the previous track side. The dashed red lines indicates the maximum melt pool dimension as well as the second melt pool boundary at the maximum extent of remelting. The sample's cross section is shown on the left. Lower and upper melt pool boundary are indicated by the white dashed line.

track. The depicted melt pool is still the one of a 1000 mm/s sample with a heating beam diameter of $270\text{ }\mu\text{m}$ and 100 W power which is moving at a postheating offset of $450\text{ }\mu\text{m}$.

The figure shows a good agreement between experiment and simulation and offers a higher certainty that the investigations done on the basis of the temperature development are correct because the finally achieved melt pool size and shape are similar.

When taking a look into the $380\text{ }\mu\text{m}$ heating beam diameter samples, the simulation offers the same possibilities to explain the generation of a second melt pool boundary. When considering that the key driver for this effect is that the additional energy is not used to enlarge the maximum melt pool size but to stop solidification, one can estimate the start of double melt pool boundaries by simply having a look at the simulated melt pool depths as listed in Tab. 6.3. When the depth of the two-beam postheating strategy is not

Table 6.3: List of simulated melt pool depth values, relative to the same speed melt pool depths. If the melt pool size is not increased for the postheating offsets in comparison to the single beam same speed sample, a chance for double melt pool boundaries can be expected.

	$45\text{ }\mu\text{m}$	$90\text{ }\mu\text{m}$	$180\text{ }\mu\text{m}$	$270\text{ }\mu\text{m}$	$360\text{ }\mu\text{m}$	$450\text{ }\mu\text{m}$
1000 mm/s	1.24	1.20	1.09	0.99	1.02	0.99
1500 mm/s	1.14	1.11	1.05	0.98	0.98	0.98
1750 mm/s	1.11	1.08	1.05	1.01	1.03	1.02
2000 mm/s	1.11	1.04	1.01	1.00	0.99	0.99

significantly larger than the same speed single-beam sample, the additional power is not expected to increase the maximum melt pool depth. In these cases the listed value is about 1.00. In these cases the additional power has to result in other changes, opening the chance to assume that at those offsets double melt pool boundaries occur. When comparing the offsets at which the simulation indicates double melt pool boundaries, which here are at about $180\text{ }\mu\text{m}$ to $270\text{ }\mu\text{m}$, to the previously showed experimental cross sections a good agreement can be observed.

6.3 Wobble Strategy

6.3.1 Experimental Planning

By using the wobble strategy the effective speed of the heating beam is significantly higher than the scan speed of the melting beam due to the circular movement of the heating beam. Furthermore, the area which is irradiated by the heating beam within a single track is much larger. Due to the higher circumferential speed as well as the larger area

which is affected, all wobbling parameter sets are investigated for the higher power heating beam setup of 200 W power and 380 μm beam diameter. Additionally, it is assumed that the melt pool size is less significantly influenced than it is by offset strategies. Hence, the influence on the density should be lower as well. Therefore, the scan speed of 2000 mm/s is neglected since it already resulted in not sufficiently dense samples within the investigation of offset strategies. This means that only the scan speeds of 1000 mm/s , 1500 mm/s and 1750 mm/s are used for wobbling samples.

The wobbling parameter sets are defined by the wobbling diameter and the distance of repetition after which the circular movement is repeated. The wobbling diameters that are investigated are either 250 μm , 500 μm or 750 μm wide. The repetition distances are set to either 1/2 or 1/3 of the elaborated wobbling diameter. This theoretically results in circumferential speeds of the heating beam of either 2π or 3π times the melting beam's scan speed. Yet, there are some drawbacks when using too high circumferential scan speed as shown in the following section.

Since a small offset is necessary to allow the controls to reliably turn on and off both laser beams, the center of the circular motion is set to 45 μm behind the melting beam's center point. All samples are again manufactured with a hatch distance of 82.5 μm and a layer thickness of 30 μm as well as a melting beam with a diameter of 90 μm and a power of 200 W. Because of the large wobbling diameters no simulation is conducted to support the experimental investigations. Yet, it can be assumed that simulation-based knowledge of the offset strategies can be transferred to explain certain effects that are occurring when using wobbling strategies.

6.3.2 Microstructure and Density

The cross sections of the wobble strategy samples show very distinct features when being compared to the reference sample or even the offset strategy samples. Fig. 6.23 shows the first set of wobble strategy samples which have been manufactured at a scan speed of 1000 mm/s . As discussed before, the distance after which the wobbling movement repeats itself is set to a half or a third of the wobbling diameter.

In general the micrographs show comparable maximum melt pool depths for all parameter sets as well as the reference sample's one. Only the upper melt pool region is significantly widened due to the wobbling heating beam. This results in double melt pool boundaries as well as a smoothed surface as it is the case for postheating strategies with high offsets. Yet, the second melt pools are much more shallow than the ones seen within the offset strategies. Furthermore, the second melt pool boundary does not origin within the same track as it

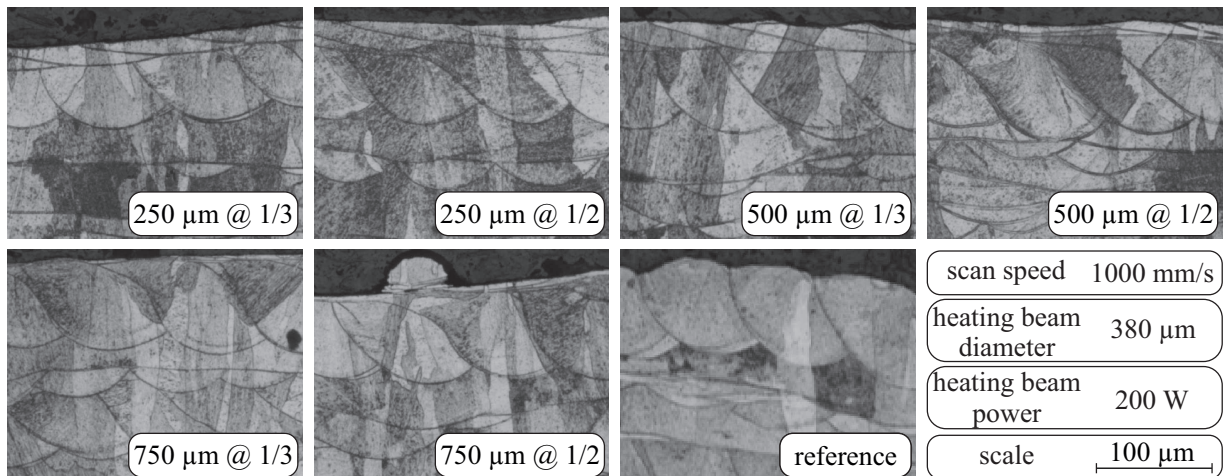


Figure 6.23: Etched cross sections of wobble strategy samples manufactured with different wobbling diameters and repetition distances. 1/2 indicates that the distance of repetition equals a half of the wobbling diameter.

can be seen for a $250\ \mu\text{m}$ wobbling diameter and a repetition distance of $125\ \mu\text{m}$. It shows that in this case the second melt pool boundary is formed by the second next track. This distance increases for increasing wobbling diameters, since the remelting of the surface by the heating beam is the reason for these second melt pool boundaries. The remelting depth of the wobbling beam reduces with increasing wobbling diameters. This is due to the increasing area over which the heating beam is inducing the its power. Furthermore, the circumferential speed increases with decreasing repetition distances. Yet, the remelting depth at a wobbling diameter of $500\ \mu\text{m}$ is larger for the sample with a smaller repetition rate which thereby is in contrast to the theory of decreasing interaction time. By having a look into the high speed images of the two $500\ \mu\text{m}$ wobbling diameter parameter sets the reason is obvious as depicted in Fig. 6.24.

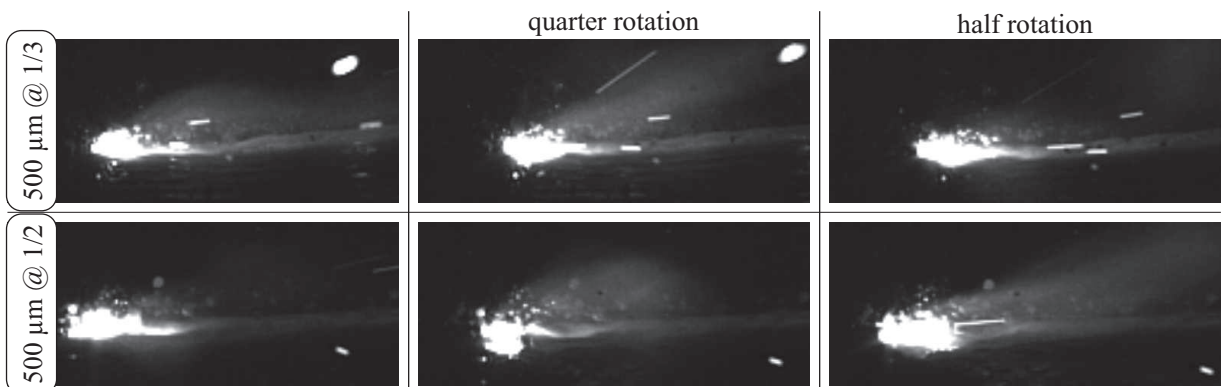


Figure 6.24: Comparison of the high speed images of wobble strategy parameter sets at a wobbling diameter of $500\ \mu\text{m}$ and a linear scan speed of $1000\ \text{mm/s}$. The desired path is illustrated in Fig. 5.3.

The comparison of the two sequences of high speed images shows that the reason for the contradictory behavior has to be attributed to the machine's control system and scan heads. The images clearly show that the wobbling diameter of the smaller repetition distance sample is not as high as it is set, presumably because the resulting circumferential speed would be too high for this wobbling diameter. Thereby, the scan head mirrors are not moving on the desired path. Hence, the effective wobbling diameter is smaller than the set value. This results in an effectively lower circumferential speed as well as a stronger focusing of the heat around the melt pool and thus larger remelting depth.

The $750\ \mu\text{m}$ wobbling diameter cross section shows another error that can be induced to the sample by the wobble strategy. Due to the high overlap of the heating beam with previous tracks a risk of melting particles to previous tracks is introduced. Yet, due to the short interaction times the size of possibly molten particles is comparably small so that it is unclear whether this increases the risk for lack of fusion errors or if it can be neglected due to the remelting by the next layer.

The cross sections of samples that are manufactured at a melting beam scan speed of $1500\ \text{mm/s}$ are shown in Fig. 6.25. As these images show, the error in wobbling diameters can be observed more often for higher linear scan speeds.

The cross section of the $500\ \mu\text{m}$ wobbling sample with a repetition distance of a third of the wobbling diameter shows that the melt pool is just reaching to the second next track. This means that the effective wobbling diameter is only about $330\ \mu\text{m}$. The high speed images show that at this speed the error in wobbling diameter is as well present for the $500\ \mu\text{m}$ wobbling diameter with a repetition distance of $250\ \mu\text{m}$ and the parameter set

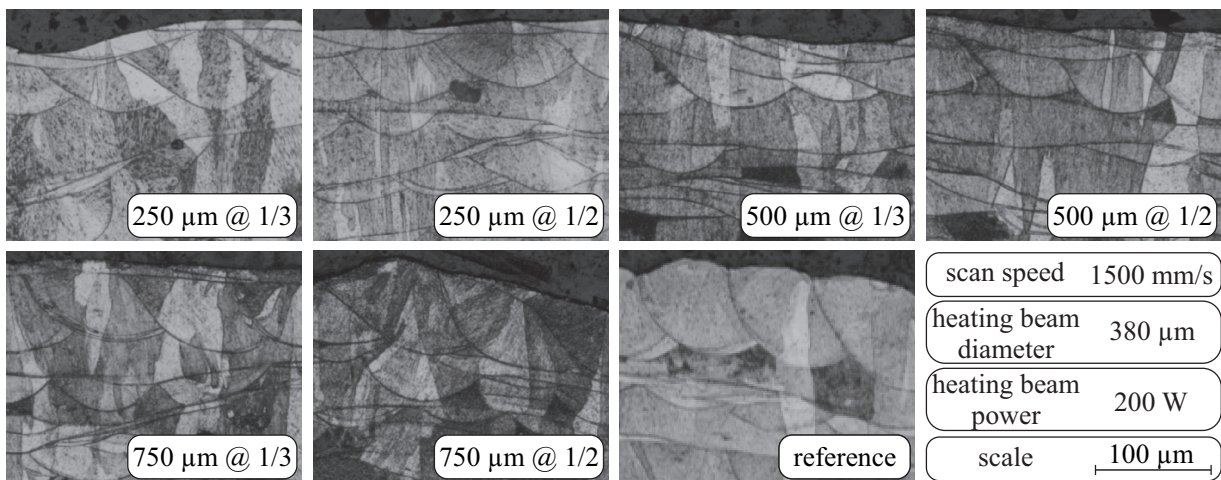


Figure 6.25: Etched cross sections of wobble strategy samples manufactured with different wobbling diameters and repetition distances. 1/2 indicates that the distance of repetition equals a half of the wobbling diameter.

of $750\ \mu\text{m}$ wobbling diameter and a repetition distance of $250\ \mu\text{m}$. In contrast the other parameter set at $750\ \mu\text{m}$ diameter does not show a wrong wobbling diameter within the high speed images. This explains why the latter one again results in lower remelting depth or even none at all. The lack of remelting is also visible within the high speed images for this parameter set, just powder particles are agglomerated to larger melt droplets on the powder bed side.

Fig. 6.26 completes the set of investigated wobble parameters by showing the cross sections of samples manufactured at a melting beam scan speed of $1750\ \text{mm/s}$. These images show roughly the same effects like the ones at slower scan speeds but the effects are more irregular and less reproducible than the previously shown results. This is assumed to be the result of an again increasing scan speed. The higher scan speed results as well in smaller basic melt pools. Yet, no balling behavior of the melt pools can be observed, meaning that the remelting within the wobble strategy is as well smoothing the surface sufficiently to suppress this effect. At small wobbling diameters the additional heat within the melt pool vicinity which results in effectively larger melt pools is additionally reducing the risk for balling so that no smoothing is necessary. A look into the high speed images shows the same error in wobbling diameters which are present for a scan speed of $1500\ \text{mm/s}$.

These control errors or simply too slow scan head mirrors are overall messing up the usability of the wobble strategy, meaning that only a small band of previously investigated parameter sets can be used because it is not guaranteed that the desired parameters are actually used to manufacture the part. Yet, the other criteria are investigated as usual but one has to keep these uncertainties in mind.

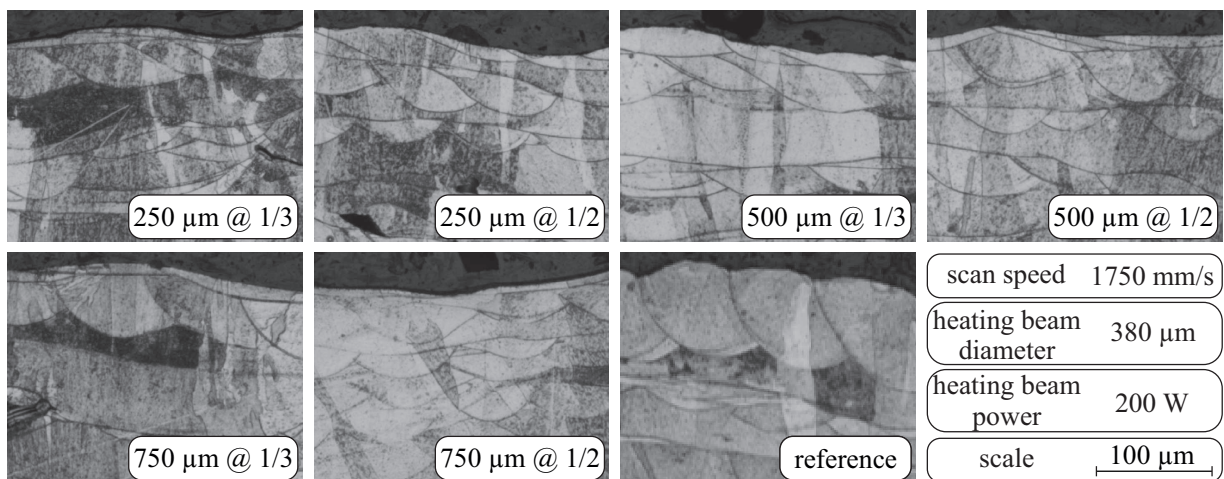


Figure 6.26: Etched cross sections of wobble strategy samples manufactured with different wobbling diameters and repetition distances. 1/2 indicates that the distance of repetition equals half of the wobbling diameter.

The next criterion to be investigated is the density which is a result of the discussed microstructure. The measured values are as usual set in relation to the reference sample's density and depicted in Fig. 6.27

Taking a look at the 1000 mm/s samples first, it can be seen that the wobble strategy parameters are behaving as the offset strategy parameter sets do. The values of small wobbling diameters are comparable to those of small postheating offsets, while large wobbling diameter parameter sets are similar to those of large postheating offsets at the same scan speed. This can be attributed to the fact, that at a scan speed of 1000 mm/s , which is equal to the reference sample's scan speed, the overall effect on the density is small since the microstructure is already dense because of the melting beam and no further heating power is required.

The present effects become more obvious when taking the higher scan speeds into account. At those speeds a strong drop for large wobbling diameters is apparent. With a $500\text{ }\mu\text{m}$ diameter and the smaller repetition rate the density is as high as it is for a wobbling diameter of $250\text{ }\mu\text{m}$. This can be attributed to the diameter error which has been discussed previously. Higher wobbling diameters result in lower densities since the power is distributed over a wider area. The density as well decreases with increasing repetition distances due to the error in wobbling diameters. When using higher distances the error is less distinct and thereby the actually present wobbling diameter is larger.

The values even drop to densities lower than the same speed sample's ones which indicates that the strategy is inducing additional errors when using certain parameter sets. This is

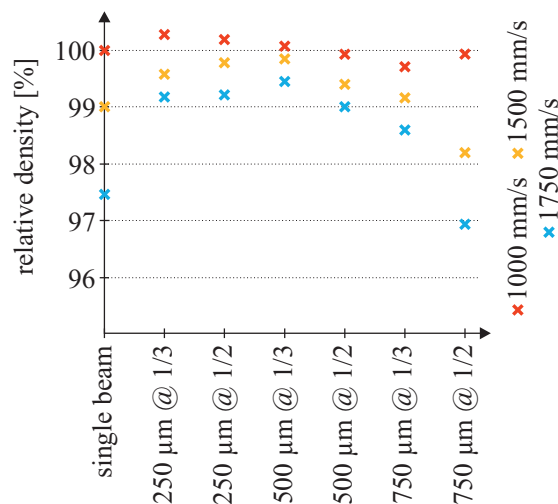


Figure 6.27: Measured density values of the wobble strategy samples in relation to the reference samples mean density value. Density values of same speed single-beam samples with an overall power of 200 W are shown as well.

the case for the highest resulting wobbling diameter. At this parameter set the heating beam agglomerates powder particles to large droplets which then are irradiated in the second next track or even later. Hence, the droplets can cool down and remain as large particles on the powder bed, thus increasing the risk for lack of fusion.

6.3.3 Spatter Characteristics

The deviation of the wobbling diameter from the desired values is an issue when evaluating trends within the available data. Fig. 6.28 shows the spatter counts for the different wobbling parameter sets. The values show no clear trends, yet commonly stay below the

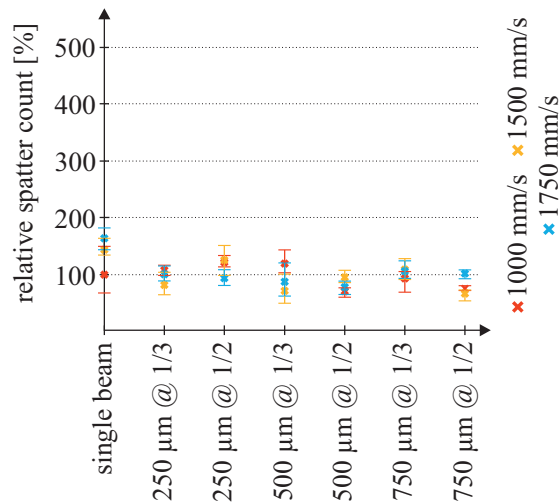


Figure 6.28: Automatically counted spatter particles per millimeter in relation to the reference sample's spatter count. Spatter count values of same speed single-beam samples with an overall power of 200 W are shown as well.

same speed single-beam samples' values. When having a look at the 1000 mm/s parameter sets which are the ones with the lowest probability for errors in the wobbling diameter, a trend for decreasing spatter counts with increasing wobbling diameter is apparent. Taking the high speed images into account the trend is obviously due to the larger area in which the heating beam is melting small powder particles so that larger droplets form. These droplets are less likely to be blown away by the vapor jet induced gas stream because of the higher mass. The difference in the general behavior is depicted in Fig. 6.29 which clearly shows the difference in droplet formation on the powder bed side.

The smaller melt droplets that are generated when using a 500 μm wobbling diameter and a 250 μm distance of repetition commonly drop into the melt pool like other powder particles which is why the amount of small droplets is smaller than the one of large droplets which are generated in case of the larger wobbling diameter.

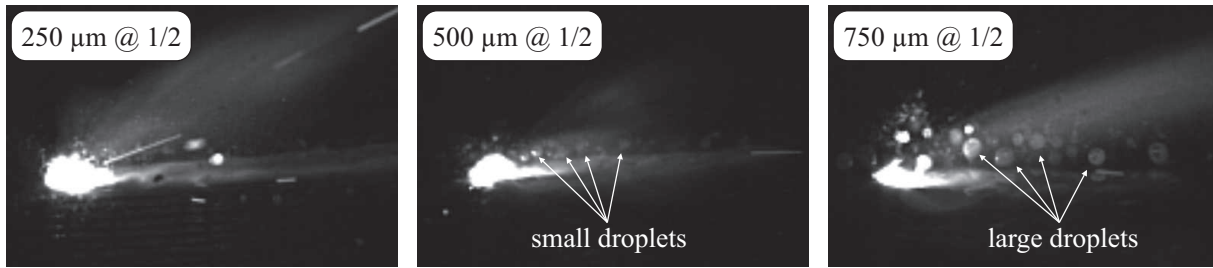


Figure 6.29: High speed images of different wobbling parameter sets at a scan speed of 1000 mm/s showing the different behavior in droplet formation because of the heating beam's melting of powder particles.

At higher scan speeds this trend is not as obvious. First, because of the discussed errors in the controls and scan heads and second because of the increasing circumferential speed of the heating beam which decreases the interaction time of the beam with the powder bed and thereby reduces the probability and amount of particles being fused to larger melt droplets. Yet, the minimum spatter counts at those speeds are even lower than the ones which can be achieved with preheating strategies. When comparing the low wobbling diameters to the offset strategies one can see that the spatter characteristics are comparable to low offsets which makes sense due to the error in the diameter which effectively reduces it even further and results in very little movement within the direct vicinity of the melting beam. Still, the large wobbling diameter samples show significantly less spatter particles than the same speed offset parameter sets due to droplet formation on the powder bed side.

These results support the findings of the offset parameter sets that slightly melting particles of the powder bed side that would not be molten by the melting beam in the current track is lowering the overall spatter count because larger, heavier particles are less likely to be blown away. Yet again, large particles that are especially created by large wobbling diameters increase the risk for lack of fusion porosity if these solidify or are blown away and drop down on a layer which is yet to be irradiated. Still, as long as the particles are not blown away the cool down is very slow due to the quasi-insulation of the powder bed so that the melt droplets commonly get absorbed into the melt pool by capillary forces as soon as they get into contact with the melt pool.

6.3.4 Surface Roughness

The surface roughness in wobble strategies is driven by the remelting of previous tracks by the circulating heating beam which reaches, depending on the chosen wobbling diameter, over several previous layers. Fig. 6.30 shows the measured mean, minimum and maximum roughness values in relation to the reference sample's mean roughness.

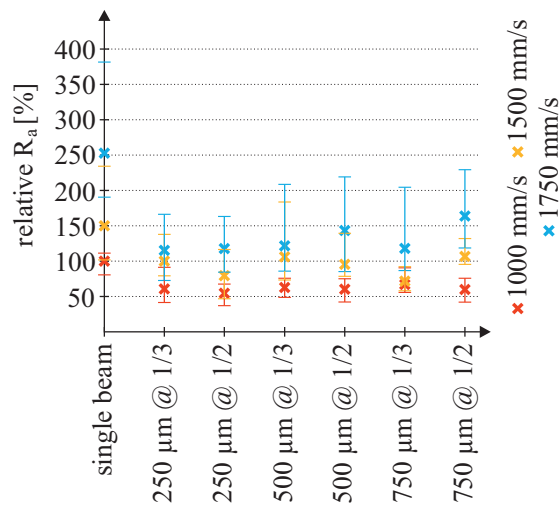


Figure 6.30: Mean, minimum and maximum of measured relative R_a values of the wobble strategy samples. The values are set in relation to the reference sample's filtered R_a value. Relative R_a values of same speed single-beam samples with an overall power of 200 W are shown as well.

The graphs show very promising effects of the wobble strategy on the surface roughness with overall surface roughness reductions by about 50% in comparison to the same speed single-beam samples and thereby about the same in comparison to the reference sample when using a wobbling parameter set with a scan speed of 1000 mm/s. Hence, the values are comparable to the one of offset strategies with large postheating offsets. This is not surprising since at large postheating offsets a similar in-situ remelting effect is present.

Yet, the wobble strategies show an interesting new effect. Because of the circular movement of the heating beam, fish scale structures are generated in case of some parameter sets on the samples' top surfaces. Depending on the used parameter sets for wobbling diameter and distance of repetition the appearance of the fish scale structures change. The fish scale structures are best visible for the highest grade of remelting, meaning the slowest investigated scan speed. Some of these structures are depicted in Fig. 6.31.

The fish scale structures are best visible by light microscopy because of the well visible melt pool boundaries. The effect on the surface roughness is very little which is why these structures are hard to see within the surface topology images and do not result in increased surface roughness. Currently there is no known use of these structures within the SLM process except a possibly esthetic one. Yet, therefore all other surface influencing factors would have to be excluded which cannot be guaranteed with the current process technology.

The structures also show the diameter error for repetition distances of a third wobbling diameter. In these cases the structure is similar to the one of the next smaller wobbling diameter with a repetition distance of a half wobbling diameter.

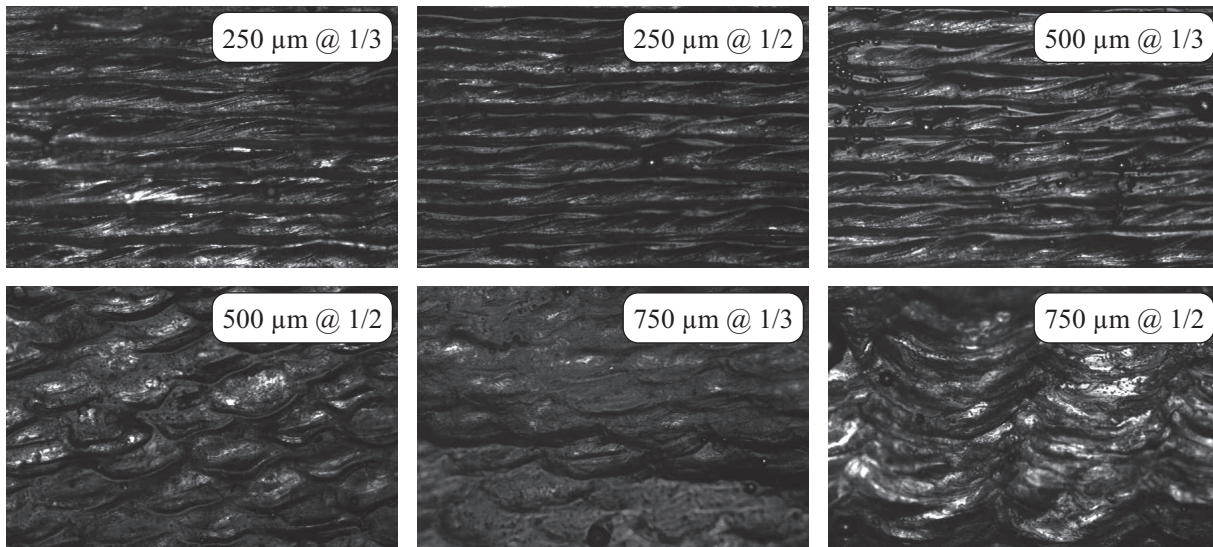


Figure 6.31: Surface images of samples manufactured with a scan speed of 1000 mm/s . In case of some parameter sets fish scale structures are generated by wobble strategies on the top surfaces of the samples due to severe remelting of previous tracks.

6.3.5 Influence on Deflection

The investigation of the offset strategies' influence on deflection showed that when keeping the movement of the melting beam similar to the reference sample's one the influence is mostly dependent on the scan speed and not on the offset parameters. To check whether this is as well the case for the wobble strategies the samples with a relative density of 99.5% of the reference samples density are investigated. In contrast to the offset strategy samples the wobble strategy cantilevers have just been built once. Yet, due to the fact that the standard deviations of the previously investigated cantilever samples are quite low, no problem is assumed to occur due to that. The measured results of the ten parameter sets are shown in Fig. 6.32.

At the first three data points of the 1000 mm/s samples the measured deflection is similar to the one measured for the offset strategy of the same scan speed, meaning about 15% less than the reference sample's deflection. At larger wobbling diameters the deflection is close to the one of the reference sample, which suggests that the deflection is decreased most if the beams are close to one another and thereby the depth which is influenced by a higher temperature is maximized. In contrast, heating the surface area does not seem to change anything. The faster scan speed cantilevers are as well comparable to the offset samples that were manufactured at the same speed which is thereby supporting the findings discussed within the offset strategy's section.

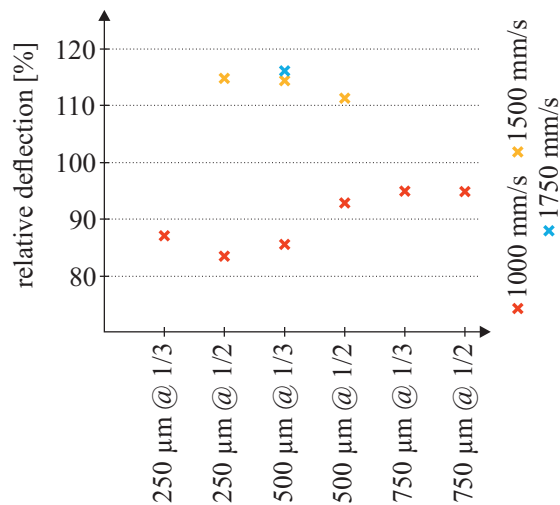


Figure 6.32: Measured cantilever deflection of the wobble strategy samples. The values are set in relation to the reference sample's mean deflection.

The fact, that in the case of the investigated alloy the deflection seems to be driven by the depth which is influenced by a certain amount of heat, directly links to the investigation of the point-wise heating strategy which is discussed in the following.

6.4 Point-wise Heating

6.4.1 Experimental Planning

The previous sections showed that offset and wobble strategies are able to influence density, spattering and surface roughness but fail to beneficially influence the distortion of parts over a wide range of parameters. The previous results lead to the assumption that the build-up of residual stresses within the alloy are hard to control because of the high thermal gradients and high cooling speeds. Yet, it seems like stresses can be reduced within SLM parts of stainless steel 316L when large depths are reheated over a certain temperature to induce some short time annealing effects.

This is where the point-wise heating strategy comes into play. Due to the fact that the heating beam is remaining in place for a short amount of time and is not continuously moving along the tracks as the melting beam does, significantly larger melt pools are expected to form which result in a large volume that is remolten or at least reheated to high temperatures. This enables an in-situ heat treatment of the part. Fig. 6.33 shows a proof of concept of this strategy with certain points at which the heating beam stops until the melting beam moved on. The point distance within this proof of concept is chosen to be 1 mm resulting in a heating beam holding time of about 1 ms.

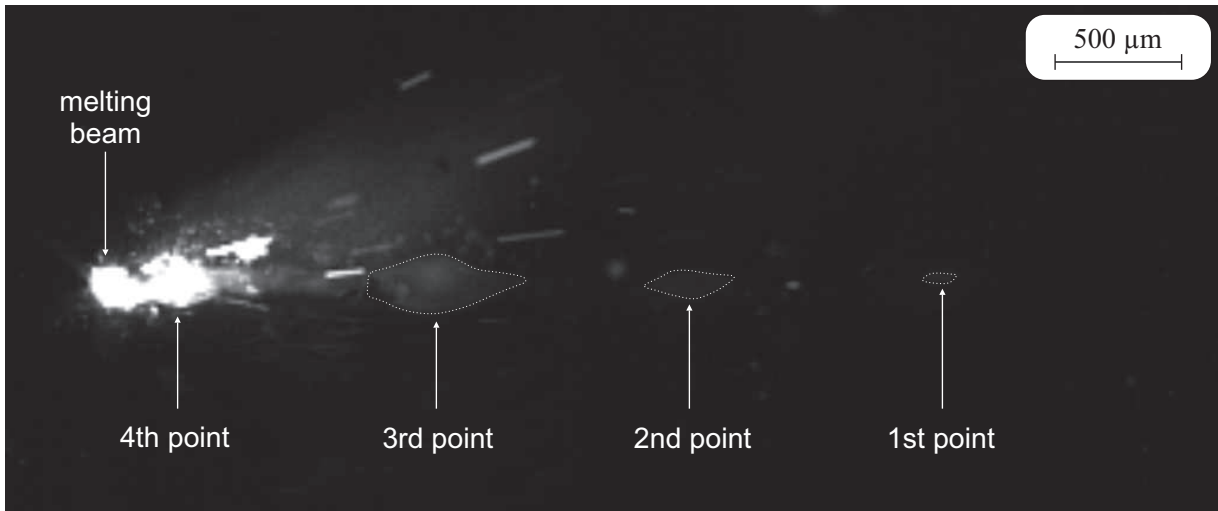


Figure 6.33: High speed image of a point-wise heating strategy parameter set using a point distance of 1 mm and a scan speed of 1000 mm/s . The points at which the heating beam stopped are still visible although heating and melting beam moved on some millimeters. The visibility of residual melt of earlier points is increased by the dashed white lines within the image.

To investigate this strategy three point distances (0.5 mm , 1.0 mm and 1.5 mm) are chosen for the three scan speeds of 1000 mm/s , 1500 mm/s and 1750 mm/s . The highest scan speed of 2000 mm/s is left out because the influence of this strategy on the density is expected to be rather low. The melting beam is still focused to $90\text{ }\mu\text{m}$ at working at 200 W in all cases. The heating beam is used in the $380\text{ }\mu\text{m}$ and 200 W setup.

The spatter characteristics are not investigated in detail for this scanning strategy because the automated evaluation tool struggles with the large distance of both beams to another. Therefore, characteristics are qualitatively discussed based on high speed images that have been taken for some of the parameter sets. The high speed images are also used to investigate further details of this strategy.

6.4.2 Microstructure and Density

The effects of the point-wise heating strategy on the microstructure are different to what can be seen in case of the other two two-beam strategies. A first impression of the 1000 mm/s samples is shown in Fig. 6.34.

The cross sections show the expected accumulation of large melt pools that are distributed all over the sample and are a result of the stopping heating beam. The 0.5 mm point distance sample shows keyhole shaped melt pools even with keyhole porosity in the bottom part of it. These keyhole melt pools are alternating with large spherical melt pools. This indicates another controls error because the wide heating beam is not expected to be able

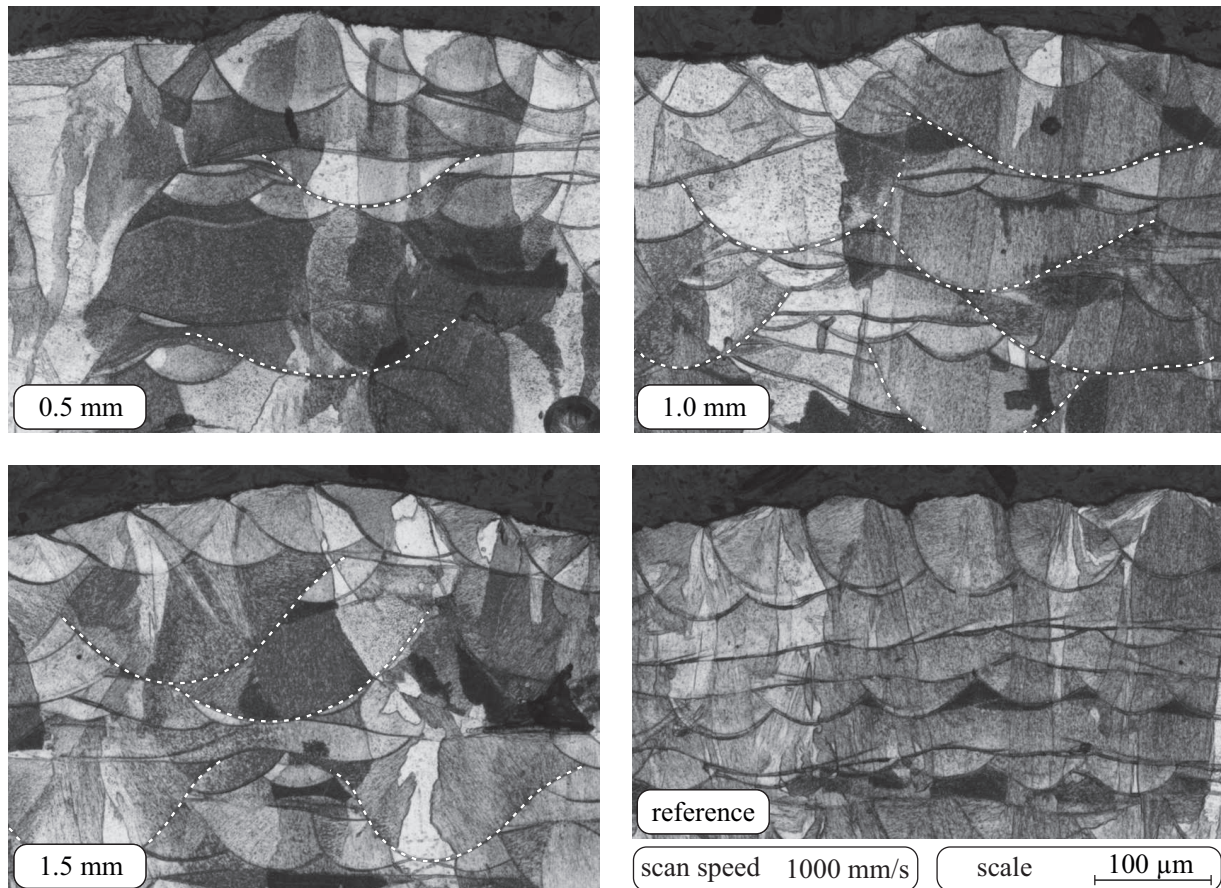


Figure 6.34: Etched cross sections of point-wise heating strategy samples manufactured with different point distances at a scan speed of 1000 mm/s . The visibility of heating point melt pool boundaries is enhanced by white dashed lines. When using a point distance of 0.5 mm roughly 0.1 J are induced to the heating point. The energy is about twice as large for 1.0 mm and about three times as large for a point distance of 1.5 mm .

to form keyhole shaped melt pools but large spherical ones. The keyhole shape leads to the assumption that the melting beam stops as well for a short period of time. This seems to happen on random occasions but quite often. The cross sections of higher point distance samples do not show these keyhole-like melt pool shapes although the holding time is higher. Hence, it is probable that a controls error occurs for point distances of 0.5 mm .

When the keyhole shaped melt pools are neglected it can be seen that the melt pool size of the large spherical melt pools increases in average with increasing point distance. Since the points are not continuously distributed along a scan track it is impossible to exclude changes in melt pool size due to an off-plane position of the melt pool but the general appearance follows the rule of increasing melt pool sizes with increasing point distances.

To get a better idea of the overall influence of this strategy, Fig. 6.35 shows the same parameter sets at a lower magnification so that a wider lateral expansion can be covered.

The first observation to make is that the grain size significantly changes when this strategy is used. The grains are in average much larger than the ones of the reference sample, in build direction as well as in lateral direction. This is the result of the larger melt pools which allow a better selection of grains, that are oriented best to grow fast along the thermal gradients, because the solidifying volume is larger and hence the time until the melt pool is completely solidified is higher.

Thereby, the grains which commonly have a lateral size of about a melt pool width are enlarged to sizes of a half holding point's melt pool width which is easily three to four times as large. Due to the higher lateral expansion of the grain it is less likely that it is overgrown by a neighboring grain within a few layers. Hence, the dimension in z-direction increases as well, yet not as strong as the lateral dimension does.

The cross sections also show that there are locations where large melt pools are more likely which is a result of the implementation of the strategy. The implementation does not consider a perfectly homogeneous distribution of the holding points over the top surface or multiple layers. At these agglomerations small bumps are visible in the top surface.

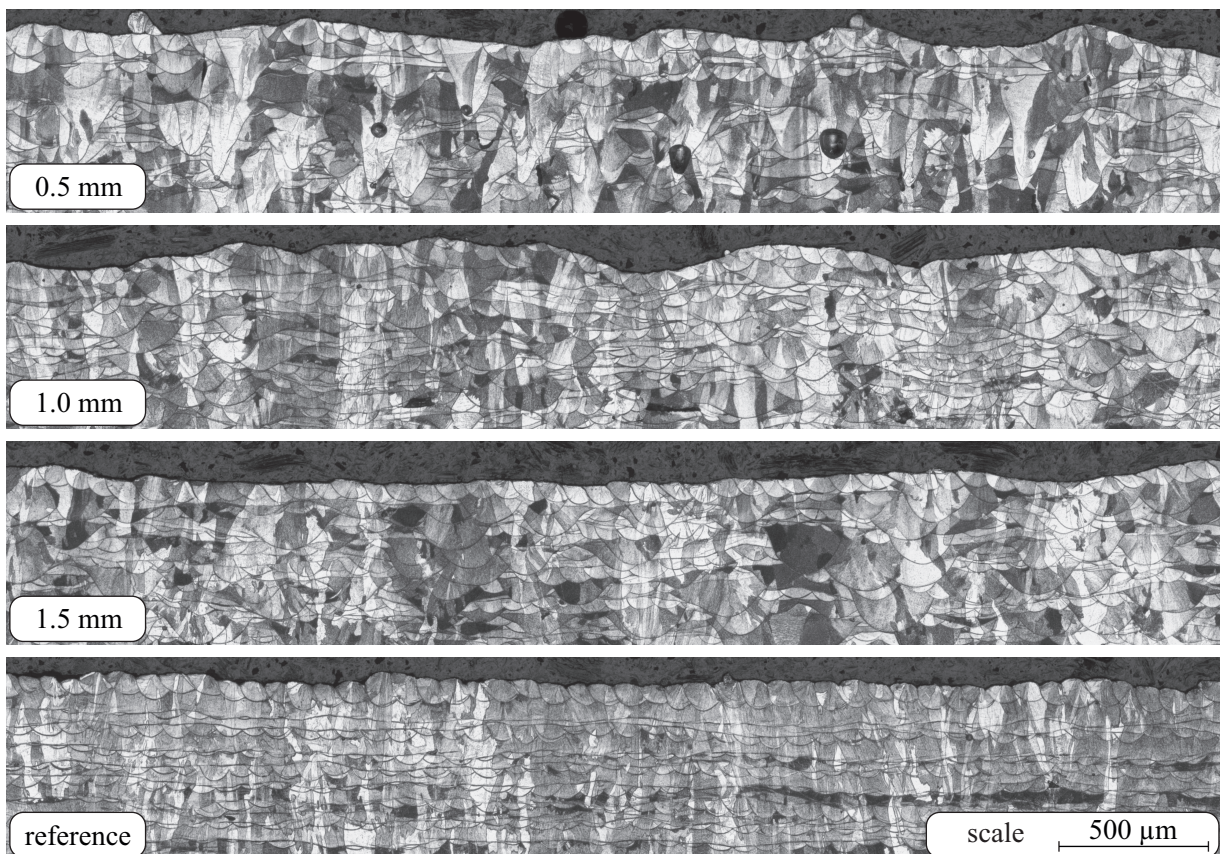


Figure 6.35: Etched cross sections of point-wise heating strategy samples manufactured with different point distances at a scan speed of 1000 mm/s . The magnification is lowered to $100\times$ to get a better idea of the global influence of the point-wise heating strategy.

Fig. 6.36 shows the same point distances of 0.5 mm , 1.0 mm and 1.5 mm at a scan speed of 1500 mm/s . It's noticeable that the amount of keyhole shaped melt pools when using a point distance 0.5 mm is significantly lower at this speed, yet several are still visible within the cross section. The other point distance samples are still mostly unaffected by this error.

The single-beam melt pools and holding points' melt pools are smaller than expected. Due to the lower energy density that is induced by the melting beam the surface is less smooth. At 0.5 mm and 1.0 mm point distance the heating beam still supports the melting beam by forming sufficiently large melt tracks. Yet, at a point distance of 1.5 mm the distance of both beams grows too large so that the influence of the heating beam on the forming of melt tracks is reduced. This effect gets more severe when the scan speed is increased even further as depicted in Fig. 6.37. At this point problems arise already when a point distance of 1.0 mm is used.

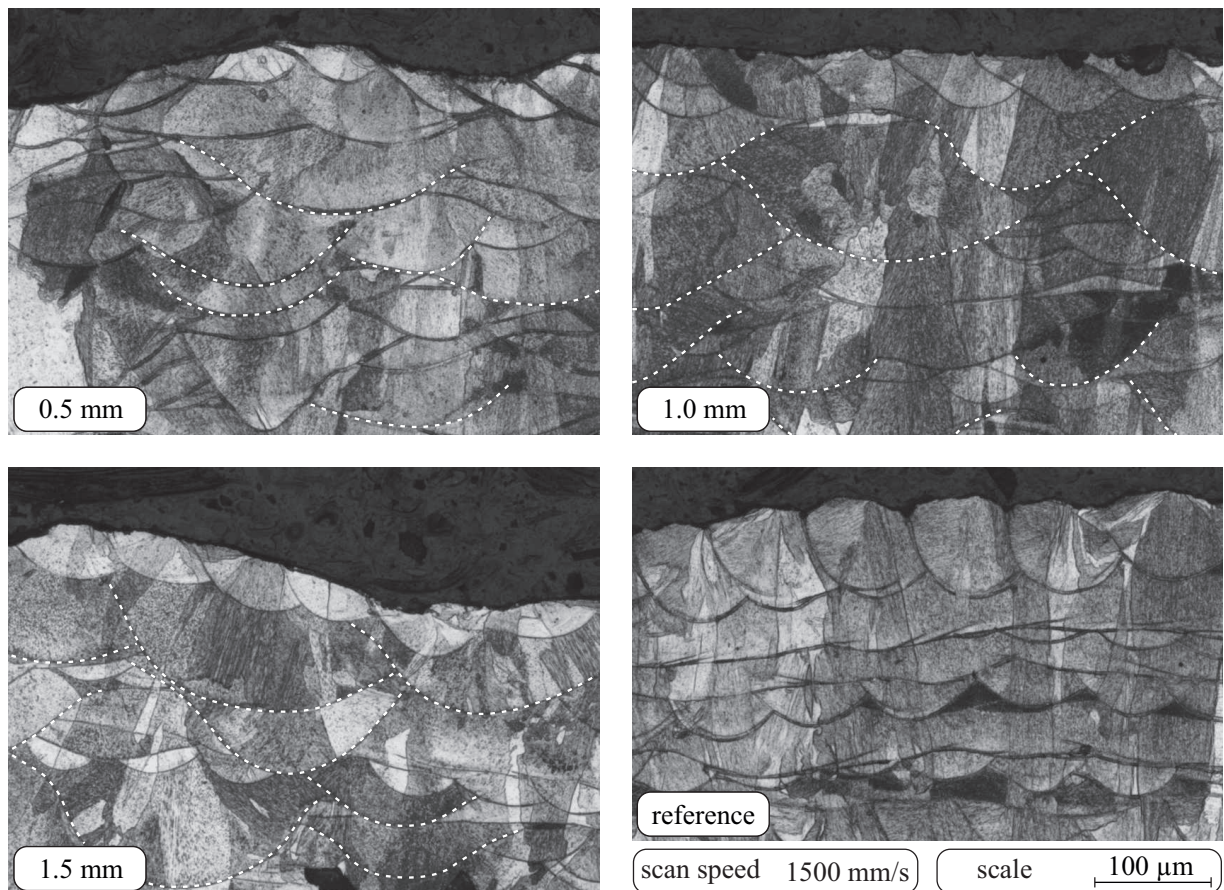


Figure 6.36: Etched cross sections of point-wise heating strategy samples manufactured with different point distances at 1500 mm/s . The visibility of heating point melt pool boundaries is enhanced by white dashed lines. When using a point distance of 0.5 mm roughly 0.067 J are induced to the heating point. The energy is about twice as large for 1.0 mm and about three times as large for a point distance of 1.5 mm .

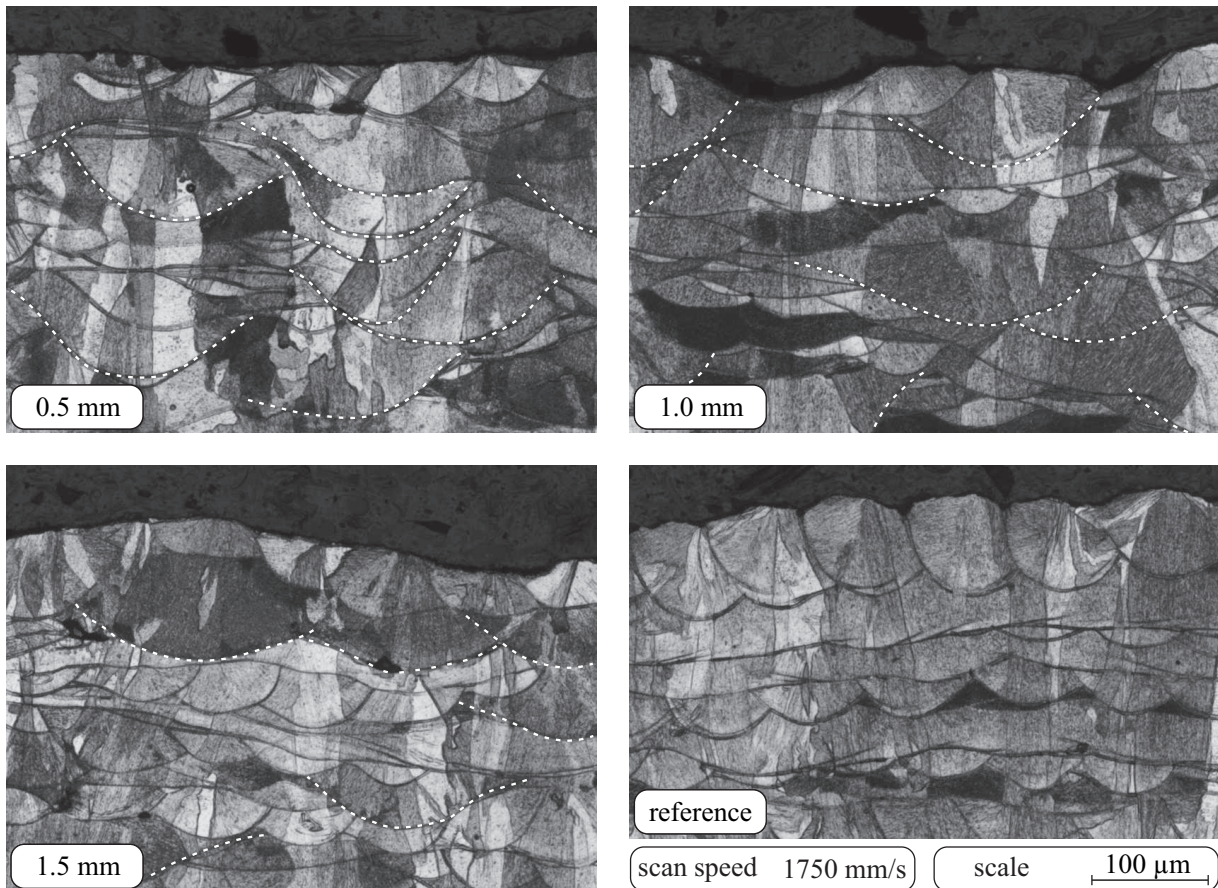


Figure 6.37: Etched cross sections of point-wise heating strategy samples manufactured with different point distances at 1750 mm/s . The visibility of heating point melt pool boundaries is enhanced by white dashed lines. When using a point distance of 0.5 mm roughly 0.057 J are induced to the heating point. The energy is about twice as large for 1.0 mm and about three times as large for a point distance of 1.5 mm .

At the lowest point distance a more or less smooth surface can be achieved at this scan speed. Yet, the discussed control error reduces the effective scan speed and thereby increases the effective energy density so that it is not safe to assume that only the small point distance is the reason for the better surface. The grains are still larger than the reference sample's ones but smaller than the ones that are generated at a lower scan speed with this strategy. This is obvious because with increasing scan speeds the holding times reduce which directly results in smaller holding point melt pools.

The density values of the previously discussed parameter sets are shown in Fig. 6.38. These support what can already be seen in the cross sections.

At 1000 mm/s the values of all three point distances are about equal. Yet, the density value of the 0.5 mm point distance is flawed by keyhole porosity which occurs due to the control error. At 1500 mm/s the density of this point distance stays about the same

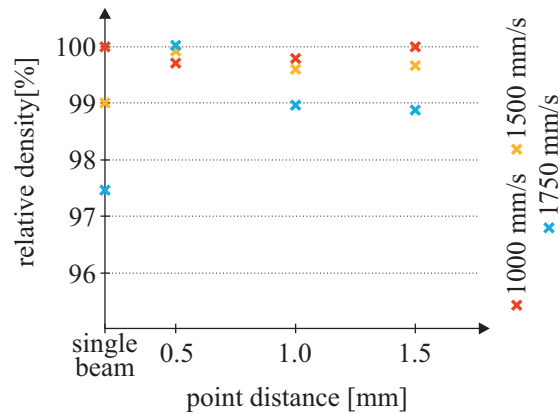


Figure 6.38: Measured density values of the point-wise heating strategy samples in relation to the reference samples mean density value. Density values of same speed single-beam samples with an overall power of 200 W are shown as well.

because the probability for the error and thus keyhole porosity to occur is smaller. The density values of the other point distances are slightly reduced. At 1750 mm/s the density values of a 1.0 mm and 1.5 mm point distance drop because in between the holding points the melting beam's power is insufficient to form robust melt pool sizes. The density of the 0.5 mm density value still stays about the same because the control error is increasing the effective energy density as well as the point distance is fairly small so that most of the heating beam's power as well supports the melting beam by forming larger melt pools.

6.4.3 High Speed Images

The high speed imaging supports the assumption that for some parameter sets an error within the controls occurs. The images show that in case of a point distance of 0.5 mm there is a high probability for the melting beam to stop for a short period of time when the heating beam moves to the next point. After this stop the melting beam proceeds until the heating beam moves again. In case of a scan speed of 1000 mm/s it is estimated that the error occurs in more than 90% of the cases when the heating beam moves. This leads to severe problems in the comparability of this parameter set. At a scan speed of 1500 mm/s the error occurs in about 50% of the cases at a point distance of 0.5 mm/s . In case of larger point distances the effect is significantly reduced. The images show that it is reduced to less than 5% for a point distance of 1 mm at 1000 mm/s scan speed and even further for higher scan speeds. In these cases the error occurs mainly at the very first holding point of the track. The error itself is illustrated in Fig. 6.39 for a point distance of 0.5 mm .

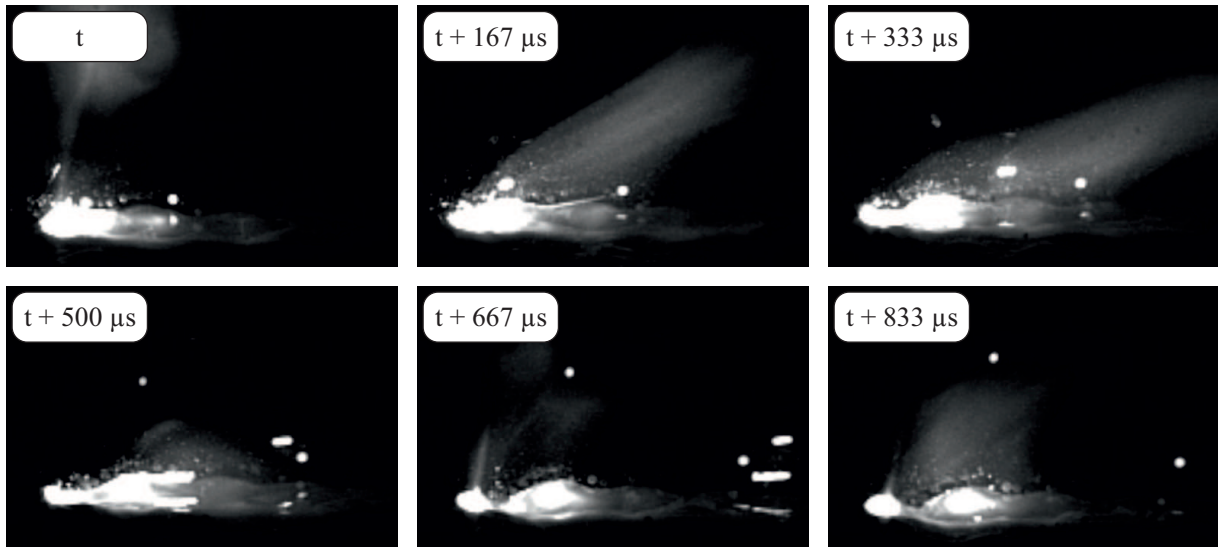


Figure 6.39: High speed images illustrating the error which is occurring at a point distance of 0.5 mm . The shown scan speed is 1000 mm/s . The process is repeated at $t + 1000\ \mu\text{s}$.

The images show that both beams stay in place for about half a millisecond. In that time the vapor jet at the melting beam's focal spot changes from a backward directed one to an upward directed vapor jet which is supporting the assumption that the stopping of the melting beam results in keyhole shaped melt pools. Yet, the heating beam stays in place as well although it should move to the next point after about half a millisecond. Therefore, it is shown that the controls are stopping any movement for about half a millisecond when the heating beam should move to its next position.

The spatter characteristics of the error-free point-wise heating parameter sets are a mixture of single-beam and large offset characteristics. Immediately after the heating beam's jump to the next holding point a small distance of both beams is present which results in spattering as it is the case for postheating offsets. Yet, the melting beam moves on increasing the distance of both beams to one another. With increasing distances the spatter characteristics change continuously as they do with increasing offsets. At distances as large as $700\ \mu\text{m}$ or more the spatter characteristics are similar to single-beam characteristics and only a very low number of new spatter particles are generated. The differences are shown in Fig. 6.40.

This means that the amount of spattering is fluctuating from high values at small beam distances to low spatter counts at high beam distances resulting in an averaged spatter count for the overall strategy. Therefore, the strategy is neither beneficial nor significantly bad for the amount of spattering within the process.

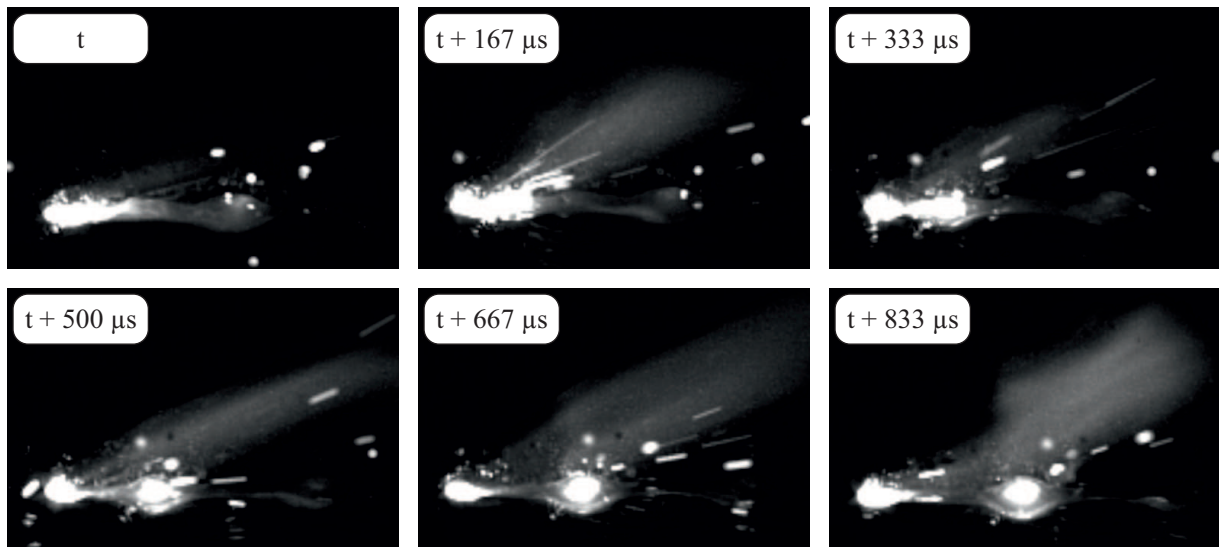


Figure 6.40: High speed images illustrating the change in spattering characteristics due to the increase of the distance between both beams. A point distance of 1 mm is used at a scan speed of 1000 mm/s . The process is repeated at $t + 1000\ \mu\text{s}$.

6.4.4 Surface Roughness

The surfaces of the samples that are manufactured with the point-wise heating strategy show a distinct bumpy structure. The measured values of the filtered surface roughness in relation to the reference sample are shown in Fig. 6.41.

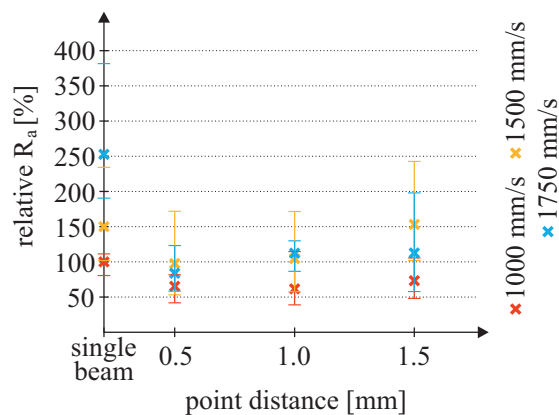


Figure 6.41: Measured mean, minimum and maximum filtered surface roughness of the point-wise heating strategy samples. Values of same speed single-beam samples are shown as well.

The surface roughness values are promising but the reduction of the mean value is not as good as it can be when the previously presented strategies are used. The value achieved when using the 0.5 mm point distance parameter has to be questioned because due to the stops of both laser beams the process does not work as intended. Still, the large number

of large melt pools that are reaching over several tracks and layers seems to be beneficial in regards to the surface roughness.

Yet, when taking a look on the unfiltered surface topology a distinct bumpy structure on the top surface can be observed for all samples of this strategy. The bumps are a result of the stacking of large melt pools which are absorbing parts of the surrounding layer due to capillary forces and are thereby forming ellipsoidal melt pools that are higher than the common layer thickness. These bumps are filtered by the set cut-off length which is why these influences are not visible in the shown graphs. What remains is just the single-beam surface roughness which is induced by the melting beam. Fig. 6.42 shows such a bumpy surface as an example.

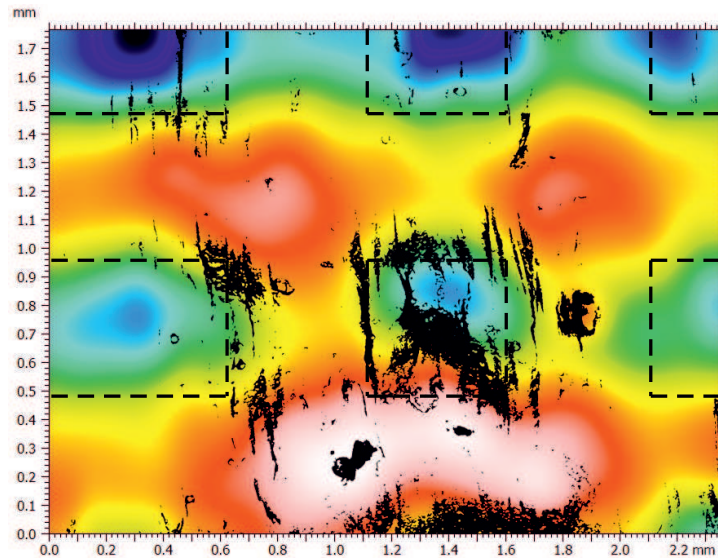


Figure 6.42: Illustration of the resulting bumpiness which is generated by the point-wise heating strategy but which is filtered and therefore not visible within the surface roughness evaluation. The shown sample is manufactured with a 1 mm point distance at a scan speed of 1000 mm/s . Only the waviness is shown. Black areas are filtered due to measuring errors. Black dashed lines indicate the mesh of heating points which over several layers generate bumps and dents on the surface.

The figure shows a grid of bumps with a mesh size of about 1 mm which is in agreement with the chosen point distance. A main reason for this extent of waviness lays within the implementation of this strategy which does not extensively account for the positioning of holding points over several layers. Only a shift along the scan direction is elaborated from track to track. Hence it is assumed that this influence can be significantly reduced when taking the build up of bumps over several layers into account and positioning the holding point in between the previous layers' ones.

6.4.5 Influence on Deflection

The influence on deflection is again investigated only for those parameters that are resulting in dense samples. Hence, only the 1000 mm/s and 1500 mm/s parameter sets are tested. The results are shown in Fig. 6.43.

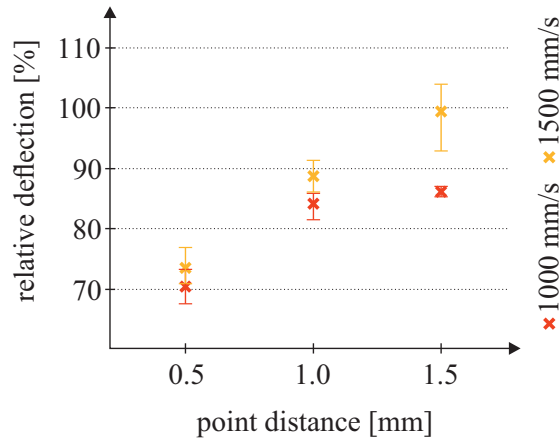


Figure 6.43: Measured mean, minimum and maximum cantilever deflection of the point-wise heating strategy samples. The values are set in relation to the reference sample's mean deflection.

The first notable change in comparison to the previously investigated samples is that the deflection of all point-wise heating samples are lower than the ones of the reference sample although half of them are manufactured at 1500 mm/s . At this speed the other strategies struggled to beneficially influence the deflection, commonly resulting in deflections which are about 10 % to 20 % higher than the reference sample's one.

The relative deflection values of all 0.5 mm point distance samples are very low with mean values of only about 70 % at 1000 mm/s and about 75 % at 1500 mm/s . This is not surprising when thinking of the common decrease of deflection with decreasing scan speeds (or increasing energy densities). As the micrographs indicate and the high speed images clearly show, the occurring error is slowing down the process due to the repetitive stopping of the melting beam as soon as the heating beam moves. This increases the effective energy density and thus results in less deflection.

Deflection values at higher point offsets of the 1000 mm/s samples are comparable to the other strategies' same scan speed samples with relative deflections of about 85 %. The most interesting observation are the low deflection values at a scan speed of 1500 mm/s at which the micrographs don't indicate any severe error in the controls at point distances of 1 mm and 1.5 mm . Still, the values are significantly lower than the other strategies' same speed samples. It is assumed that the higher depth which is affected by the heating beam is the key to this effect because the other strategies fail to influence higher depths at this

scan speed. Yet, no beneficial effect is observed when increasing the point distance which effectively increases the holding time and thus the melt pool size. The higher point distance obviously results in a more inhomogeneous distribution of the large melt pools that are generated by this strategy which is also visible within the micrographs as discussed earlier. Thereby the beneficial effect is only induced to certain locally restricted areas within the part which is assumed to be the main reason for the lower beneficial influence at those point distances.

6.5 Summary

The presented two-beam strategies offer different unique ways to influence the temperature fields within the vicinity of the melt pool so that melting and solidification, microstructure, density, spattering, surface roughness and deflection can be influenced. Yet, the strategies fail to optimize all criteria at once which is why the best strategy has to be chosen on the basis of the current needs. The following list offers a short summary of the effects that have to be expected when using the presented two-beam strategies.

1. Preheating offset strategies reduce spattering significantly and can slightly improve surface roughness. Depending on the chosen offset the density can be increased as well. The microstructure and deflection are not notably affected.
2. Postheating offset strategies offer a density increase, yet spattering is increased as well. At high offsets the strategy offers a surface smoothing effect due to an influencing of the solidification behavior. This allows working with low remelting depths. Deflection is not notably changed.
3. Wobble strategy offers the same benefits as the offset strategies but the extent depends on the chosen wobbling diameter. Yet, the beneficial effects are less strong and the strategy suffers from the necessary highly dynamic scan head mirror movement that can result in errors. The strategy induces distinct structures to the surface that are neither good nor bad.
4. Point-wise heating can beneficially influence the deflection due to in-situ annealing effects and the grain size is significantly enlarged. The influence on density and surface roughness is low, but a not optimized placing of the heating points can result in a bumpy surface structure.

Due to the lack of influence on deflection when using offset or wobble strategies it can be assumed that the build-up of residual stresses in SLM can not be significantly changed by

changing the effective intensity profile because of the harsh cooling speeds and temperature gradients. Only if the heat penetration depth is increased a positive effect can be observed when using stainless steel 316L as it is shown by using the point-wise heating strategy. Yet, hot cracking which is mainly driven by the segregation of alloying elements might be reduced by using offset strategies with high postheating offsets because of the possibility to work with small melt pool depth and thereby a low melt pool volume.

Chapter 7

Usability for Crack Susceptible Steel

The previous chapter shows that the different two-beam strategies are each offering interesting effects that could be used to improve the processability of materials that are commonly hard to process with SLM. This chapter gives an outlook on that topic by investigating the usability of two-beam strategies for increasing the processability of AISI 4140 (42CrMoS4) which contains over 0.4% carbon and thus is considered hard to weld because of its crack susceptibility at high cooling speeds. Furthermore, this material allows to evaluate the influence of the different temperature gradients and cooling speeds that are generated by the different strategies again because this material's response to a possible change is expected to be more severe.

Therefore, the investigation starts with a brief screening process based on the experiments done for stainless steel 316L to find parameter sets before discussing the strategies' influences on the microstructure and cracking behavior of this alloy. First, single-beam samples are investigated to find a proper single-beam reference parameter set which is the basis for the planning of the two-beam strategies' parameter sets. All three presented two-beam strategies are considered, although the usability of offset and wobble strategies is expected to be low due to the fact that those strategies failed to significantly reduce deflection over a wide range of parameters. Yet, previously not observed microstructural effects might occur due to the change from an austenitic to a martensitic steel. The two-beam strategies are compared to the single-beam reference as well as a single-beam strategy which elaborates a two time remelting of the top surface, imitating an in-process heat treatment as it is assumed to be present when the point-wise heating strategy is used. Vickers hardness measurements are conducted for selected samples to widen the knowledge of the effects that are induced to the microstructure by the different strategies.

7.1 Basic Investigations

The investigation starts with the search for a single-beam reference parameter set. Due to this alloy's higher thermal conductivity at room temperature in comparison to the previously investigated stainless steel, it is assumed that the optimal parameter set is to be found at a lower scan speed. Therefore, scan speeds of 700 mm/s to 1100 mm/s are used for this test. Hatch distance, beam diameter and power are kept as they were in case of the stainless steel samples. The scan strategy is changed in so far that a checkerboard pattern with a cell size of 7 mm is used to increase the transferability of the results to the larger samples that are used to investigate the cracking behavior. Yet, the hatching is kept unidirectional with a rotation of the scan pattern by 90° per layer. The results of the density measurement of these five samples are listed in Tab. 7.1.

Table 7.1: List of measured relative densities of the single-beam reference samples of AISI 4140. The full bulk density is 7.85 g/cm^3 .

scan speed [mm/s]	700	800	900	1000	1100
relative density [%]	98.5	99.4	99.1	98.8	98.3

The values show a maximum relative density of about 99.4% in case of a scan speed of 800 mm/s . Hence, this scan speed and its density value are taken as the reference sample for further investigations. This is used to set the two-beam parameter sets as well as the remelting single-beam strategy parameters. The chosen parameter sets for a screening of these strategies are listed in Tab. 7.2 together with the measured density values relative to the reference sample's one.

The density values show no surprise. The densities are decreasing with increasing scan speed except for the point-wise heating strategy which is the case because of the already extensively discussed control error. The 800 mm/s parameter sets all qualify as sufficiently dense for further investigation. Hence, a wide range of possible parameter sets is available for the build-up of notched samples for the quantification of cracking susceptibility. Yet first, a look into the microstructure of the alloy is presented.

Fig. 7.1 exemplarily shows selected micrographs of point-wise heating and offset strategies. Both samples show a distinct light upper layer which is located on top of a darker bulk material. It can be assumed that the top layer consists of martensite while the layers below are made up of tempered martensite which is supported by hardness measurements as discussed later on in section 7.2. Melt pool cross sections are hard to see because of the missing segregation of the low amount of alloying elements. Only the layerwise melt pool boundary is present because of the change in coloring within the heat affected zone.

Table 7.2: List of parameter sets that are used for further investigation as well as the measured densities of these parameter sets in relation to the reference sample. The parameters sets are defined by scan speed, strategy and its characteristic parameter. The characteristic parameters are the offset, the wobbling diameter and repetition distance, the point distance as well as the remelting speed.

strategy	scan speed [<i>mm/s</i>]	characteristic parameter	relative density [%]
offset	800	$-540 \mu m$	99.5
offset	800	$-270 \mu m$	99.4
offset	800	$-90 \mu m$	99.4
offset	800	$90 \mu m$	99.3
offset	800	$270 \mu m$	99.4
offset	800	$540 \mu m$	99.2
offset	1200	$90 \mu m$	98.5
offset	1400	$90 \mu m$	97.6
wobbling	800	$500 \mu m$ at 1/2	99.7
wobbling	1200	$500 \mu m$ at 1/2	98.8
wobbling	1400	$500 \mu m$ at 1/2	98.2
point-wise	800	$0.5 mm$	99.6
point-wise	800	$1.0 mm$	99.8
point-wise	1200	$0.5 mm$	99.5
remelting	800	$400 mm/s$	99.6
remelting	800	$800 mm/s$	99.6
remelting	800	$1200 mm/s$	99.5

Additionally, the cross sections show grains that are elongated along the build direction as it is known for several alloys. Yet, the columnar grain structure is overlaid with fine martensitic structures. Hence, the large scale background grain structures are supposedly the remains of the austenitic solidification microstructure which is present before the phase transformation to martensite. When taking a look at the point-wise heating sample it can be seen that in this sample the overall background grain size is significantly larger as it is also the case for the previously discussed stainless steel.

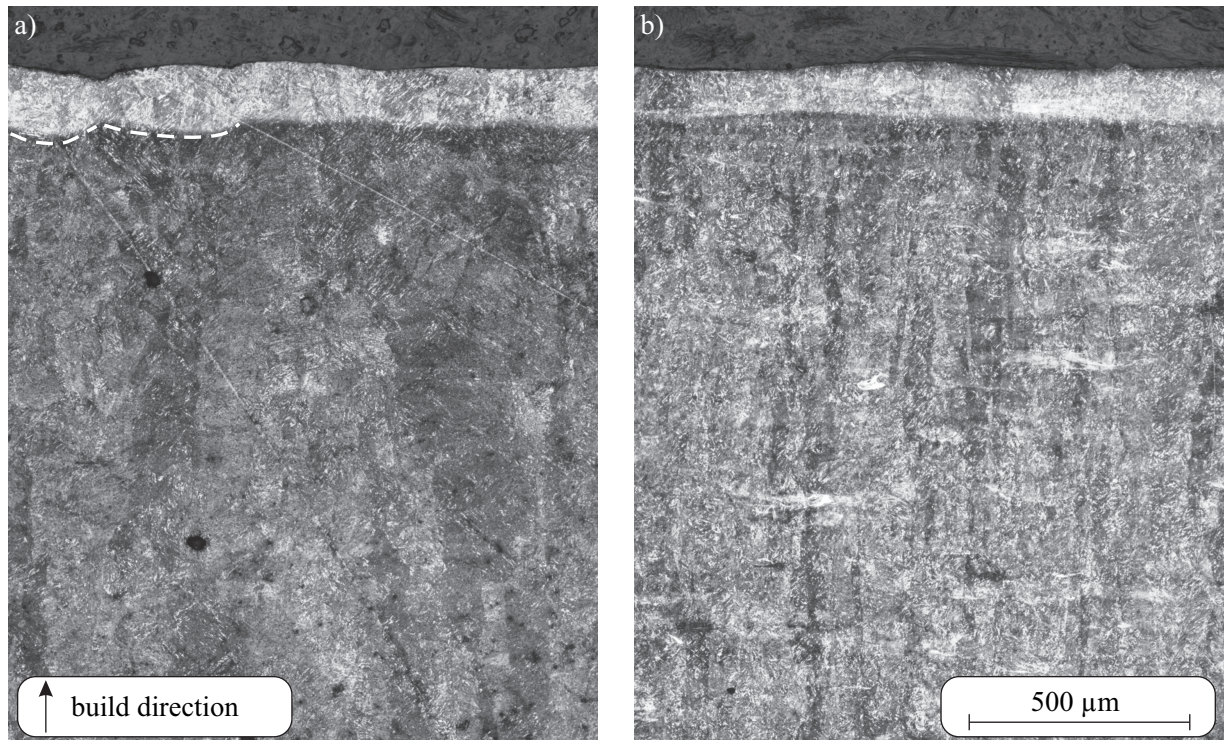


Figure 7.1: Etched cross sections of AISI 4140 manufactured using selected parameter sets. a) point-wise heating with a point distance of 0.5 mm , b) offset strategy with a postheating offset of $540\ \mu\text{m}$. Both strategies are done using a scan speed of 800 mm/s . The heating points in a) are only visible to a very small extent in the upper left (indicated by white dashed lines) because the cross section does not seem to cross the resulting melt pools in the very center. In lower layers the melt pool boundaries are resolved due to diffusion.

7.2 Influence on Cracking

No cracking is present within the cubic samples because of the small size, which is why the sample geometry is changed to a notched beam so that a location for crack initiation is defined. The beam is illustrated in Fig. 5.9. The crack penetration depth can then be used to quantify the strategies' influence on the cracking behavior. The tested parameter sets as well as the measured mean values of crack penetration depth are listed in Tab. 7.3. The number of tested parameters is reduced in comparison to Tab. 7.2 so that a large range of parameters is tested that guarantee sufficiently high density values.

The values show that only the point-wise heating strategy significantly reduces the crack penetration depth in a reproducible way. The remelting single-beam strategy results in slightly lower cracking for the 800 mm/s remelting. The 400 mm/s remelting parameter set has to be questioned because severe overheating in the vicinity of the notch was present which deformed the general shape of the sample resulting in a significantly less thick bulk area above the crack. The offset and wobble strategies result in cracks that break the

Table 7.3: List of parameter sets that are used for cracking samples as well as the measured mean crack penetration depth of these parameter sets. The parameters sets are defined by scan speed, strategy and its characteristic parameter. The characteristic parameters are the offset, the wobbling diameter and repetition distance, the point distance as well as the remelting speed. A crack penetration depth of ∞ indicates that the cracking broke the sample apart.

strategy	scan speed [mm/s]	characteristic parameter	crack penetration depth [mm]
reference	800		1.454
offset	800	$-540 \mu m$	∞
offset	800	$90 \mu m$	∞
offset	800	$540 \mu m$	∞
wobbling	800	$500 \mu m$ at $1/2$	∞
point-wise	800	$0.5 mm$	0.091
point-wise	800	$1.0 mm$	0.136
point-wise	1200	$0.5 mm$	0.130
remelting	800	$400 mm/s$	0.089
remelting	800	$800 mm/s$	0.669

sample apart. Yet, this happened during handling of the samples for cutting them of the build plate and cutting in half for embedding, grinding and polishing. This means that the strategies apparently increased the crack penetration depth in comparison to the reference sample but the exact extent of it cannot be measured because of crack growth during sample handling. Some cross sections of the crack vicinity are shown in Fig. 7.2 to get a better picture of the cracking behavior.

The figure illustrates the problem of the $400 mm/s$ remelting parameter set quite well. The bulk material thickness over the notch is only about half the size of the desired thickness so that the overall state of residual stresses is not comparable to the other samples. Yet, the cross sections do not allow the deduction of any more effects that might have resulted in a stress relief during build-up. Therefore, a Vickers hardness measurement is done in the crack vicinity to get information about the grade of annealing effects because the hardness values are reduced with increasing degree of martensite tempering. The hardness evolutions along the depth of the samples are plotted in Fig. 7.3.

The graphs show that indeed there is untempered martensite in the top surface which has already been assumed because of the lighter color of this layer. Underneath the top layer the martensite is tempered, resulting in lower hardness values depending on the degree of tempering.

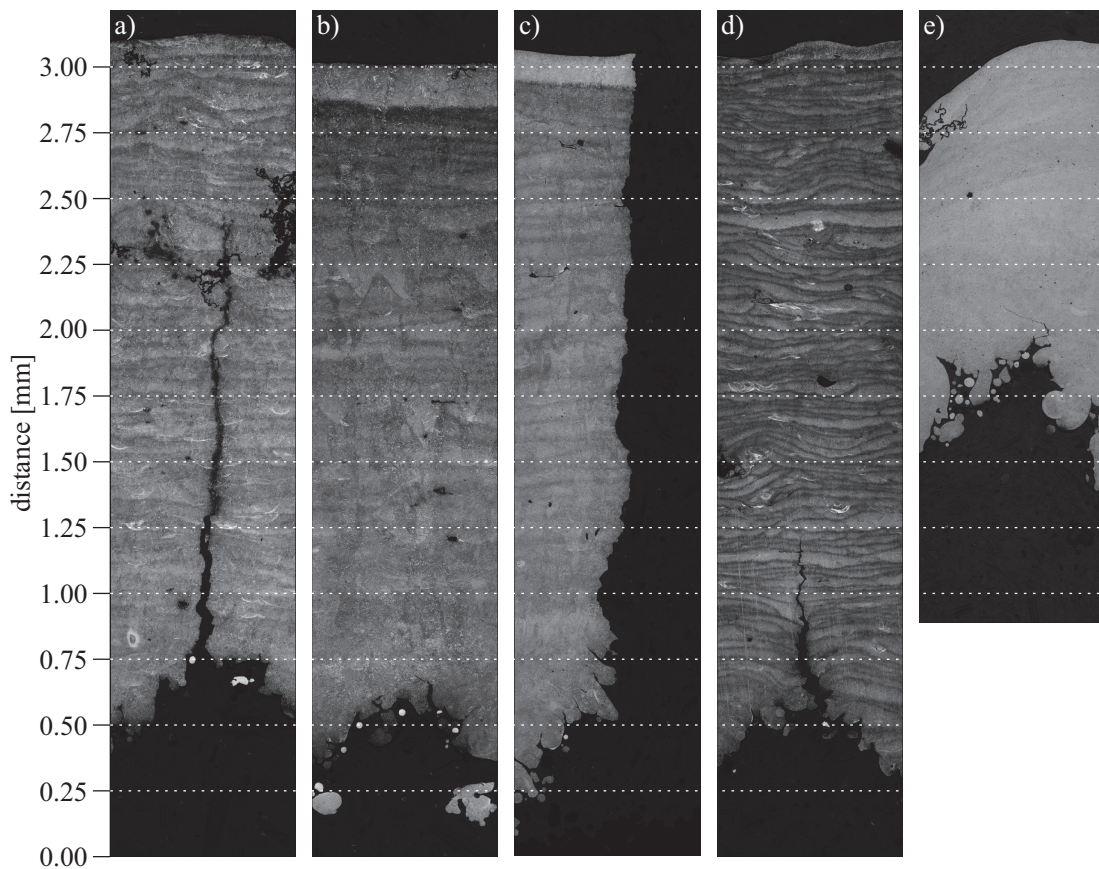


Figure 7.2: Etched cross sections of the vicinity of the notch of AISI 4140 cracking samples. a) reference single-beam sample, b) point-wise heating at 800 mm/s and a point distance of 0.5 mm , c) $-540\text{ }\mu\text{m}$ offset, d) remelting with 800 mm/s , e) remelting with 400 mm/s .

When only considering the samples for which a crack penetration depth could be measured, the reason for the difference in these values seems obvious. The reference single-beam sample has the highest hardness values so that it can be expected that the lowest extent of stress relieving martensite tempering occurs with this parameter set. By using a two time remelting with the same parameters the crack penetration depth can be reduced by about 55 % while the median hardness value is less than 10 % lower. The second remelting parameter set as well as the point-wise heating sets show crack penetration depths near zero and thus more than 90 % lower values than the reference sample. The hardness values of the point-wise heating samples are about 20 % lower while the second remelting parameter set shows a median hardness value of about 10 % less than the reference sample's one. Yet, the variation within the remelting hardness curve is high, reaching down to values comparable to the most effective point-wise heating strategy. Still, because of the deformation of the sample due to the remelting step the extent of crack penetration depth reduction has to be questioned for this remelting parameter set.

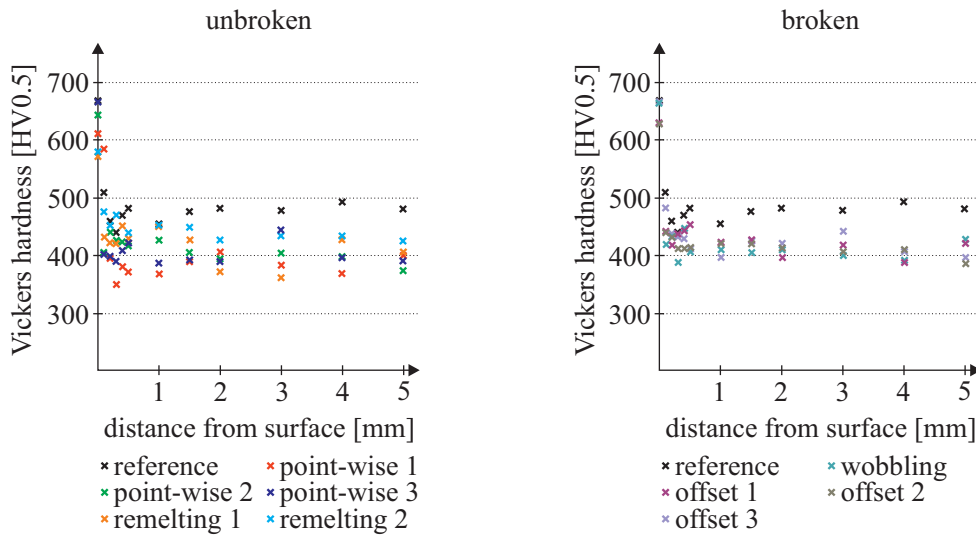


Figure 7.3: Vickers hardness evolution along the depth of the samples. A depth of 0 indicates the sample's surface. The values are separated for those sample's which broke apart and those which did not.

Using the hardness as an indicator for the crack susceptibility is known from conventional welding techniques as shown by the structural welding code [91]. For low alloyed steels with an elevated crack susceptibility due to a higher carbon content the standard proposes hardness control as a possible method to make sure that the welds are not cracking. In this method it is stated that by long year experimental studies a hardness of 350 to 400 HV is suggested as an indicator for crack-free welds, with 350 HV being stated as a value at which it can safely be assumed that no cracking occurs. This perfectly fits to the hardness values and cracking results of this thesis, although a laser welding technique is used. The samples with low cracking show wide areas with hardness values below 400 HV . And the sample with the lowest crack penetration depth shows values down to 352 HV .

In contrast to this quite clear trends which can be shown for the unbroken samples, the broken ones which were manufactured by using the other two-beam strategies show hardness values which are comparable to the one of the 1 mm point distance point-wise heating sample, which is around 400 HV . This suggests that there has to be another, unknown effect which is changing the distribution of residual stresses within the sample. The change in melt pool sizes when using the point-wise heating strategy might be a possible answer because of the changing cooling speeds and temperature gradients but no final answer can be given at this point.

Nevertheless, point-wise heating strategies show themselves to be very useful when trying to get rid of global effects, for example reducing residual stresses based defects like cracking or distortion, while offset and wobble strategies proof themselves to be beneficial to increase the process quality on melt pool scale as shown in the previous chapter. Yet, having crack free samples is only the first step to a qualification of the material for SLM.

Chapter 8

Conclusion and Outlook

Additive manufacturing and SLM in particular are promising in regards to the potential these processes offer to increase part complexity and individualization while being independent of part specific tools. Yet, the SLM process is dominated by incredibly high thermal gradients and cooling speeds that are a result of the localized melting by a highly focused laser beam which induces strong melt pool dynamics and severe evaporation. Getting these effects under control, or at least reducing these effects' influences on the final part quality as well as the process robustness without significantly reducing the process' productivity any further, is the main challenge on the way to a wider industrial applicability.

This thesis presented a general change to the process by using two synchronized beams to influence the process in the vicinity of the melt pool by changing the effective intensity profile on the one hand and on the other hand by changing the movement of the laser beam in general. To do so, a laboratory machine was built from scratch which offers two independently, yet synchronizable laser sources and scan heads with a sufficiently wide scan field overlap. This setup as well as the open control platform allow implementing different synchronized two-beam strategies which have been investigated based on a stainless steel alloy. Thereby, not only a proof of concept has been given but also an investigation of the strategies' effects on the key indicators of microstructure, density, spattering, surface roughness and deflection. These experimental results have been backed by a temperature and fluid flow field numerical modeling to widen the understanding of the change in process dynamics when using those strategies. This thesis focused on three different two-beam strategies, the offset strategy using either preheating or postheating, the wobble strategy as well as a point-wise heating strategy in which the beams are configured so that a focused melting beam as well as a heating beam with a wider beam diameter can be used.

Preheating showed itself to be beneficial to reduce spattering. Since the main part of spatter particles that can be observed within the SLM process is made up of powder particles

that are being sucked into the vapor jet induced gas stream, melting and agglomerating particles in the front of the melt pool decrease the amount of spatter particles. This is due to the fact that either the mass of the agglomerated or fused particles is increased which decreases the risk to be sucked into the gas stream or that when even a melt pool is formed in front of the melting beam no particles are left to be sucked in. Yet, no automatized quantification of the spatter size is possible with the presented tool for the evaluation of high speed images. Extending this tool might enable more detailed views into the influence on spatter characteristics and might open a window for the process optimization in regards of the minimization of large spatter particles which are a major risk for the parts' densities. When using a wide, high power heating beam parts of previous tracks are remolten so that surface roughness can be reduced slightly as well. In contrast, the influence on microstructure and density of the parts is comparably low because the final shape of the melt pool is formed later on when the melting beam passes by. This also is the reason why the influence of preheating on deflection can be neglected.

A postheating offset strategy shows the opposing effects in regards to the spattering characteristics. Most particles that are ejected backwards are passing the heating beam and thus are rapidly heated or even disintegrated into several smaller particles within the heating beam. Thereby the absolute spatter count increases significantly. Yet, it is unclear whether this effect is harmful to the process because smaller particles are less likely to be the cause for lack of fusion errors. In regards to the microstructure and density the postheating strategy offers some promising effects because the following heating beam influences the solidification and thus the general melt pool shape. This results in melt pools with double melt pool boundaries at high postheating offsets. These double melt pool boundaries are a result of the heating beam's stopping or even reversing of the solidification as can be proven with the numerical model. These postheating offsets as well increase the extent of Marangoni convection in the back of the melt pool which leads to a surface smoothing effects which can effectively be used to suppress any balling phenomena so that SLM with very little remelting is made possible. Still, postheating offsets do not influence the deflection of parts significantly.

Wobble strategies combine preheating and postheating offset strategies because the heating beam is moving around the melting beam in a circular way. Thereby both states, a heating beam in front and behind the melting beam, are present during the process. Additionally, the heating beam is covering a wider area perpendicular to the movement direction of the melting beam. Hence, the effect of spatter reduction can be achieved by agglomerating particles on the powder bed side. Due to the remelting on previous tracks distinct fish scale surface structures are generated which are neither beneficial nor harmful in regards to the surface roughness. Exactly as the offset strategy, wobbling fails to significantly

reduce the deflection of parts. The main issue of this strategy is based on the necessary highly dynamic movement of the scan head mirrors which fail to follow the desired path in case of some process parameter sets. This induces a degree of uncertainty when testing the strategies because only high speed imaging can give a clear picture of the heating beams movement. Certainty of the movement can only be achieved when checking the parameter sets with high speed imaging and the microscopy of irradiated surfaces which seems to be an irresponsibly high effort for a strategy that does not offer promising effects superior to those of the easier to handle offset strategies.

These strategies showed that influencing the temperature field only on the surface of the part is not sufficient to counteract the incredibly high cooling speeds and thermal gradients which are present within the process. Hence, the point-wise heating strategy was tested which is defined by a continuous movement of the melting beam which is overlaid by a point-wise movement of the heating beam. Thereby, the melting beam generates the common single-beam microstructure while the heating beam is locally generating far larger melt pools so that several times more previous layer are remolten. By doing so it is possible to induce higher temperature to lower layers and thereby inducing a short-time in-situ heat treatment as well as a grain coarsening. The experiments show that this actually results in a way to reduce residual stresses and thereby the deflection of the samples. Other criteria are obviously influenced less if the heating point distance is larger than the melt pool length because then both processes are happening more or less independently of one another.

The investigation of these strategies showed that all of them offer ways to improve the process, yet wobbling does not seem to be superior to the offset strategies but is increasing the effort and uncertainty of the process. Especially offset strategies enable the reduction of some inherent effects, meaning spattering and the resulting surface roughness, which are commonly addressed when talking about the applicability of the process within industry. Yet, in cases of offset strategies the use of two-beams does not seem to be the smartest solution when there is a chance of static, by lenses, or dynamic, by for example spatial light modulators, beam shaping. Including one of these options to change the intensity profile along the scan direction within a machine seems promising based on the presented results to increase the process quality and robustness without any significant drop in productivity. When using this to reduce the necessary melt pool depth even a widening of the range of processable alloys should be possible because hot cracking susceptible materials are expected to crack less with decreasing melt pool sizes. Yet, this has to be investigated in more detail. Using spatial light modulators to shape the effective beam profile might even allow to tune the extent of the observed effects because of the higher flexibility in shaping the intensity profile which is offered by those devices.

The possibility to widen the range of processable materials in regards to cold cracking susceptible alloys by using two-beam strategies has already been presented within this work. The results that were achieved when using the point-wise heating strategy show that the short-time in-situ heat treatment is sufficient to widely suppress cracking within the hard to weld steel AISI 4140. This is the first step on the way to qualify this material for the SLM process as crack free parts are necessary to continue with heat treatment and post-processing. Yet, it has to be checked whether the suppression of cracking can be achieved in more complex and larger parts as well. If this is the case, investigations into static and dynamic mechanical properties are necessary with different heat treatment and post-processing strategies to fully qualify this material for the use in SLM.

Vickers hardness measurements supported the theory that the point-wise heating strategy is effectively changing the microstructure in lower layers. Yet, heat treatment does not seem to be the sole effect that decreased the cracking probability and extent, although it is known to be a good indicator for the crack susceptibility in the resulting weld. It is assumed that the large melt pools which are a result of the point-wise heating strategy are also changing the distribution of residual stresses beneficially, but the effects behind that have to be investigated in further work to confirm that. When thinking about the in-situ heat treatment, most common machines offer the chance to heat the build plate to 200°C or higher which is expected to result in a similar effect. There as well are known strategies of induction assisted laser welding [40] in which the vicinity of the melt pool is selectively preheated to guarantee that during cool down the bainite phase is forming so that a lower hardness and stress loaded microstructure evolves. In the current setup it has to be doubted that the available power is high enough to enable that slow cooling speeds. Yet, with higher heating power, no matter if laser or electrical, comparable results can be assumed to be possible as it can be seen for the cases of high base plate heating temperatures.

In general the strength of the two-beam strategies is the flexibility of this approach. This can only be utilized when feature specific processing in SLM is used which until now is only the case for overhanging structures and top surfaces on current commercially available machines. A wide range feature and material specific processing would justify the use of two-beam strategies as well as it is justified on the present laboratory machine to allow the investigation of various different scan strategies. In other cases cheaper, easier to handle approaches like the build plate heating or static beam shaping seem to be sufficient to offer similar benefits as the presented two-beam strategies do. Dynamic beam shaping by spatial light modulators is expected to be as complex and expensive as two-beam strategies.

As a concluding remark it has to be underlined that changing the effective intensity profile at constant power and thus changing the heat distribution on the surface of a part proved itself to be insufficient to influence distortion and related effects within the SLM process because the temperature gradients and cooling speeds are far too strong to be counteracted by this approach. Yet, changing the effective intensity profile offers the chance to reduce the extent of other effects that are confined to the vicinity of the melt pool like spattering and balling.

Bibliography

- [1] F. Abe, K. Osakada, M. Shiomi, K. Uematsu, M. Matsumoto (2001) The manufacturing of hard tools from metallic powders by selective laser melting. *J. Mater. Process. Technol.*, 111(1-3):210–213.
- [2] P. Alvarez, J. Ecenarro, I. Setien, M. S. Sebastian, A. Echeverria, L. Eciolaza (2016) Computationally efficient distortion prediction in Powder Bed Fusion Additive Manufacturing. *Int. J. Eng. Res. Sci.*, 2(10):39–46.
- [3] K. Amato (2012) Comparison of Microstructures and Properties for a Ni-Base Superalloy (Alloy 625) Fabricated by Electron Beam Melting. *J. Mater. Sci. Res.*, 1(2):3–41.
- [4] K. An, L. Yuan, L. Dial, I. Spinelli, A. D. Stoica, Y. Gao (2017) Neutron residual stress measurement and numerical modeling in a curved thin-walled structure by laser powder bed fusion additive manufacturing. *Mater. Des.*, 135:122–132.
- [5] M. T. Andanani, R. Dehghani, M. R. Karamooz-Ravari, R. Mirzaeifar, J. Ni (2017) Spatter formation in selective laser melting process using multi-laser technology. *Mater. Des.*, 131:460–469.
- [6] S. Bai, J. Liu, P. Yang, M. Zhai, H. Huang (2016) Femtosecond Fiber Laser Additive Manufacturing of Tungsten. *Proc. SPI Photonics West*.
- [7] A. Bauereiß, T. Scharowsky, C. Körner (2014) Defect generation and propagation mechanism during additive manufacturing by selective beam melting. *J. Mater. Process. Technol.*, 214(11):2497–2504.
- [8] P. Bidare, I. Bitharas, R. M. Ward, M. M. Attallah, A. J. Moore (2017) Fluid and particle dynamics in laser powder bed fusion. *Acta Mater.*, 142:107–120.
- [9] C. D. Boley, S. A. Khairallah, A. M. Rubenchik (2015) Calculation of laser absorption by metal powders in additive manufacturing. *Appl. Opt.*, 54(9):2477–2482.

- [10] G. Branner (2013) Modellierung transienter Effekte in der Struktursimulation von Schichtbauverfahren. *J. Chem. Inf. Model.*, 53:1689–1699.
- [11] D. W. Brown, J. D. Bernardin, J. S. Carpenter, B. Clausen, D. Spornjak, J. M. Thompson (2016) Neutron diffraction measurements of residual stress in additively manufactured stainless steel. *Mater. Sci. Eng. A*, 678(August):291–298.
- [12] D. Buchbinder, H. Schleifenbaum, S. Heidrich, W. Meiners, J. Bültmann (2011) High power Selective Laser Melting (HP SLM) of aluminum parts. *Phys. Procedia*, 12(PART 1):271–278.
- [13] C. Casavola, S. L. Campanelli, C. Pappalettere (2008) Experimental Analysis of Residual Stresses in The Selective Laser Melting Process. *Proc. XIth Int. Congr. Expo.*
- [14] B. Cheng, S. Shrestha, K. Chou (2015) Stress and deformation evaluations of scanning strategy effect in selective laser melting. *Addit. Manuf.*, 12:240–251.
- [15] S. Clijsters, T. Craeghs, J. P. Kruth (2012) A priori process parameter adjustment for SLM process optimization. *Innov. Dev. Virtual Phys. Prototyp. - Proc. 5th Int. Conf. Adv. Res. Rapid Prototyp.*, pages 553–560.
- [16] M. Cloots (2017) *Empirische und simulative Studie über die Verarbeitbarkeit von IN738LC mittels SLM*. Phd thesis, ETH Zurich.
- [17] M. Cloots, K. Kunze, P. J. Uggowitzer, K. Wegener (2016) Microstructural characteristics of the nickel-based alloy IN738LC and the cobalt-based alloy Mar-M509 produced by selective laser melting. *Mater. Sci. Eng. A*, 658:68–76.
- [18] M. Cloots, P. J. Uggowitzer, K. Wegener (2016) Investigations on the microstructure and crack formation of IN738LC samples processed by selective laser melting using Gaussian and doughnut profiles. *Mater. Des.*, 89:770–784.
- [19] Do. Dai, D. Gu (2014) Thermal behavior and densification mechanism during selective laser melting of copper matrix composites: Simulation and experiments. *Mater. Des.*, 55:482–491.
- [20] D. Dai, D. Gu (2015) Tailoring surface quality through mass and momentum transfer modeling using a volume of fluid method in selective laser melting of TiC/AlSi10Mg powder. *Int. J. Mach. Tools Manuf.*, 88:95–107.

- [21] D. Dai, D. Gu (2016) Influence of thermodynamics within molten pool on migration and distribution state of reinforcement during selective laser melting of AlN/AlSi10Mg composites. *Int. J. Mach. Tools Manuf.*, 100:14–24.
- [22] A. G. Demir, B. Previtali (2017) Investigation of remelting and preheating in SLM of 18Ni300 maraging steel as corrective and preventive measures for porosity reduction. *Int. J. Adv. Manuf. Technol.*, 93(5-8):2697–2709.
- [23] E. R. Denlinger, M. Gouge, J. Irwin, P. Michaleris (2017) Thermomechanical model development and in situ experimental validation of the Laser Powder-Bed Fusion process. *Addit. Manuf.*, 16:73–80.
- [24] R. Ebert, F. Ullmann, D. Hildebrandt, J. Schille, L. Hartwig, Sa. Kloetzer, An. Streek, H. Exner (2012) Laser processing of tungsten powder with femtosecond laser radiation. *J. Laser Micro Nanoeng.*, 7(1):38–43.
- [25] P. Edwards, M. Ramulu (2014) Fatigue performance evaluation of selective laser melted Ti-6Al-4V. *Mater. Sci. Eng. A*, 598:327–337.
- [26] R. Engeli, T. Etter, S. Hövel, K. Wegener (2016) Processability of different IN738LC powder batches by selective laser melting. *J. Mater. Process. Technol.*, 229:484–491.
- [27] F. Geiger, K. Kunze, T. Etter (2016) Tailoring the texture of IN738LC processed by selective laser melting (SLM) by specific scanning strategies. *Mater. Sci. Eng. A*, 661:240–246.
- [28] H. Gong, K. Rafi, H. Gu, G. D. Janaki Ram, T. Starr, B. Stucker (2015) Influence of defects on mechanical properties of Ti-6Al-4V components produced by selective laser melting and electron beam melting. *Mater. Des.*, 86:545–554.
- [29] D. Gu, W. Meiners, K. Wissenbach, R. Poprawe (2012) Laser additive manufacturing of metallic components: materials, processes and mechanisms. *Int. Mater. Rev.*, 57(3):133–164.
- [30] D. Gu, P. Yuan (2015) Thermal evolution behavior and fluid dynamics during laser additive manufacturing of Al-based nanocomposites: Underlying role of reinforcement weight fraction. *J. Appl. Phys.*, 118(23).
- [31] A. V. Gusarov, J. P. Kruth (2005) Modelling of radiation transfer in metallic powders at laser treatment. *Int. J. Heat Mass Transf.*, 48(16):3423–3434.
- [32] A. V. Gusarov, I. S. Malakhova-Ziablova, M. D. Pavlov (2013) Thermoelastic residual stresses and deformations at laser treatment. *Phys. Proc.*, 41:896–903.

- [33] A. V. Gusarov, I. Yadroitsev, P. Bertrand, I. Smurov (2009) Model of Radiation and Heat Transfer in Laser-Powder Interaction Zone at Selective Laser Melting. *J. Heat Transfer*, 131(7):072101.
- [34] T. Heeling, M. Cloots, K. Wegener (2017) Melt Pool Simulation for the Evaluation of Process Parameters in Selective Laser Melting. *Addit. Manuf.*, 14:116–125.
- [35] N. E. Hodge, R. M. Ferencz, J. M. Solberg (2014) Implementation of a thermo-mechanical model for the simulation of selective laser melting. *Comput. Mech.*, 54(1):33–51.
- [36] A. Hussein, L. Hao, C. Yan, R. Everson (2013) Finite element simulation of the temperature and stress fields in single layers built without-support in selective laser melting. *Mater. Des.*, 52:638–647.
- [37] IAEA (2008) *Thermophysical Properties of Materials for Nuclear Engineering: A Tutorial and Collection of Data*. International Atomic Energy Agency.
- [38] ISO17296 (2016) Additive Fertigung - Grundlagen. *ISO-Norm*.
- [39] R. I. Issa (1986) Solution of the implicitly discretised fluid flow equations by operator-splitting. *J. Comput. Phys.*, 62(1):40–65.
- [40] A. Jahn, M. Krätzsich, B. Brenner (2008) Induction assisted laser beam welding of HSLA steel sheets. *Proc. Int. Sc. Coll. on Mod. El. Process.*, pages 195–200.
- [41] M. R. Kabir, H. Richter (2017) Modeling of Processing-Induced Pore Morphology in an Additively-Manufactured Ti-6Al-4V Alloy. *Materials (Basel)*., 10(145).
- [42] L. Kaden, G. Matthäus, T. Ullsperger, H. Engelhardt, M. Rettenmayr, A. Tünnermann, S. Nolte (2017) Selective laser melting of copper using ultrashort laser pulses. *Appl. Phys. A*, 123(9):596.
- [43] G. Kasperovich, J. Haubrich, J. Gussone, G. Requena (2016) Correlation between porosity and processing parameters in TiAl6V4 produced by selective laser melting. *Mater. Des.*, 105:160–170.
- [44] N. Keller, Fa. Neugebauer, H. Xu, V. Ploshikhin (2013) Thermo-mechanical Simulation of Additive Layer Manufacturing of Titanium Aerospace structures. *Light. Conf.*, 3(5).

- [45] K. Kempen, L. Thijs, B. Vrancken, J. Van Humbeeck, J. P. Kruth (2013) Producing Crack-Free, High Density M2 Hss Parts By Selective Laser Melting: Pre-Heating the Baseplate. *Proc. 24th Int. Solid Free. Fabr. Symp.*, pages 131–139.
- [46] S. A. Khairallah, A. Anderson (2014) Mesoscopic simulation model of selective laser melting of stainless steel powder. *J. Mater. Process. Technol.*, 214(11):2627–2636.
- [47] S. A. Khairallah, A. T. Anderson, A. M. Rubenchik, W. E. King (2016) Laser powder-bed fusion additive manufacturing: Physics of complex melt flow and formation mechanisms of pores, spatter, and denudation zones. *Acta Mater.*, 108:36–45.
- [48] H. Ki, J. Mazumder, P. S. Mohanty (2002) Modeling of laser keyhole welding: Part I. mathematical modeling, numerical methodology, role of recoil pressure, multiple reflections, and free surface evolution. *Metall. Mater. Trans. A*, 33(June):1817–1830.
- [49] W. E. King, A. T. Anderson, R. M. Ferencz, N. E. Hodge, C. Kamath, S. A. Khairallah, A. M. Rubenchik (2015) Laser powder bed fusion additive manufacturing of metals; physics, computational, and materials challenges. *Appl. Phys. Rev.*, 2(4):041304.
- [50] A. Klassen, T. Scharowsky, C. Körner (2014) Evaporation model for beam based additive manufacturing using free surface lattice Boltzmann methods. *J. Phys. D. Appl. Phys.*, 47(27):275303.
- [51] C. Körner, E. Attar, P. Heintl (2011) Mesoscopic simulation of selective beam melting processes. *J. Mater. Process. Technol.*, 211(6):978–987.
- [52] T. A. Krol, G. Branner, J. Schilp (2009) Modelle zur thermomechanischen Simulation metallverarbeitender Strahlschmelzprozesse. *Proc. ANSYS Conf. 27th CADFEM Users Meet.*
- [53] J. P. Kruth, M. Badrossamay, E. Yasa, J. Deckers, L. Thijs, J. Van Humbeeck (2010) Part and material properties in selective laser melting of metals. *16th Int. Symp. Electromachining*, pages 1–12.
- [54] J. P. Kruth, J. Deckers, E. Yasa, R. Wauthle (2012) Assessing and comparing influencing factors of residual stresses in selective laser melting using a novel analysis method. *Proc. Inst. Mech. Eng. Part B J. Eng. Manuf.*, 226(6):980–991.
- [55] J. P. Kruth, L. Froyen, J. Van Vaerenbergh, P. Mercelis, M. Rombouts, B. Lauwers (2004) Selective laser melting of iron-based powder. *J. Mater. Process. Technol.*, 149(1-3):616–622.

- [56] K. Kunze, Th. Etter, J. Grässlin, V. Shklover (2014) Texture, anisotropy in microstructure and mechanical properties of IN738LC alloy processed by selective laser melting (SLM). *Mater. Sci. Eng. A*, 620:213–222.
- [57] J. Y. Lee, S. H. Ko, D. F. Farson, C. D. Yoo (2002) Mechanism of keyhole formation and stability in stationary laser welding. *J. Phys. D. Appl. Phys.*, 35(13):1570–1576.
- [58] Y. S. Lee, W. Zhang (2016) Modeling of heat transfer, fluid flow and solidification microstructure of nickel-base superalloy fabricated by laser powder bed fusion. *Addit. Manuf.*, 12:178–188.
- [59] W. Li, J. Liu, Y. Zhou, S. Wen, Q. Wei, C. Yan, Y. Shi (2016) Effect of substrate preheating on the texture, phase and nanohardness of a Ti-45Al-2Cr-5Nb alloy processed by selective laser melting. *Scr. Mater.*, 118:13–18.
- [60] Y. Liu, Y. Yang, S. Mai, D. Wang, C. Song (2015) Investigation into spatter behavior during selective laser melting of AISI 316L stainless steel powder. *Mater. Des.*, 87:797–806.
- [61] S. Ly, A. M. Rubenchik, S. A. Khairallah, G. Guss, M. J. Matthews (2017) Metal vapor micro-jet controls material redistribution in laser powder bed fusion additive manufacturing. *Sci. Rep.*, 7(1):4085.
- [62] M. Markl, C. Koerner (2016) Multiscale Modeling of Powder Bed - Based Additive Manufacturing. *Annu. Rev. Mater. Res.*, (April):1–31.
- [63] M. J. Matthews, G. Guss, S. A. Khairallah, A. M. Rubenchik, P. J. Depond, W. E. King (2016) Denudation of metal powder layers in laser powder bed fusion processes. *Acta Mater.*, 114:33–42.
- [64] M. J. Matthews, J. Trapp, G. Guss, A. M. Rubenchik (2017) Energy coupling efficiency and melt pool dynamics associated with the laser melting of metal powder layers. Part F43-C:3–4.
- [65] P. Mercelis, J. P. Kruth (2006) Residual stresses in selective laser sintering and selective laser melting. *Rapid Prototyp. J.*, 12(5):254–265.
- [66] R. Mertens, B. Vrancken, N. Holmstock, Y. Kinds, J. P. Kruth, J. Van Humbeeck (2016) Influence of powder bed preheating on microstructure and mechanical properties of H13 tool steel SLM parts. *Phys. Procedia*, 83:882–890.
- [67] K. A. Mumtaz, N. Hopkinson (2010) Selective Laser Melting of thin wall parts using pulse shaping. *J. Mater. Process. Technol.*, 210(2):279–287.

- [68] F. Neugebauer, N. Keller, V. Ploshikhin, F. Feuerhahn, H. Köhler (2014) Multi Scale FEM Simulation for Distortion Calculation in Additive Manufacturing of Hardening Stainless Steel. *Proc. Int. Work. Therm. Form. Weld. Distortion*, (April):1–11.
- [69] B. Nie, H. Huang, S. Bai, J. Liu (2014) Femtosecond laser melting and resolidifying of high-temperature powder materials. *Appl. Phys. A Mater. Sci. Process.*, 118(1):37–41.
- [70] B. Nie, L. Yang, H. Huang, S. Bai, P. Wan, J. Liu (2015) Femtosecond laser additive manufacturing of iron and tungsten parts. *Appl. Phys. A Mater. Sci. Process.*, 119(3):1075–1080.
- [71] T. Niendorf, S. Leuders, A. Riemer, H. A. Richard, T. Tröster, D. Schwarze (2013) Highly anisotropic steel processed by selective laser melting. *Metall. Mater. Trans. B Process Metall. Mater. Process. Sci.*, 44(4):794–796.
- [72] A. Okunkova, P. Peretyagin, Y. Vladimirov, M. Volosova, R. Torrecillas, S. V. Fedorov (2014) Laser-beam modulation to improve efficiency of selecting laser melting for metal powders. *Proc. SPIE Phot. Eur.*, 9135:913524.
- [73] M. A. Ordal, R. J. Bell, R. W. Alexander, L. L. Long, M. R. Querry (1985) Optical properties of fourteen metals in the infrared and far infrared: Al, Co, Cu, Au, Fe, Pb, Mo, Ni, Pd, Pt, Ag, Ti, V, and W. *Appl. Opt.*, 24(24):4493–4499.
- [74] L. Papadakis, A. Loizou, J. Risse, S. Bremen, J. Schrage (2014) A computational reduction model for appraising structural effects in selective laser melting manufacturing. *Virtual Phys. Prototyp.*, 9(1):17–25.
- [75] L. Parry, I. A. Ashcroft, R. D. Wildman (2016) Understanding the effect of laser scan strategy on residual stress in selective laser melting through thermo-mechanical simulation. *Addit. Manuf.*
- [76] M. Praprotnik, M. Sterk, R. Trobec (2004) Inhomogeneous Heat-Conduction Problems solved by a new explicit finite difference scheme. *Int. J. Pure Appl. Math.*, 13:275–291.
- [77] K. G. Prashanth, S. Scudino, H. J. Klauss, K. B. Surreddi, L. Löber, Z. Wang, A. K. Chaubey, U. Kühn, J. Eckert (2014) Microstructure and mechanical properties of Al-12Si produced by selective laser melting: Effect of heat treatment. *Mater. Sci. Eng. A*, 590:153–160.

- [78] A. Rausch, V. Küng, C. Pobel, M. Markl, C. Körner (2017) Predictive Simulation of Process Windows for Powder Bed Fusion Additive Manufacturing: Influence of the Powder Bulk Density. *Materials (Basel)*., 10(10):1117.
- [79] A. Riemer, S. Leuders, M. Thöne, H. A. Richard, T. Tröster, T. Niendorf (2014) On the fatigue crack growth behavior in 316L stainless steel manufactured by selective laser melting. *Eng. Fract. Mech.*, 120:15–25.
- [80] M. Rombouts, L. Froyen, A. V. Gusarov, E. H. Bentefour, C. Glorieux (2005) Photopyroelectric measurement of thermal conductivity of metallic powders. *J. Appl. Phys.*, 97(2).
- [81] M. Rombouts, J. P. Kruth, L. Froyen, P. Mercelis (2006) Fundamentals of selective laser melting of alloyed steel powders. *CIRP Ann. - Manuf. Technol.*, 55(1):187–192.
- [82] A. Rubenchik, S. Wu, S. Mitchell, I. Golosker, M. LeBlanc, N. Peterson (2015) Direct measurements of temperature-dependent laser absorptivity of metal powders. *Appl. Opt.*, 54(24):7230.
- [83] M. Schmidt, M. Merklein, D. Bourell, D. Dimitrov, T. Hausotte, K. Wegener, L. Overmeyer, F. Vollertsen, G. N. Levy (2017) Laser based additive manufacturing in industry and academia. *CIRP Ann. - Manuf. Technol.*, 66(2):561–583.
- [84] B. Schoinochoritis, D. Chantzis, K. Salonitis (2015) Simulation of metallic powder bed additive manufacturing processes with the finite element method: A critical review. *Proc. Inst. Mech. Eng. Part B J. Eng. Manuf.*
- [85] Y. Shi, H. Shen, Z. Yao, J. Hu (2007) Temperature gradient mechanism in laser forming of thin plates. *Opt. Laser Technol.*, 39(4):858–863.
- [86] M. Shiomi, K. Osakada, K. Nakamura, T. Yamashita, F. Abe (2004) Residual Stress within Metallic Model Made by Selective Laser Melting Process. *CIRP Ann. - Manuf. Technol.*, 53(1):195–198.
- [87] S. Sa. Sih, J. W. Barlow (2004) The Prediction of the Emissivity and Thermal Conductivity of Powder Beds. *Part. Sci. Technol.*, 22(3):291–304.
- [88] M. Simonelli, C. Tuck, N. T. Aboulkhair, I. Maskery, I. Ashcroft, R. D. Wildman, R. Hague (2015) A Study on the Laser Spatter and the Oxidation Reactions During Selective Laser Melting of 316L Stainless Steel, Al-Si10-Mg, and Ti-6Al-4V. *Metall. Mater. Trans. A Phys. Metall. Mater. Sci.*, 46(9):3842–3851.

- [89] B. P. Singh, M. Kaviany (1991) Independent theory versus direct simulation of radiation heat transfer in packed beds. *Int. J. Heat Mass Transf.*, 34(11):2869–2882.
- [90] B. P. Singh, M. Kaviany (1992) Modelling radiative heat transfer in packed beds. *Int. J. Heat Mass Transf.*, 35(6):1397–1405.
- [91] American Welding Society (2010) *Structural Welding Code - Steel*.
- [92] G. Son (2003) Efficient Implementation of a Coupled Level-Set and Volume-of-Fluid Method for Three-Dimensional Incompressible Two-Phase Flows. *Numer. Heat Transf. Part B Fundam.*, 43(6):549–565.
- [93] G. Son (2005) a Level Set Method for Incompressible Two-Fluid Flows With Immersed Solid Boundaries. *Numer. Heat Transf. Part B Fundam.*, 47(5):473–489.
- [94] G. Son, N. Hur (2002) a Coupled Level Set and Volume-of-Fluid Method for the Buoyancy-Driven Motion of Fluid Particles. *Numer. Heat Transf. Part B Fundam.*, 42(6):523–542.
- [95] A. B. Spierings, K. Dawson, T. Heeling, P. J. Uggowitzer, R. Schäublin, F. Palm, K. Wegener (2017) Microstructural features of Sc- and Zr-modified Al-Mg alloys processed by selective laser melting. *Mater. Des.*, 115:52–63.
- [96] A. Streek, P. Regenfuss, H. Exner (2013) Fundamentals of Energy Conversion and Dissipation in Powder Layers during Laser Micro Sintering. *Phys. Procedia*, 41:851–862.
- [97] M. Tang, P. C. Pistorius, J. Beuth (2017) Prediction of lack-of-fusion porosity for powder bed fusion. *Addit. Manuf.*, 14:39–48.
- [98] L. Thijs, K. Kempen, J. P. Kruth, J. Van Humbeeck (2013) Fine-structured aluminium products with controllable texture by selective laser melting of pre-alloyed AlSi10Mg powder. *Acta Mater.*, 61(5):1809–1819.
- [99] L. Thijs, F. Verhaeghe, T. Craeghs, J. Van Humbeeck, J. P. Kruth (2010) A study of the microstructural evolution during selective laser melting of Ti - 6Al - 4V. *Acta Mater.*, 58(9):3303–3312.
- [100] I. Tolosa, F. Garcíandía, F. Zubiri, F. Zapirain, A. Esnaola (2010) Study of mechanical properties of AISI 316 stainless steel processed by "selective laser melting", following different manufacturing strategies. *Int. J. Adv. Manuf. Technol.*, 51(5-8):639–647.

- [101] J. Trapp, A. M. Rubenchik, G. Guss, M. J. Matthews (2017) In situ absorptivity measurements of metallic powders during laser powder-bed fusion additive manufacturing. *Appl. Mater. Today*, 9:341–349.
- [102] H. K. Versteeg, W. Malalasekera (1995) *An introduction to computational fluid dynamics - The finite volume method*. Longman Group Limited.
- [103] B. Vrancken, L. Thijs, Jean. P. Kruth, J. Van Humbeeck (2012) Heat treatment of Ti6Al4V produced by Selective Laser Melting: Microstructure and mechanical properties. *J. Alloys Compd.*, 541:177–185.
- [104] Z. Wang, K. Guan, M. Gao, X. Li, X. Chen, X. Zeng (2012) The microstructure and mechanical properties of deposited-IN718 by selective laser melting. *J. Alloys Compd.*, 513:518–523.
- [105] K. Wegener, A. Spierings, M. Schmid (2016) Additive Manufacturing on the Way to Industrialization. In *Proc. 6th Int. Conf. Comp. Manuf. (COMA16)*, number January, pages 11–22.
- [106] C. Weingarten, D. Buchbinder, N. Pirch, W. Meiners, K. Wissenbach, R. Poprawe (2015) Formation and reduction of hydrogen porosity during selective laser melting of AlSi10Mg. *J. Mater. Process. Technol.*, 221:112–120.
- [107] Wohlers. Wohlers Report 2016 Published. Technical report, Wohlers Associates, Fort Collins, Colorado, USA, 2016.
- [108] M. Xia, D. Gu, G. Yu, D. Dai, H. Chen, Q. Shi (2017) Porosity evolution and its thermodynamic mechanism of randomly packed powder-bed during selective laser melting of Inconel 718 alloy. *Int. J. Mach. Tools Manuf.*
- [109] P. Yuan, D. Gu (2015) Molten pool behaviour and its physical mechanism during selective laser melting of TiC/AlSi10Mg nanocomposites: simulation and experiments. *J. Phys. D. Appl. Phys.*, 48(3):035303.
- [110] M. F. Zaeh, G. Branner (2010) Investigations on residual stresses and deformations in selective laser melting. *Prod. Eng.*, 4(1):35–45.
- [111] C. Zhao, K. Fezzaa, R. W. Cunningham, H. Wen, F. De Carlo, L. Chen, A. D. Rollett, T. Sun (2017) Real-time monitoring of laser powder bed fusion process using high-speed X-ray imaging and diffraction. *Sci. Rep.*, 7(1):3602.

-
- [112] Y. Zhong, L. Liu, S. Wikman, D. Cui, Z. Shen (2016) Intragranular cellular segregation network structure strengthening 316L stainless steel prepared by selective laser melting. *J. Nucl. Mater.*, 470:170–178.
- [113] X. Zhou, D. Wang, X. Liu, D. Zhang, S. Qu, J. Ma, G. London, Z. Shen, W. Liu (2015) 3D-imaging of selective laser melting defects in a Co-Cr-Mo alloy by synchrotron radiation micro-CT. *Acta Mater.*, 98:1–16.
- [114] L. Zumofen, C. Beck, A. Kirchheim, H. J. Dennig (2017) Quality Related Effects of the Preheating Temperature on Laser Melted High Carbon Content Steels. *Proc. AMPA2017*.

Curriculum Vitae

Thorsten Heeling

born on October 16th 1989 in Oberhausen, Germany

Nationality: Germany

1999 - 2008	Secondary school, Freiherr-vom-Stein Gymnasium Oberhausen, Germany
2008 - 2012	Bachelor studies in Mechanical Engineering at Ruhr-Universität Bochum, Germany (Degree: B.Sc.)
2012 - 2013	Master studies in Mechanical Engineering at Ruhr-Universität Bochum, Germany (Degree: M.Sc.)
2014 - 2018	Research assistant and PhD student at the Institute of Machine Tools and Manufacturing (IWF), ETH Zurich, Switzerland
since 2018	Research Engineer at Robert Bosch Manufacturing Solutions GmbH, Stuttgart, Germany

List of Publications

Journals

- A. B. Spierings, K. Dawson, T. Heeling, P. Uggowitzer, R. Schaeublin, F. Palm (2016) Microstructural Features of Sc- and Zr-modified Al-Mg Alloys Processed by Selective Laser Melting. *Materials & Design*, 115:52-63.
- T. Heeling, K. Wegener (2017) Melt Pool Simulation for the Evaluation of Process Parameters in Selective Laser Melting. *Additive Manufacturing*, 14:279-282.
- T. Heeling, K. Wegener (2018) The Effect of Multi-Beam Strategies on Selective Laser Melting of Stainless Steel 316L. *Additive Manufacturing*, in Review.

Conferences

- T. Heeling, K. Wegener (2016) Computational Investigation of Synchronized Multi-beam Strategies for the Selective Laser Melting Process. *Physics Procedia*, 83:899-908.
- T. Heeling, L. Zimmermann, K. Wegener (2016) Multi-Beam Strategies for the Optimization of the Selective Laser Melting Process. *Proceedings of the 2016 Annual International Solid Freeform Fabrication Symposium*, Austin, USA, pages 1428-1438.
- T. Heeling, M. Gerstgrasser, K. Wegener (2017) Investigation of Selective Laser Melting Spatter Characteristics for Single- and Multi-Beam Strategies using High Speed Imaging. *Proceedings of Lasers in Manufacturing Conference 2017*, Munich, Germany.

Press articles

- K. Wegener, A. B. Spierings, T. Heeling (2016) Zukunft additiver Fertigung. *Schweizer Maschinenmarkt*, 10.11.2016.